Study of Supercritical CO_2 Displacing Water at the Pore Scale and Its Relevance at the Core Scale and Beyond

by

Jim Kuo

A thesis
presented to the University of Waterloo
in fulfillment of the
thesis requirement for the degree of
Master of Applied Science
in
Mechanical Engineering

Waterloo, Ontario, Canada, 2012

AUTHOR'S DECLARATION

I hereby declare that I am the sole author of this thesis. This is a true copy of the thesis, including any required final revisions, as accepted by my examiners.

I understand that my thesis may be made electronically available to the public.

Abstract

The advent of carbon sequestration and rapidly decreasing cost of computing creates opportunities in reservoir characterization for carbon storage. Reservoir description has been based on conventional seismic and well-log analysis which may be uncertain in real environments. In recent years, there had been interests in understanding the underlying physics behind multiphase flows in small scales. With the advancement in imaging technology, it is possible to reconstruct real porous media for simulation purposes. All the previous studies have the information gathered at the pore scale and have been limited by the uncertainty of how to use it. Upscaling of such information has always been a topic of great challenge in the fields of geology, hydrogeology, and petroleum engineering.

Multiphase lattice Boltzmann method (LBM), a proven tool to simulate flows in porous media, was applied to simulate flows in porous media at the pore scale (above the representative element volume (REV) size threshold) to gather permeability and relative permeability data. Artificially created fields of permeability and relative permeability are used as benchmarks. Cores extracted from these fields were used in kriging to recreate the fields. Pores from the cores were extracted and used as individual data points for kriging. Comparing the core kriged and pore kriged fields showed that while only modest improvements in permeability field accuracy of 4-16% was seen, large accuracy improvements in relative permeability fields of 55-82% was observed.

Acknowledgements

This thesis would not have been possible without the encouragement and support of my advisor, Professor Fue-Sang Lien, who challenged me to be a better researcher. I would like to thank the Natural Sciences and Engineering Research Council (NSERC) and Ontario Ministry of Training, Colleges and Universities for their financial support. I would also like to thank my friends and colleagues at the University of Waterloo for their support and the wonderful conversations over the years. I want to give special acknowledgments to Profs. Cecile Devaud and John Wen for their patience while reviewing my manuscript. It is a pleasure to thank my friends and family for their undying support. I would lastly like to thank my rabbit Charlie for his company and the joy that he brought me.

Dedication

To my parents, Danny and Grace, and my brother Tim, who had always encouraged me to follow my dreams and devoted much of their energy to ensure that I would receive the support I needed to get there. Thank you.

Table of Contents

List of Figures

List of Tables

Nomenclature

Roman Letter

Lattice Boltzmann

A	Parameter of the free-energy model
Ca	Capillary number
c_i	Speed at direction i
c_s	Speed of sound
F_i	Body force
f_i	Probability distribution function to track the velocity and pressure field
f_i^-	Negative composition of the distribution function f_i
f_i^+	Positive composition of the distribution function f_i
$f_i^{eq,+}$	Positive composition of the equilibrium probability distribution function f_i^{eq}
$f_i^{eq,-}$	Negative composition of the equilibrium probability distribution function f_i^{eq}
f_i^{eq}	Equilibrium probability distribution function for f_i
g_i	Probability distribution function to track the phase field
g_i^-	Negative composition of the distribution function g_i
g_i^+	Positive composition of the distribution function g_i
$g_i^{eq,+}$	Positive composition of the equilibrium probability distribution function g_i^{eq}
$g_i^{eq,-}$	Negative composition of the equilibrium probability distribution function g_i^{eq}
g_i^{eq}	Equilibrium probability distribution function for g_i
k	Surface tension parameter
M	Viscosity ratio
Q	Number of directions
$Q_{i\alpha\beta}$	Tensor for $c_{i\alpha}c_{i\beta} - c_s^2\delta_{\alpha\beta}$
p_0	Bulk pressure
Re	Reynolds number
t	Time
u_α	Velocity in the α-direction
w_i	Weights for each of the direction i

x	Cartesian coordinates

Porous Media Generation

A	Amplitude of variation
a, b, c	Coordinates of different points in space
F	Value at the specified location
H	Reduction factor
i, j, k	Cartesian coordinates
n	Number of passes
R	Random number between -1 and 1

Upscaling

K	Permeability
K_{eff2D}	Effective permeability in 2D

Darcy's Law

k_i	Permeability
$k_p(saturation)$	Relative permeability of phase p at a certain saturation
k_{rp}	Relative permeability of phase p
P	Pressure
q_{pi}	Darcy velocity of phase p in direction i

Greek Symbols

Lattice Boltzmann Method

Γ	Mobility parameter
γ	Surface tension
$\delta_{\alpha\beta}$	Delta function
Λ	Parameter for two relaxation time
μ	Chemical potential
ρ	Density
ν	Kinematic viscosity
τ	Relaxation parameter for density fields

τ_ϕ	Relaxation parameter for phase fields
τ_{gas}	Relaxation parameter for gas
τ_{liq}	Relaxation parameter for liquid
ϕ	Phase
ω	Relaxation parameter for density fields
ω_ϕ	Relaxation parameter for phase fields
ω_+	Positive composition of the relaxation parameter for density fields
ω_-	Negative composition of the relaxation parameter for density fields
ω_+^ϕ	Positive composition of the relaxation parameter for phase fields
ω_-^ϕ	Negative composition of the relaxation parameter for phase fields

Darcy's Law

μ_p	Dynamic viscosity for phase p

Subscripts

α, β	Cartesian tensor indices
i	Direction indices
p	Phase

Acronyms

BGK	Bhatnagar-Gross-Krook
CCS	Carbon capture and storage
D3Q19	Three dimensional and contains 19 velocities
LBE	Lattice Boltzmann equation
LBM	Lattice Boltzmann method
REV	Representative elementary volume
SRT	Single relaxation time
TRT	Two relaxation time

Chapter 1
Introduction

1.1 Motivation

Owing to the increasing urbanization and energy use, various methods to control carbon dioxide (CO_2) emissions have been proposed. Carbon capture and storage (CCS) is a process that captures CO_2 emissions and stores them in geological formations deep inside the earth. CCS is becoming accepted world wide as a viable way to greatly reduce greenhouse gas emissions into the atmosphere. CO_2 from power plants and other industrial processes is compressed and transported to underground long-term storage sites.

Mapping the permeability field of a subsurface reservoir is one of the most crucial elements in predicting direction and speed of flow. Permeability can be obtained by core analysis in the laboratory or in reservoir settings. If these measurements cannot be obtained directly, indirect methods can be applied by relating geometric properties to permeability correlations. In practice, these methods are used in conjunction to provide maximum information for the current geological model for the reservoir (Babadagli and Al-Salmi 2004). Correlations between measureable parameters such as porosity are used to determine the permeability. The correlation of permeability and porosity are obtained from routine core analysis without detailed geological justification. Such a simple prediction could result in high errors as high as ten folds (Permadi and Susilo 2009). These indirect methods often prove to be unreliable thus need to be used with other methods. Direct, or core-based, permeability measurements are considered the standard to which all other measurements are compared (Permadi et al. 2009).

Indirect methods rely on measurement of other properties. Well log data are used to fill the gap in which direct method cannot. The most commonly used are empirical models, which are based on the correlations. Other methods used to determine permeability from well log data such as neural network have been applied (Balan et al. 1995).

A core plug, or sample can range between 3cm to 15cm in diameter. Core analysis today uses X-ray computerized tomography (CT) to determine the porosity distributions in two- and three-dimensions (Unalmiser et al. 1998). Measurements are also done to determine the permeability and the relative permeability of these samples. It is worthy to note that the value of the average permeability of a

formation is not as important in reservoir engineering calculations as the permeability distribution across the reservoir, obtained from routine core analysis (Dake 2001).

One novel method of measuring permeability is the use of conducting a number of local permeability measurements of a core sample to represent the core as a whole (Tidwell and Wilson 2002). A study conducted by Taylor et al. (Taylor and Vinopal 1999) showed that a mini-permeameter, an equipment which measures permeability in small dimensions, can provide multiple nondestructive measurements of a core sample and offer equivalent data to that provided by more expensive conventional core analysis.

Geostastical method of kriging has been used for characterization of permeability of reservoir domains. Works done by Venteris et al (Venteris and Carter 2009), Journel et al (Journel and Alabert 1990), Illman et al (Illman et al. 2010) and Xu et al (Xu et al. 1992) demonstrated that geostatistical kriging are important in characterization of reservoir.

CO_2 is supercritical at temperatures and pressures above the critical values of 304K and 7.38MPa. Such critical condition of CO_2 is reached at depth of about 700m. (Suekane et al. 2005) Supercritical CO_2 injected into deep saline aquifers would undergo the multiphase process that displaces the water (Suekane et al. 2006). Lattice Boltzmann method (LBM) has proven to be a useful tool in simulating flows in porous media. Previous works done by Gunstensen et al. (Gunstensen and Rothman 1993), Yiotis et al (Yiotis et al. 2007), Huang et al. (Huang et al. 2009), Martys et al. (Martys and Chen 1996), and Suekane et al. (Suekane et al. 2005) show that multiphase LBM is ideal for simulating relative permeability curves in irregular geometries.

The aim of this thesis is to introduce an idea that combines these ideas of taking distributions of local small permeability measurements, multiphase LBM, and geostatistical kriging to reservoir characterization. Numerical experiments relevant to CCS were conducted based on two-phase immiscible flow of water and supercritical CO_2 in porous media.

1.2 Study Objective

A new study on relative permeability in pore samples using binary fluid LBM model in multi-directions and a new method on how to utilize the pore scale results is proposed in this thesis. The main objective of this study is to utilize the main advantages of LBM in characterizing flows in porous media and applying to the field of carbon capture and storage. Flows in ten porous medium

are considered, then utilized to create two mappings of fields. The proposed method would be conducted on these fields and compared with current characterization practices.

1.3 Thesis Outline

Chapter 2 introduces the governing equations and formulations used in present research. Chapter 3 presents the numerical implementation and the boundary conditions used in the binary fluid LBM used in this thesis. Chapter 4 focuses on the test problems to validate the implementations commonly used in the literatures. Chapter 5 describes the results obtained from LBM at the pore scale, and how the permeability and relative permeability data is used at the core and field scales. Chapters 6 and 7 highlight the main findings and provide suggestions for future work.

Chapter 2
Mathematical Formulation

2.1 Lattice Boltzmann Model for Binary Liquid

The lattice Boltzmann equation (LBE) is based on probability distribution functions that satisfy the macroscopic variables and conservation laws. LBE consists of two parts: a local collision step and a streaming step. The information from the node is transferred to the adjacent nodes by these two parts. For this binary liquid model, two sets of populations are required to adequately describe the motions of the immiscible fluids: one (f_i) to track the pressure and velocity fields, and the other (g_i) to represent the phase field, indicating the so-called gas or liquid phase, shown in Eq. (1) and Eq. (2) (Kuzmin et al. 2011; Kuzmin et al. 2011). In these formulations, single relaxation time (SRT) collision or BGK collision scheme is shown; however, two relaxation time (TRT) collision scheme is employed to increase accuracy and stability. Collision of fluid particles is considered as relaxation toward local equilibrium (Sukop and D.T. Thorne 2006). These equilibrium functions f_i^{eq} and g_i^{eq} are described in Eq. (3), Eq. (4), Eq. (5), and Eq. (6).

$$f_i(x + c_i, t + 1) = f_i(x, t) + \omega f_i^{eq}(x, t) - \omega f_i(x, t) + F_i \tag{1}$$

$$g_i(x + c_i, t + 1) = g_i(x, t) + \omega g_i^{eq}(x, t) - \omega g_i(x, t) \tag{2}$$

$$f_i^{eq} = w_i \left(3p_0 - k\phi\Delta\phi + \frac{u_\alpha c_{i\alpha}}{c_s^2} + \frac{Q_{i\alpha\beta} u_\alpha u_\beta}{2c_s^2} \right) + k w_i^{\alpha\beta} \partial_\alpha \phi \partial_\beta \phi, \quad 1 \le i \le Q - 1 \tag{3}$$

$$f_0^{eq} = \rho - \sum_{i \neq 0} f_i^{eq} \tag{4}$$

$$g_i^{eq} = w_i (\Gamma\mu + \phi \frac{u_\alpha c_{i\alpha}}{c_s^2} + \phi \frac{Q_{i\alpha\beta} u_\alpha u_\beta}{2c_s^2}), \quad 1 \le i \le Q - 1 \tag{5}$$

$$g_0^{eq} = \rho - \sum_{i \neq 0} g_i^{eq} \tag{6}$$

$$\mu = -A\phi + A\phi^3 - k\Delta\phi \tag{7}$$

Γ is the mobility parameter, μ is the chemical potential (Eq. (7)) , k is related to surface tension, A is a parameter of the free-energy model, Q is the number of directions in the D3Q19 model, the tensor $Q_{i\alpha\beta} = c_{i\alpha}c_{i\beta} - c_s^2\delta_{\alpha\beta}$, $c_s = \frac{\sqrt{3}}{3}$ is the speed of sound, and bulk pressure is expressed as $p_0 = c_s^2\rho + A(-0.5\phi^2 + 0.75\phi^4)$. The discrete velocity sets are defined in Eq. (8), Eq. (9), and Eq. (10). The direction weights needed to recover macroscopic equations are listed in Eq. (11), Eq. (12), Eq. (13), Eq. (14), Eq. (15), Eq. (16), Eq. (17), and Eq. (18).

$$c_{ix} = \{0, 1, -1, 0, 0, 0, 0\ 1, -1, 1, -1, 0, 0, 0, 0, 1, -1, 1, -1\} \tag{8}$$

$$c_{iy} = \{0, 0, 0, 1\ , -1, 0, 0, 1, 1, -1, -1, 1, -1, 1, -1, 0, 0, 0, 0\} \tag{9}$$

$$c_{iz} = \{0, 0, 0, 0, 0, 1, -1, 0, 0, 0, 0, 1, 1, -1, -1, 1, 1 - 1, -1\} \tag{10}$$

$$w_{1-2}^{xx} = w_{3-4}^{yy} = w_{5-6}^{zz} = \frac{5}{12} \tag{11}$$

$$w_{3-6}^{xx} = w_{1-2,5-6}^{yy} = w_{1-4}^{zz} = \frac{-1}{3} \tag{12}$$

$$w_{7-10,15-18}^{xx} = w_{7-14}^{yy} = w_{11-18}^{zz} = \frac{-1}{24} \tag{13}$$

$$w_{11-15}^{xx} = w_{15-18}^{yy} = w_{7-10}^{zz} = \frac{1}{12} \tag{14}$$

$$w_{7,10}^{xy} = -w_{8,9}^{xy} = w_{11,14}^{yz} = -w_{12,13}^{yz} = w_{15,18}^{zx} = -w_{16,17}^{zx} = \frac{1}{4} \tag{15}$$

$$w_0 = 0 \tag{16}$$

$$w_{1-6} = \frac{1}{6} \tag{17}$$

$$w_{7-18} = \frac{1}{12} \tag{18}$$

The kinematic viscosity is defined as $\nu = c_s^2(\tau - 0.5)$, $M = \Gamma(\tau_\phi - 0.5)$ is the mobility parameter, $\tau = 1/\omega$ and $\tau_\phi = 1/\omega_\phi$ are the relaxation parameters. The f_i equation simulates the continuity and Navier-Stokes equation. The g_i equation simulates the movement of the phases with velocities

supplied from the Navier-Stokes equation. The gas phase is denoted by $\phi = -1$, and the liquid phase is denoted as $\phi = 1$. The relaxation time is taken to be linear and bounded by τ_{gas} and τ_{liq}, $\tau = \tau_{gas} + \left(\frac{\phi+1}{2}\right)(\tau_{liq} - \tau_{gas})$. The surface tension is given as $\gamma = \sqrt{\frac{8kA}{9}}$ and the interface width is $5\sqrt{\frac{k}{A}}$ lattice units.

2.2 Porous Media Generation

Midpoint Displacement Method is a commonly used method for landscape generation for computer graphics (Gothäll et al. 2005) and porous media, such as geological media (Lu et al. 2003) and snow (Carbone et al. 2010).

In 1-D the midpoint displacement algorithm starts with a line between two points. These two points are considered to define the horizontal axis of the 2-D final geometry. The midpoint of the two initial points is displaced vertically by a random amount. The two new line segments are then divide in half and the midpoints of these segments are displaced by a random amount. This process is repeated until the desired level of detail is attained with the range of the random displacement being reduced in each pass. For example if the random range was reduced by half for each pass and the original range of the random displacement was from -1.0 to 1.0, then the range for the second pass with 2 midpoints would be from -0.5 to 0.5, and -0.25 to 0.25 for the third pass with 4 midpoints. (Jilesen et al. 2011)

The amount by which the range of random numbers is reduced in each pass is controlled. In fact the amount by which the range decreases is one of the factors which control the final geometry. The expression for the midpoint value is shown in Eq. (19). An example of the algorithm is shown in Figure 1 (Jilesen et al. 2011),

$$\mathrm{F(x)} = \frac{1}{2}\left(\mathrm{F}\left(\mathrm{x} + \frac{\mathrm{dx}}{2}\right) + \mathrm{F}\left(\mathrm{x} - \frac{\mathrm{dx}}{2}\right)\right) + \mathrm{A} \cdot \mathrm{R} \cdot 2^{-\mathrm{H} \cdot \mathrm{n}} \tag{19}$$

where R is a random number between -1 and 1, A is a constant controlling the amplitude of the variation, H is the reduction factor and n is the pass number. Increasing the value of H, results in a smoother final geometry.

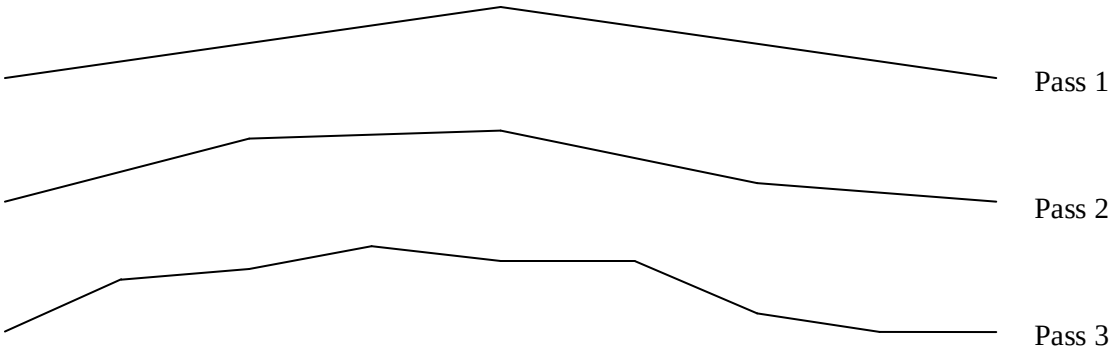

Figure 1 – Example of 1D midpoint displacement algorithm (Jilesen et al. 2011)

The equations to generate random field values in three-dimensions using neighbouring points are provided below:

$$\mathrm{F(x,y,z)} = \frac{1}{\mathrm{n}}\sum_{1}^{\mathrm{n}} \mathrm{F(neighbours)} + \mathrm{A}\cdot\mathrm{R}\cdot 2^{-\mathrm{H}\cdot\mathrm{n}} \tag{20}$$

$$\mathrm{i,j,k} = \mathrm{a} \rightarrow \mathrm{c}, \qquad \mathrm{b} = \frac{\mathrm{a}+\mathrm{c}}{2} \tag{21}$$

where a, b, and c are the coordinates of different points in space, such that b is the midpoint of a and c. For example, point (b, b, b) is the midpoint of points (a, a, a) and (c, c, c) but the values of the a's in a point, i.e. (a, a, a), are not necessarily the same. In another words, point (a, a, a) can be thought of as (a_x, a_y, a_z).

$$\mathrm{F(b,b,b)} = \frac{\big(\mathrm{F(a,a,a)} + \mathrm{F(a,a,c)} + \mathrm{F(a,c,a)} + \mathrm{F(a,c,c)}\big)}{8} + \frac{\mathrm{F(c,a,a)} + \mathrm{F(c,a,c)} + \mathrm{F(c,c,a)} + \mathrm{F(c,c,c)}}{8} + \mathrm{A}\cdot\mathrm{R}\cdot 2^{-\mathrm{H}\cdot\mathrm{n}} \tag{22}$$

$$\mathrm{F(b,a,b)} = \frac{(\mathrm{F(a,a,a)} + \mathrm{F(a,a,c)} + \mathrm{F(c,a,a)} + \mathrm{F(c,a,c)} + \mathrm{F(b,b,b)} + \mathrm{F(b,a-b,b)})}{6} + \mathrm{A}\cdot\mathrm{R}\cdot 2^{-\mathrm{H}\cdot\mathrm{n}} \tag{23}$$

$$F(a,b,b) = \frac{(F(a,a,a) + F(a,a,c) + F(a,c,a) + F(a,c,c) + F(b,b,b) + F(a-b,b,b))}{6} + A \cdot R \cdot 2^{-H \cdot n} \quad (24)$$

$$F(b,b,a) = \frac{(F(a,a,a) + F(a,c,a) + F(c,a,a) + F(c,c,a) + F(b,b,b) + F(b,b,a-b))}{6} + A \cdot R \cdot 2^{-H \cdot n} \quad (25)$$

$$F(b,a,a) = \frac{(F(a,a,a) + F(b,a,b) + F(c,a,a) + F(b,a,a-b) + F(b,b,b) + F(b,a-b,b))}{6} + A \cdot R \cdot 2^{-H \cdot n} \quad (26)$$

$$F(a,b,a) = \frac{\left(F(a,a,a) + F(a,b,b) + F(a,c,a) + F(b,b,a) + F(a,b,a-b) + F(a-b,b,a)\right)}{6} + A \cdot R \cdot 2^{-H \cdot n} \quad (27)$$

$$F(a,a,b) = \frac{(F(a,a,a) + F(a,a,c) + F(a,b,b) + F(a,a-b,b) + F(b,a,b) + F(a-b,a,b))}{6} + A \cdot R \cdot 2^{-H \cdot n} \quad (28)$$

2.3 Upscaling

Numerical simulations of flows in porous media are important in many different applications. In particular to the field of CCS, experiments are costly and difficult, if not impossible to conduct. Numerical simulations are limited by the computing resources in terms of size and details of the simulations. Mathematical techniques that replace the detailed descriptions of the geological model with a coarser model while retaining the important features have been explored. This process is referred to as upscaling (Das and Hassanizadeh 2005; Green and Paterson 2007).

One widely used technique in upscaling petroleum reservoirs is renormalization (King 1989). The technique involves describing the flow in porous media as flow of current in electric circuits. The blocks of cells then can be simplified to a single equivalent resistor, and hence an effective permeability. King (King 1989) derived a two-dimensional solution by assuming no flow boundary conditions normal to the flow, and that uniform pressures are applied at the inlet and outlet, shown in

Figure 2. The result is applicable only to isotropic medium, anisotropic media can be treated in the similar fashion. King (King 1989) further extended the model to three-dimensional but noted that there is no simple closed form solution. Further improvements were introduced by others (Dainton et al. 1997; Renard and de Marsily 1997; Zhang 1998; Christie 2001; Hastings and Muggeridge 2001; Farmer 2002).

Green and Paterson (Green et al. 2007) presented an approximation of three-dimensional renormalization technique based on the full three-dimensional method that is three orders of magnitude faster but with less than 5% reduction in accuracy. The two dimensional and three dimensional equations are shown in Eq. (29) and Eq. (30).

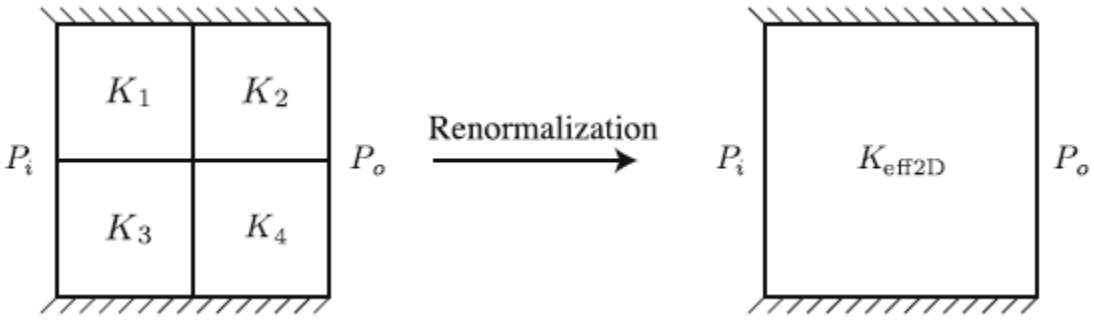

Figure 2 – Renormalization in two dimensions (Green et al. 2007)

$$K_{eff2D}(K_1, K_2, K_3, K_4) = \frac{4(K_1 + K_3)(K_2 + K_4)[K_1K_3(K_2 + K_4) + K_2K_4(K_1 + K_3)]}{\{(K_1 + K_2 + K_3 + K_4)[K_1K_3(K_2 + K_4) + K_2K_4(K_1 + K_3)] + 3(K_1 + K_2)(K_3 + K_4)(K_1 + K_3)(K_2 + K_4)\}} \quad (29)$$

$$K_{eff3D}(K_1, K_2, K_3, K_4, K_5, K_6, K_7, K_8) = \frac{1}{4}\Big(K_{eff2D}(K_1, K_2, K_3, K_4) + K_{eff2D}(K_5, K_6, K_7, K_8) + K_{eff2D}(K_5, K_6, K_1, K_2) + K_{eff2D}(K_7, K_8, K_3, K_4)\Big) \quad (30)$$

2.4 Kriging

Kriging is an estimation procedure which can be used to make contour maps. Kriging uses the information from semivariogram to find a set of weights that are used in the estimation of the surface at unsampled locations. The weights change according to the geographic arrangement of the samples. In this study, punctual kriging is employed. Punctual kriging is the simplest type of kriging, thus is used to just demonstrate the proposed methodology in this study. Under this simple kriging, the drift is considered to be zero (Davis 1986).

2.5 Darcy's Law

Fluid flow in porous normally occurs much below the threshold of turbulent flow. Under these conditions, Darcy's law can be assumed to describe the flow adequately. Darcy's law is in the form of

$$q_{pi} = -\frac{k_{rp}k_i}{\mu_p}\frac{\partial P}{\partial x_i} \tag{31}$$

where q_{pi} is the Darcy velocity (LT^{-1}), or volume flux density of phase p in the i direction, k_i is the permeability (L^2) of the material in the i direction. k_{rp} (varies from 0 to 1) is the relative permeability of the phase p, μ_p is the dynamic viscosity ($ML^{-1}T^{-1}$) of the phase (Parker 1989).

2.5.1 Permeability

Permeability is an intrinsic material property of the porous medium, which is determined by using Darcy's law when there is only one phase present. Eq. (32) shows how permeability is determined if viscosity, pressure gradient, and Darcy velocity is known.

$$k_i = -\frac{\mu q_i}{\frac{\partial P}{\partial x_i}} \tag{32}$$

2.5.2 Relative Permeability

Relative permeability is the ratio of the effective permeability of the porous medium to the absolute permeability shown in Eq. (33). The relative permeability is a function of a system of two or more fluids and the porous media (Abaci et al. 1992).

$$k_{rp} = \frac{k_p(saturation)}{k} \tag{33}$$

There are two measures of relative permeability, one is steady and the other one is unsteady. The unsteady time was used to study CO_2 displacing water. This is more relevant to the field of carbon capture and storage as seen in the world done by (Bennion 2005). It is more advantageous to use LBM for unsteady simulation as it is an unsteady method.

Chapter 3
Numerical Implementation

3.1 LBM Boundary Conditions

A number of boundary conditions have been developed for LBM such as periodic, bounce-back, constant pressure and constant velocity. One of the advantages of LBM is the flexibility to incorporate complex solid boundaries that makes it possible to simulate realistic porous media (Sukop et al. 2006).

3.1.1 Bounce-back

Bounce-back boundaries are easy to implement and yet is one of the advantages of LBM. In the case of porous media, the solid nodes are separated into two types – boundary solids that lie at the solid-fluid interface, and the isolated solids that do not contact fluid. This reduces the computing time significantly when only a small fraction of the domain is occupied by the fluids. In particular, half bounce-back is used in this study for stability. In half bounce-back, the particles stream into the solid nodes and reflect back in the opposite direction in the same time step shown in Figure 3 (Sukop and Or 2004; Sukop et al. 2006).

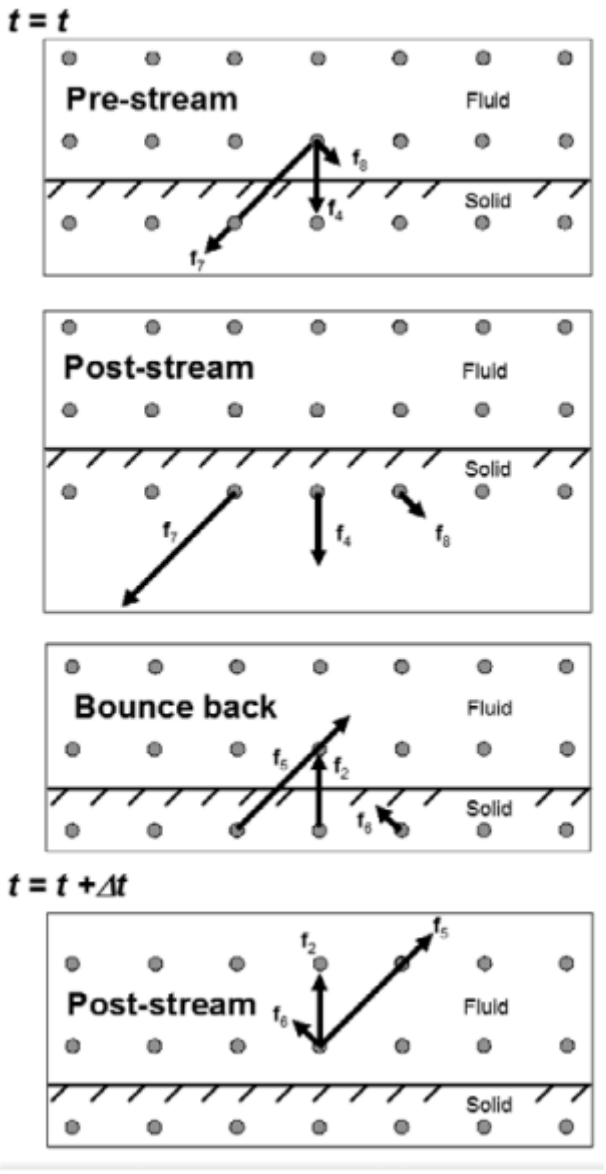

Figure 3 - Half bounce-back for LBM (Sukop et al. 2004)

3.1.2 Periodic Boundary Condition

Periodic boundary condition is perhaps the simplest boundary condition in LBM. It allows the fluids that leave the domain to enter the domain by wrapping around the domain, show in Figure 4. The porous media generator takes advantage of this periodicity in LBM and generates a fully periodic

porous medium in all directions. In the pore scale simulations, the periodic boundary conditions are used in the transverse directions (Sukop et al. 2006).

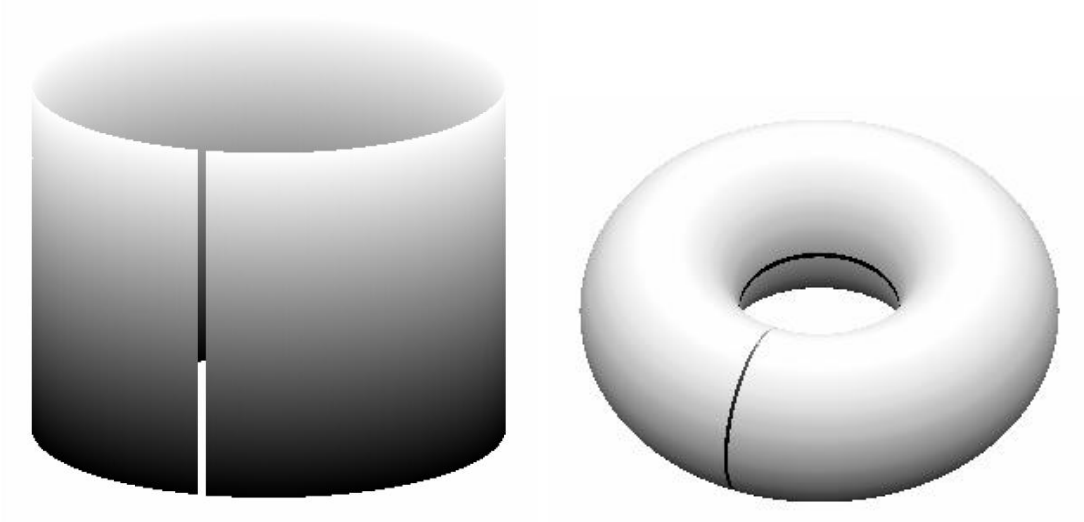

Figure 4 - Concept of periodic boundary conditions (Sukop et al. 2006)

3.2 LBM Force

External force represents an external force population. The force population represents an external body force and is represented using a source term that appears in the Navier-Stokes equation. The source term is given in Eq. (34) (Guo et al. 2002).

$$F_i = \left(1 - \frac{\omega}{2}\right) w_i \left[\frac{\boldsymbol{c_i} - \boldsymbol{u}}{c_s^2} + \frac{\boldsymbol{c_i} \cdot \boldsymbol{u}}{c_s^4} \boldsymbol{c_i}\right] \cdot \boldsymbol{F} \tag{34}$$

3.3 Contact Angle

Contact angle of two fluids at the surface is described by the Young-Laplace equation, seen in Eq. (35), where γ_{f1s} and γ_{f2s} are the fluid-solid interfacial tensions and γ_{12} is the fluid to fluid interfacial tension (Pooley et al. 2008).

$$\cos\theta = \frac{(\gamma_{f1s} - \gamma_{f2s})}{\gamma_{12}} \tag{35}$$

In this lattice Boltzmann model, the contact angle θ, or wettability, is controlled by changing the phase value ∅ of the surface.

3.4 Two Relaxation Time Scheme

The two relaxation time (TRT) scheme has certain advantages over single relaxation time (SRT or BGK) in terms of stability and accuracy. TRT allows better control of the accuracy depending on the problem with only 10 – 20% additional computational cost than that of BGK (Pan et al. 2006; Kuzmin and Derksen 2011). TRT also allows higher accuracy in modeling contact angles as the spurious velocities at the interface are reduced (Pooley et al. 2008). There are strong numerical evidences that permeability of an arbitrary porous media is independent of the chosen viscosity value when a specific so-called "magic parameter", Λ, is fixed and no-slip conditions are modeled with bounceback (Kuzmin et al. 2011).

As the name implies, TRT uses two relaxation rates, ω_+ and ω_-, noting that if the two rates are equal, the TRT scheme collapses down to the SRT scheme. The distribution functions need to be decomposed into positive and negative parts as well, shown below:

$$f_i = f_i^+ + f_i^- \tag{36}$$

$$f_i^{eq} = f_i^{eq,+} + f_i^{eq,-} \tag{37}$$

$$f_i^+ = (f_i + f_i(opposite))/2 \tag{38}$$

$$f_i^- = (f_i - f_i(opposite))/2 \tag{39}$$

$$f_i^{eq,+} = (f_i^{eq}{}_i + f_i^{eq}(opposite))/2 \tag{40}$$

$$f_i^{eq,-} = (f_i^{eq} - f_i^{eq}(opposite))/2 \tag{41}$$

$$g_i = g_i^+ + g_i^- \tag{42}$$

$$g_i^{eq} = g_i^{eq,+} + g_i^{eq,-} \tag{43}$$

$$g_i^+ = (g_i + g_i(opposite))/2 \tag{44}$$

$$g_i^- = (g_i - g_i(opposite))/2 \tag{45}$$

$$g_i^{eq,+} = (g_i^{eq}{}_i + g_i^{eq}(opposite))/2 \quad (46)$$

$$g_i^{eq,-} = (g_i^{eq} - g_i^{eq}(opposite))/2 \quad (47)$$

where the opposite function stands for the index of direction in the opposite direction. The magic parameter is given as $\Lambda = (\frac{1}{\omega_+} - \frac{1}{2})(\frac{1}{\omega_-} - \frac{1}{2})$. This includes spatial error, stability, best advection and diffusion. When the magic parameter, $\Lambda = \frac{1}{12}$, is adopted, best results for advection is produced as it removes the third order error (Kuzmin et al. 2011).

Single relaxation formulations for collision and streaming equations are shown directly below as a reminder. The TRT formulations for these equations are listed in Eq. (48) and Eq. (49).

$$f_i(x + c_i, t + 1) = f_i(x, t) + \omega f_i^{eq}(x, t) - \omega f_i(x, t) + F_i \quad (1)$$

$$g_i(x + c_i, t + 1) = g_i(x, t) + \omega g_i^{eq}(x, t) - \omega g_i(x, t) \quad (2)$$

$$f_i(x + c_i, t + 1) = f_i(x, t) + \omega_+ f_i^{eq,+}(x, t) + \omega_- f_i^{eq,-}(x, t) - \omega_+ f_i^{+}(x, t) - \omega_- f_i^{-}(x, t) + F_i \quad (48)$$

$$g_i(x + c_i, t + 1) = g_i(x, t) + \omega_+^{\phi} g_i^{eq,+}(x, t) + \omega_-^{\phi} g_i^{eq,-}(x, t) - \omega_+^{\phi} g_i^{+}(x, t) - \omega_-^{\phi} g_i^{-}(x, t) \quad (49)$$

3.5 Relating LBM Units to Real Units

LBM porous media simulations are related to real units by means of nondimensional parameters. Three nondimensional parameters are important for the immiscible two-phase flow through porous media. These parameters are the Reynolds number $Re = \frac{ud}{\nu}$, where d is the width of the smallest channel in a porous medium, viscosity ratio $M = \frac{\mu_1}{\mu_2}$, and capillary number $Ca = \frac{\mu u_{characteristic}}{\gamma}$ (Huang et al. 2011; Kuzmin et al. 2011). It is important to note that sometimes it is not possible to achieve full matching relationships with the nondimenional parameters between LBM units and real units; however, one needs to consider the leading non-dimensional numbers which are responsibility for the physical phenomena nondimensional parameters (Kuzmin et al. 2011) .

Chapter 4

Test Cases

4.1 Laplace-Young equation

A common experiment is to use spherical bubbles of non-wetting fluid to determine the capillary pressure between two immiscible fluids (Gunstensen et al. 1993). The capillary pressure is given by Laplace-Young equation in Eq. (50) (Dullien 1979). The equation shows that the capillary pressure trend should be linear with the slope of 2γ and passes through the origin. The measured points and the theoretical prediction are shown in Figure 5 and Figure 6. The numerical simulation trend shows good agreement with the linear prediction.

$$P_{in} - P_{out} = \frac{2\gamma}{R} \tag{50}$$

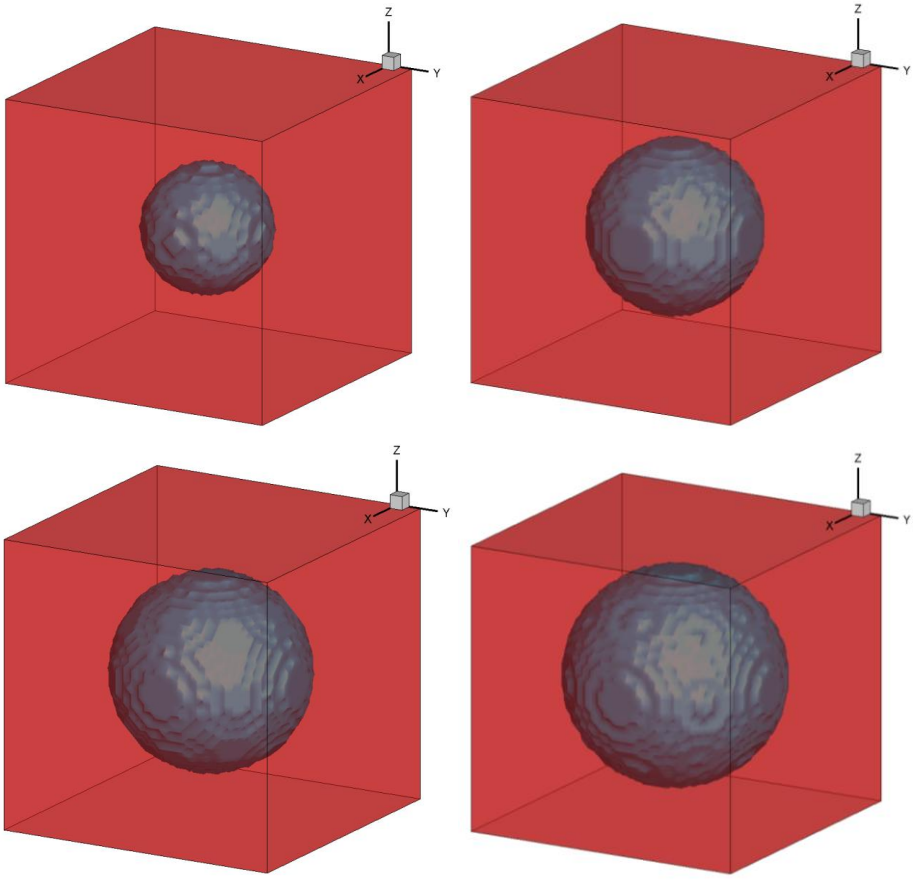

Figure 5 - Bubble of changing sizes for verification of Young-Laplace equation

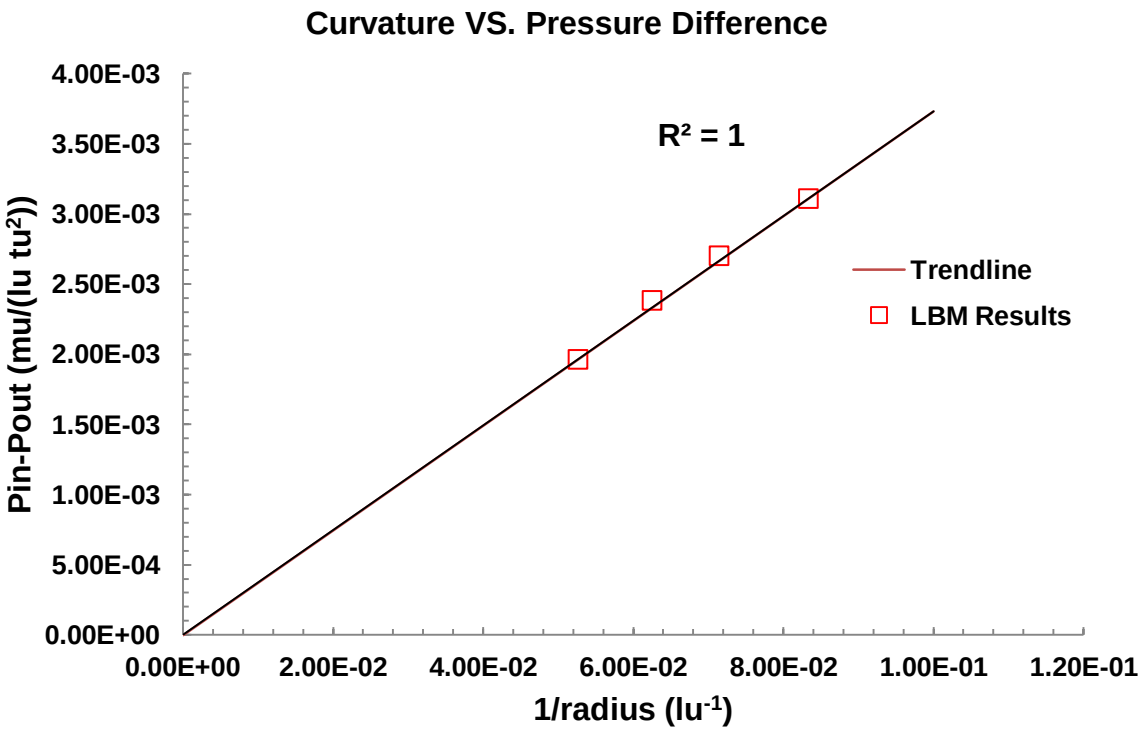

Figure 6 - Pressure as a function of bubble diameter

4.2 Wettability and Contact Angle

Solid surfaces are always involved in two-phase porous media flows. This can be established by changing the "phase" of the wall in the LBM initialization. Having wall phase value closer to the droplet increases wettability while the reverse decreases it. Figure 7 shows the different wettability situations. Initially, the gas droplet (non-wetting phase) is assumed to be neutral wetting, and allowed to evolve into different a wide range of wettability, starting from completely non-wetting (spherical), partially non-wetting (120°), neutral wetting (90°), and partially wetting (60°). Therefore, this implementation is capable of predicting a wide range of wettabilities.

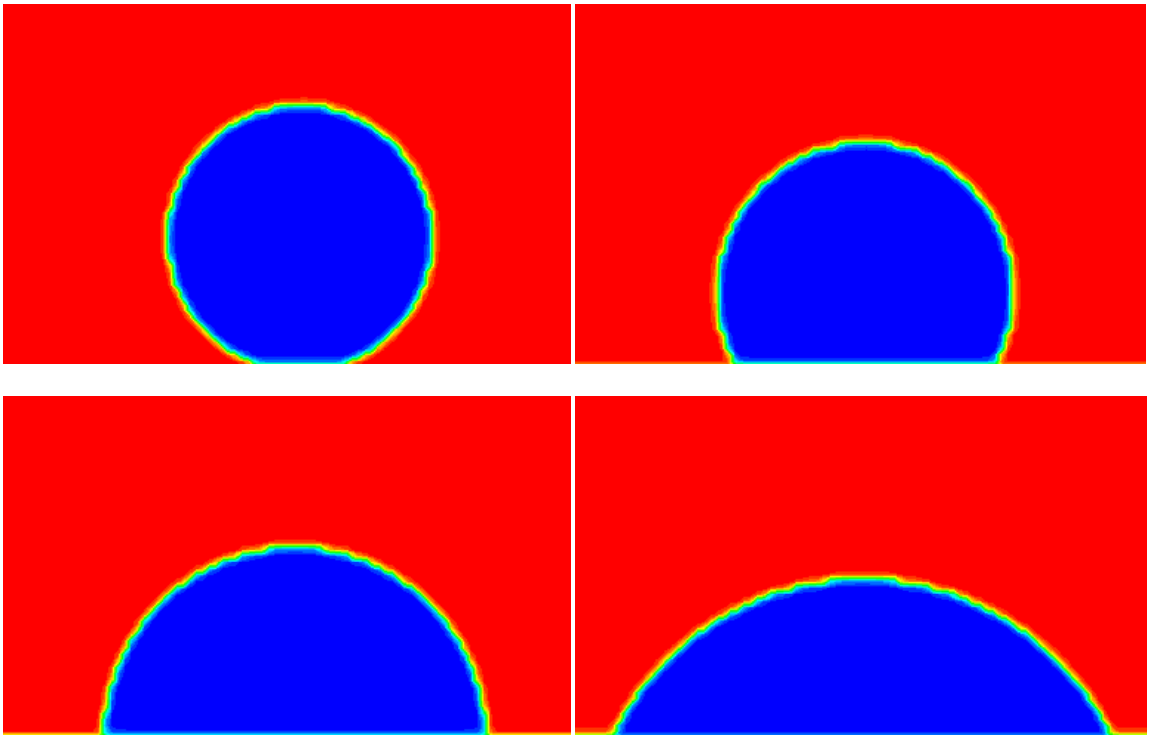

Figure 7 - Contact angles between phases with a solid surface (starting from top left to right), non-wetting, partially non-wetting, neutral wetting, and partially wetting

4.3 Flow Between Parallel Plates

A study of immiscible layered two-phase flow between two parallel plates is shown in Figure 8. Periodic boundaries are applied on the left and right and bounce-back (no-slip) boundary condition was applied on the top and bottom boundaries. The viscosity ratio between the fluid 1 and fluid 2 is set to be 10. The solution domain was set to be 102 units in height and 5 units in length. The small length has no effect on the solution as the body force was set to be small, 10^{-8}, such that the velocity does not exceed 0.3 lu(lattice unit)/lt (lattice time). The flow is driven by a body force, applied to the non-wetting phase and wetting phase, respectively. The analytical and simulated velocity profiles match nicely as seen in Figure 9 and Figure 10 (Huang et al. 2011), where $M = \frac{\mu_{non-wetting}}{\mu_{wetting}}$ equals 0.1 and 10, respectively. Good result comparisons between simulations and analytical solutions for relative permeability curves seen in Figure 11 were also obtained (Yiotis et al. 2007). This shows that the implementation is good at calculating velocity profiles and relative permeability curves.

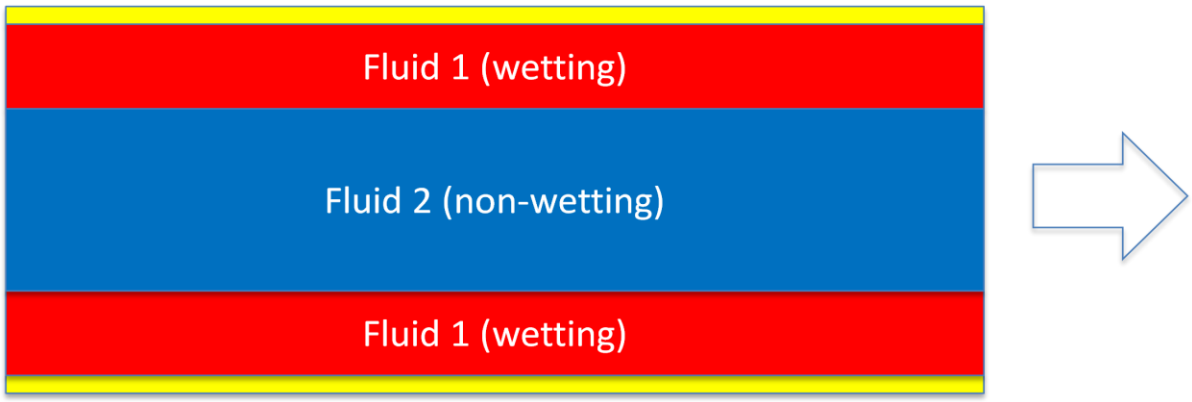

Figure 8 - Graphical description of immiscible flow between two parallel plates where fluid 1 is wetting phase and fluid 2 is non-wetting.

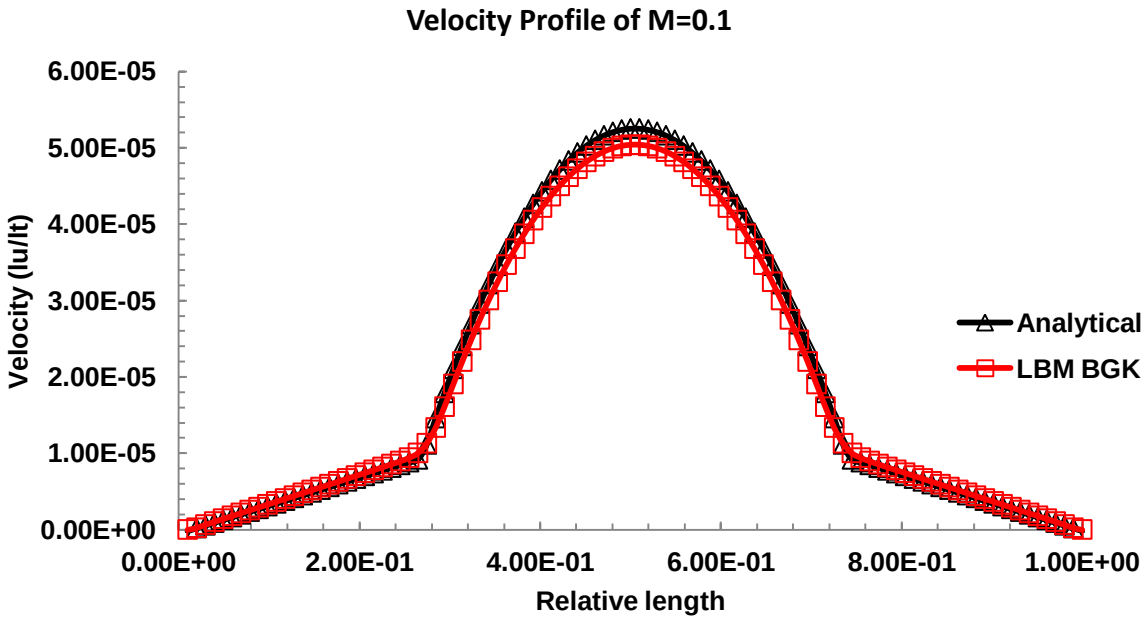

Figure 9 - Fluid velocity profile with wetting phase being more viscous by a factor of 10 (M=0.1)

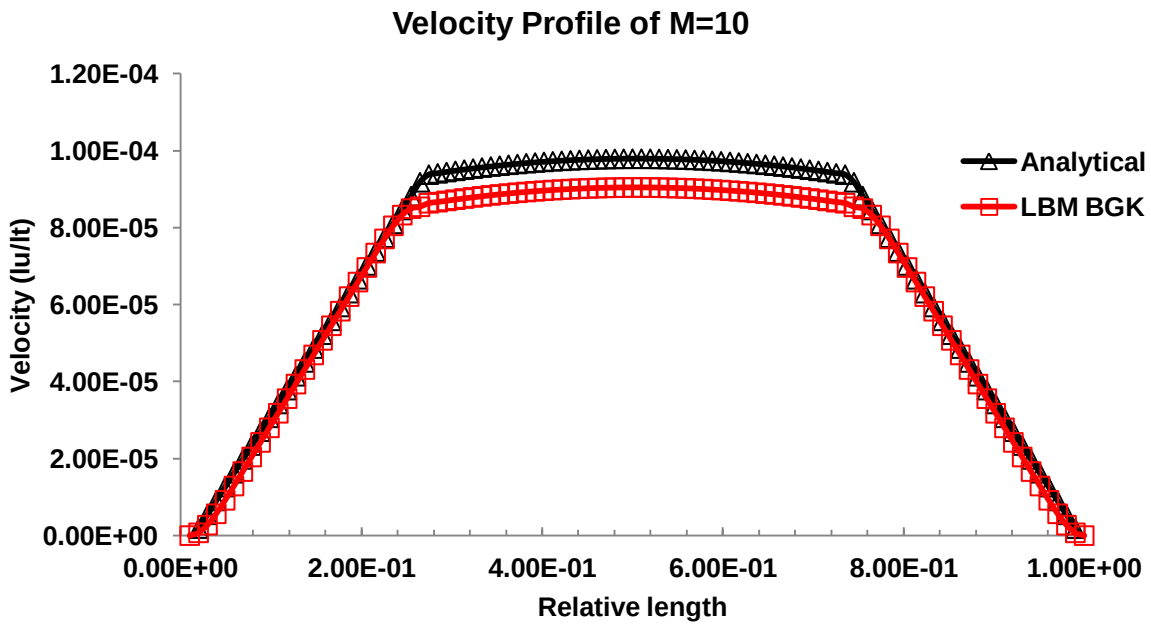

Figure 10 - Fluid velocity profile when non-wetting phase is more viscous by a factor of 10 (M=10)

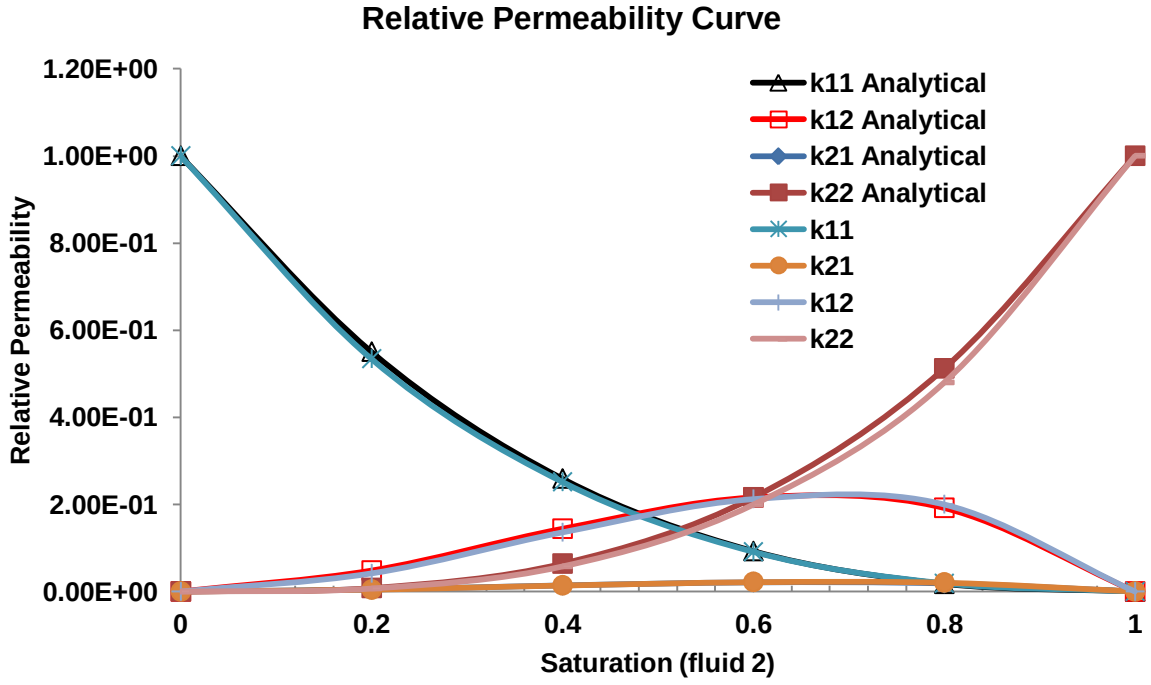

Figure 11 - Relative permeability curves for the two fluids and their analytical solutions

Chapter 5
Pore-Core-Field Results

5.1 Porous Media Generation

5.1.1 Problem Description

Lattice Boltzmann models have proved to be suitable tools to calculate permeability and relative permeability curves at the pore scale. To generate these medium, the medium generator based on 3D midpoint displacement method developed by Jonathan et al. (Jilesen et al. 2011) was used. The algorithm is sufficient in generating multiple realizations of porous geometries that match the properties of the medium such as specific area and porosity. For these geometries to be representatives of a porous media at the pore scale, the specific area and porosity must be uniform. They are periodic in all directions and will then be used for LBM simulations to obtain permeability and relative permeability data at the pore scale.

5.1.2 Computational Aspects

The porosities of the porous media realizations are set to be 0.2 in the simulations. This was chosen as the upper limit of the rock formations at Viking II found at the Wabamum Lake in Alberta, Canada (Survey 2006), at a depth of approximately 1342m. The resolution of the realizations were set to be 128^3, as this resolution can offer relatively computationally inexpensive simulations using LBM later on. The reduction factor, H, was set at 0.9, which ranged the specific surface areas to be between 0.04 to 0.06/unit.

5.1.3 Porous Media Realization Results

The realizations of these porous media are shown in Appendix A. The realizations that do not have meaningful simulation value, i.e. do not provide linkage space between one end to the other, were discarded. Note that it is not crucial to have realizations that "pass through" in all x, y, and z directions as this is probably also rare in real samples. These samples exist in lattice Boltzmann units, and thus need to be related to real units. It is crucial to select proper dimensions that satisfy the representative elementary volume (REV) so that the properties considered adequately satisfy the

macroscopic properties. Based on study done by Ovaysi et al. (Ovaysi and Piri 2010), the REV for that particular sandstone was found to be 0.6796 mm in each of the three dimensions, or 0.324 mm^3 in volume. Thus, it is satisfactory to dictate the dimension of the generated porous media to be 1mm in each dimension, meaning each lattice unit is 0.0078125mm. Although this dimension is larger than that of the traditional definition of pore scale, which is usually defined as dimensions less than that of the REV dimension (Zhang et al. 2000) (Meakin and Tartakovsky 2009), the term pore scale in this thesis is conveniently used to describe the geometries close to the lower threshold of the REV dimension. The core scale dimension is assumed to be in the order of centimeters and the field scale in the order of meters and larger in this study.

Each of these realizations has periodic boundary conditions in all directions but may not be physically connected within itself. This connectivity inside the porous media is crucial for flows to pass through; therefore, requires post processing to identify connections from one end to the other. A total of 10 porous medium were selected, each one with unique characteristics to represent a variety of structures that may exist in porous media in sandstones. Table 1 summarizes the directions fluids can flow through or not in the porous medium. However, in later sections, only two (x and y) of the three directions will be used, thus any geometries penetrable in the z-direction (geometries 1, 2, and 3) will become x-direction in the simulations.

Table 1 – Geometries and their impenetrableness in x-, y-, and z-directions

Geometry	X- Direction	Y- Direction	Z- Direction
1	Not penetrable	Not penetrable	Penetrable
2	Not penetrable	Not penetrable	Penetrable
3	Not penetrable	Not penetrable	Penetrable
4	Penetrable	Not penetrable	Not penetrable
5	Not penetrable	Penetrable	Not penetrable
6	Penetrable	Penetrable	Not penetrable
7	Penetrable	Penetrable	Not penetrable
8	Not penetrable	Penetrable	Not penetrable
9	Penetrable	Not penetrable	Not penetrable
10	Not penetrable	Penetrable	Not penetrable

5.2 Flow in Pore Scale Porous Media

5.2.1 Problem Description

Flows in porous media can be described by the Navier-Stokes equations and surface tension at the pore scale (Suekane et al. 2005). Carbon dioxide becomes a supercritical fluid at critical values of 304 K and 7.38 MPa, or depth of 700 m. At depth of 1.3 km, the density of the supercritical CO_2 is about 0.7 times that of water (Chiquet et al. 2007), and viscosity of 0.1 times that of water (Fenghour et al. 1998). The aim of this section is to improve our understanding of immiscible two-phase flow of water and supercritical CO_2 and to obtain useful information, specifically permeability and relative permeability curves for each porous media in x, y, and z-directions.

5.2.2 Computation Aspects

The domain size for each LBM simulation was 128^3, the dynamic viscosity of H_2O is $6.09 \times 10^{-4}\ Pa\ s$, and $6.08 \times 10^{-5}\ Pa\ s$ for CO_2, meaning the viscosity ratio of water to CO_2 is 10. The interfacial tension between the two fluids was found to be 0.0323 N/m (Chiquet et al. 2007), which is connected to the LBM unit by dimensionless parameters. The A parameter was chosen to be 0.04, and K was chosen to be 0.01 for stability reasons and to reduce the numbers of lattices at the interface to $5\sqrt{\frac{k}{A}} = 2.5$ lattice units wide (Kuzmin et al. 2011). The surface tension has a value of $\gamma = \sqrt{\frac{8kA}{9}} = 0.01886$. A body force of 3×10^{-4} was applied to drive the flow of both fluids with relaxation times of $\tau_{H_2O} = 2.5$ and $\tau_{CO_2} = 0.7$, which relates a kinematic viscosity ratio of 10. The applied body force is equivalent to a constant differential pressure of 5.72 kPa between the inlet and outlet, in line with experiments (Tölke 2002; Bennion and Bachu 2006; Egermann et al. 2006). In this LBM model, the densities of the two fluids are considered to be equal, which at this depth is not a bad assumption if viscous forces are more dominant as seen by the small values of Reynolds numbers in the orders of O(0.01)-O(0.1) (White 2006). On the other hand, the flows are not dominated by capillary forces as the capillary numbers are constant and are much greater than 10^{-5}.

The magic parameter for the two relaxation time scheme was set as $\Lambda = \frac{1}{12}$ in order to obtain the best advection results. The contact angle for water and the surface is assumed to be 60°, adjusting the "phase" of the wall to 0.5, where $\phi_{H_2O} = 1$ and $\phi_{CO_2} = -1$.

No-slip bounce-back conditions are applied to the boundary faces parallel to the direction of the applied force. Periodic boundary conditions are prescribed to the inlet and outlet faces. This is similar to the work done by Ramstad et al. (Ramstad et al. 2010), where the exiting wetting fluid changes to non-wetting fluid and re-injected at inlet face, mimicking a constant invasive supply of CO_2. The geometries that Ramstad et al. worked with were not of periodic nature; hence, needed four extra cells at the inlet and outlet faces of the model for the flow to adjust to reentry. This is not needed for our simulations as the geometries are periodic during construction.

5.2.3 Permeability Results

In this problem, unsteady relative permeability calculations are desired to take advantage of the strength of LBM. Unsteady state method for calculating relative permeability is the least time-consuming because it allows the values of relative permeability to be determined dynamically (Li et al. 2005). In particular, only drainage relative permeability curves as CO_2 displacing water is of primary concern. During the drainage process, the porous media would be filled with water and CO_2 would enter the porous medium and displace the water; however, over time, it reaches a point where water becomes trapped in the medium and no more water would be displaced (dead water), this point of saturation of irreducible wetting phase is denoted by S_{wi}. The measurements of flow rates for both fluids are collected until S_{wi} is reached (Bennion 2005; Müller 2011). It was difficult to use a general convergence criterion. In single phase, this was calculated based on the change in flow rates. Consequently, this criterion was applied in each phase $\Delta q = \frac{q(t)-q(t-\Delta t)}{q(t-1)} \leq \varepsilon$, which was used to calculate if the system had reached steady state. The value of ε was chosen to be 10^{-6} after 100,000-120,000 time steps (Gunstensen 1992). These criteria were determined based on numerical experiments.

The Reynolds and Capillary numbers for each pore geometries in their x and y directions are shown in the Table 2, with the maximum Reynolds number of 0.16906 and the minimum of 0.00654, which are sufficiently low that the simulations are well within the valid region of Darcy's Law, meaning viscous effects are prevalent. The Capillary numbers are independent of the simulation results while allowing the Reynolds numbers to be dependent. Controlling the body force is crucial in balancing stability and simulation time. It was also worth noting that when the body force is small, minuscule amount of CO_2 can leak over to the outlet due to the periodic nature. This phenomenon was ignored

as it did not affect the flow physics. If flows of low Capillary numbers are desired, a buffering spacing of voids should be used as done by Ramstad et al. (Ramstad et al. 2010).

The calculated permeability values in LBM units and real units are shown in Table 3. These permeability values were plotted against the minimum diameters of the channels, seen in Figure 12. There is a positive trend of increasing minimum diameter and permeability. This can be explained by the fact that some of these channels act as the only link between the inlet and the outlet. The wide data spread is due to the large degree of variation in structure and property. This is similar to the concept of permeability and pore size discussed in the works by Bennion et al. (Bennion et al. 2006).

Table 2 – Reynolds and Capillary numbers applied in each simulation

Geometry	Stream-wise Direction	Reynolds Number	Capillary Number
1	x	0.02067	0.01591
2	x	0.05496	0.01591
3	x	0.02137	0.01591
4	x	0.09575	0.01591
5	y	0.04079	0.01591
6	x	0.02157	0.01591
6	y	0.02457	0.01591
7	x	0.00654	0.01591
7	y	0.04327	0.01591
8	y	0.16906	0.01591
9	x	0.01134	0.01591
10	y	0.07075	0.01591

Table 3 – Permeability in each direction in both LBM and real units

Geometry	Permeability to Water (LBM units)		Permeability to Water (mD)	
	X- Direction	Y- Direction	X- Direction	Y- Direction
1	1.0207	0	3.8925	0
2	2.3265	0	8.8723	0
3	1.2662	0	4.8288	0
4	3.5463	0	13.5239	0
5	0	1.7266	0	6.5843
6	0.9129	1.2133	3.4813	4.6269
7	0.4846	1.6026	1.8481	6.1117
8	0	4.5538	0	17.3659
9	0.5598	0	2.1347	0
10	0	2.6205	0	9.9934

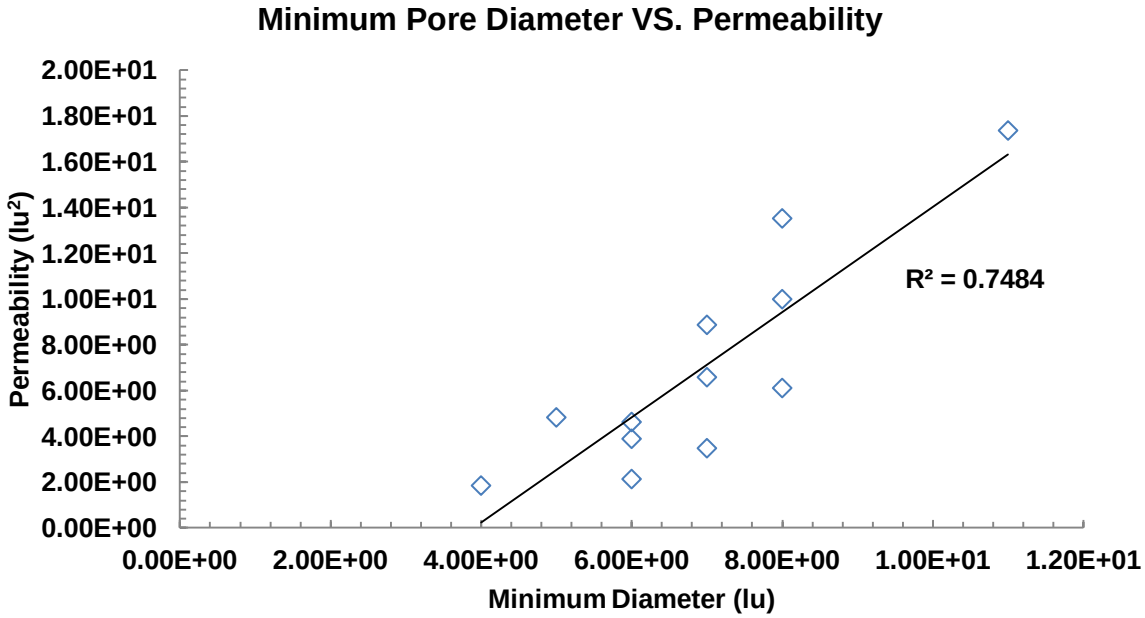

Figure 12 – Minimum pore diameter and their relations to permeability in LBM units

5.2.4 Relative Permeability Results

Figure 13 to Figure 22 show the relative permeability curves for the ten geometries. The permeability data in the figures are presented in saturation increments of 0.1 and this format will be used in later processing to reduce computational cost. Figure 13 shows the permeability curves for the first geometry in the x-direction, with the S_{wi} at 0.56. Figure 14 shows the permeability curves for the second geometry in the x-direction, with the S_{wi} at 0.67. Figure 15 shows the permeability curves for the third geometry in the x-direction, with the S_{wi} at 0.61. Figure 16 shows the permeability curves for the forth geometry in the x-direction, with the S_{wi} at 0.72. Figure 17 shows the permeability curves for the fifth geometry in the y-direction, with the S_{wi} at 0.65. Figure 18 shows the permeability curves for the sixth geometry in the x and y-directions, with the S_{wi} at 0.59 and 0.60, respectively. Figure 19 shows the permeability curves for the seventh geometry in the x-direction, with the S_{wi} at 0.70 and 0.79, respectively. It is important to note that the relative permeability curves for the same geometry may vary quite differently in different directions. Figure 20 shows the permeability curves for the eighth geometry in the y-direction, with the S_{wi} at 0.75. Figure 21 shows the permeability curves for the ninth geometry in the x-direction, with the S_{wi} at 0.60. Figure 22 shows the permeability curves for the tenth geometry in the y-direction, with the S_{wi} at 0.67. Figure 23 shows the distribution of the CO_2 phase pushing into the porous media at time step of 4,000 in the sixth geometry. Figure 24 shows the distribution of CO_2 at time step of 20,000 showing the incremental filling of the medium by CO_2. Figure 25 shows the displacement after 100,000 time steps, resulting in a complete push through of the CO_2 phase.

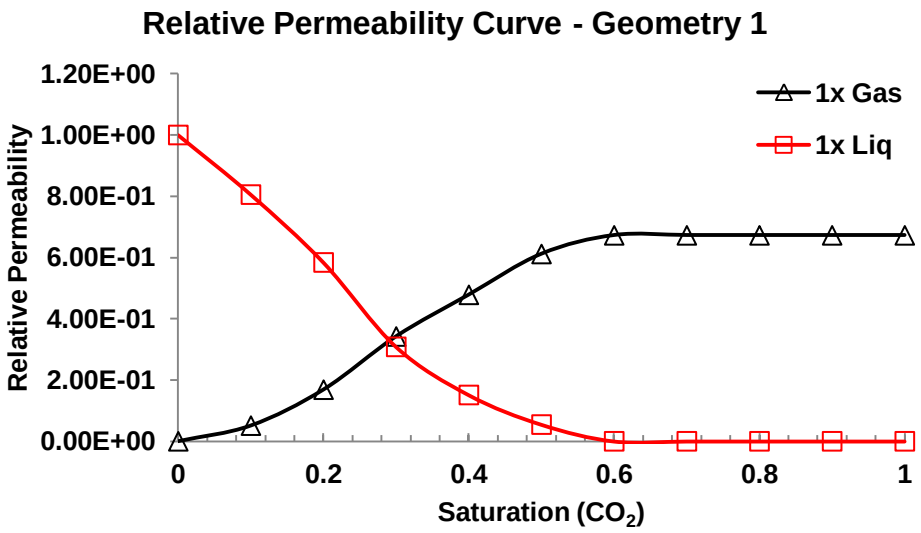

Figure 13 - Relative permeability curves for geometry 1

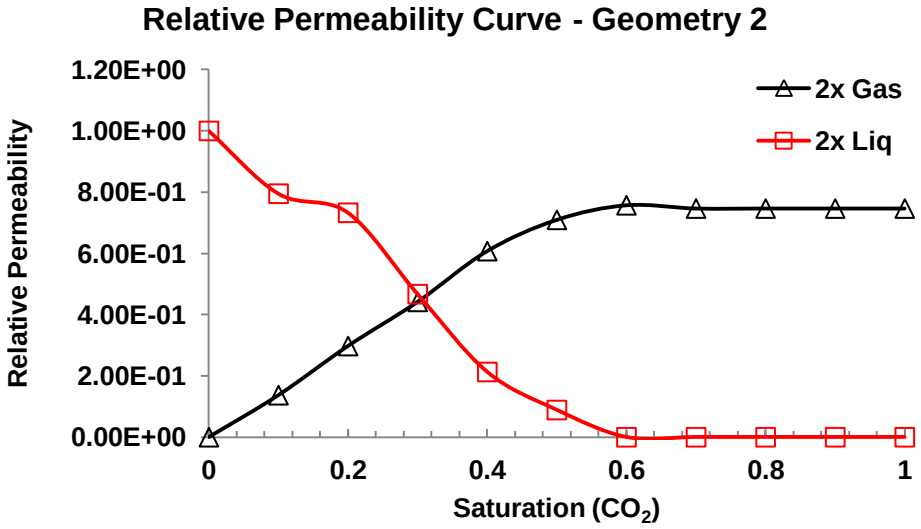

Figure 14 - Relative permeability curves for geometry 2

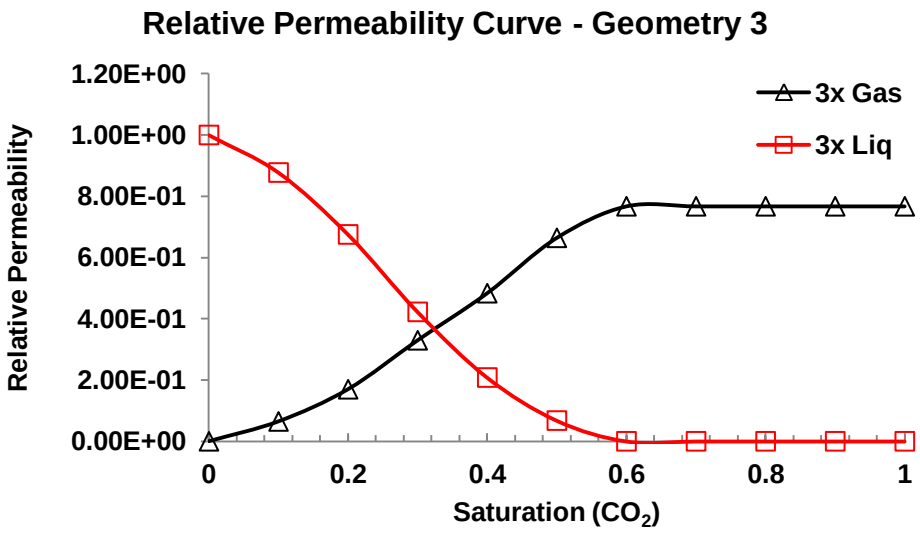

Figure 15 - Relative permeability curves for geometry 3

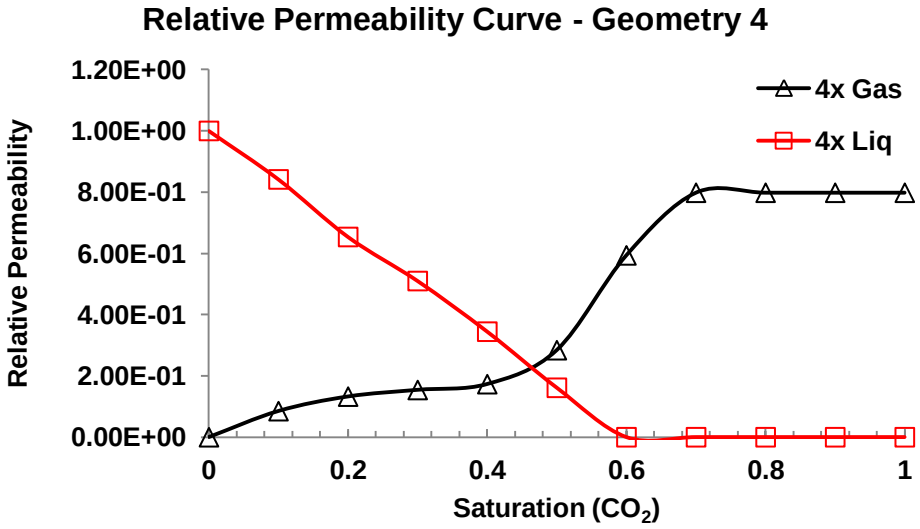

Figure 16 - Relative permeability curves for geometry 4

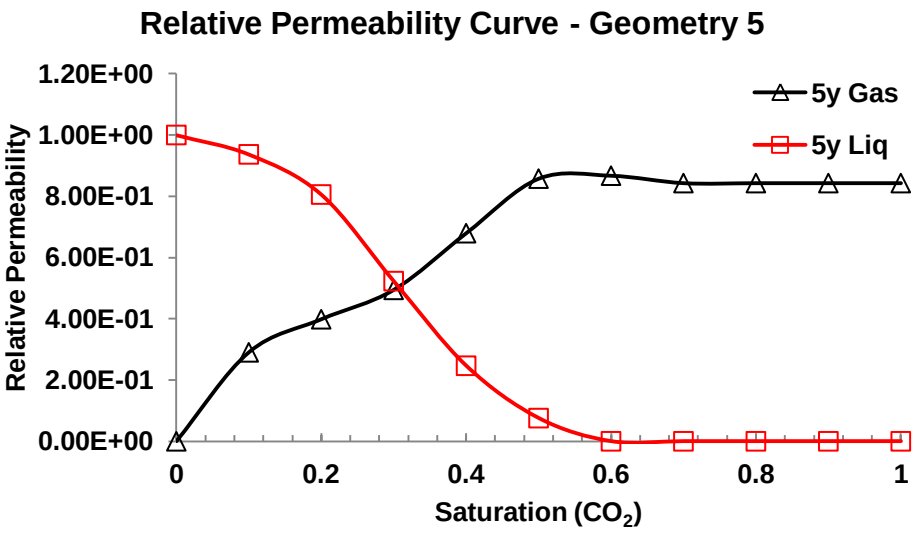

Figure 17 - Relative permeability curves for geometry 5

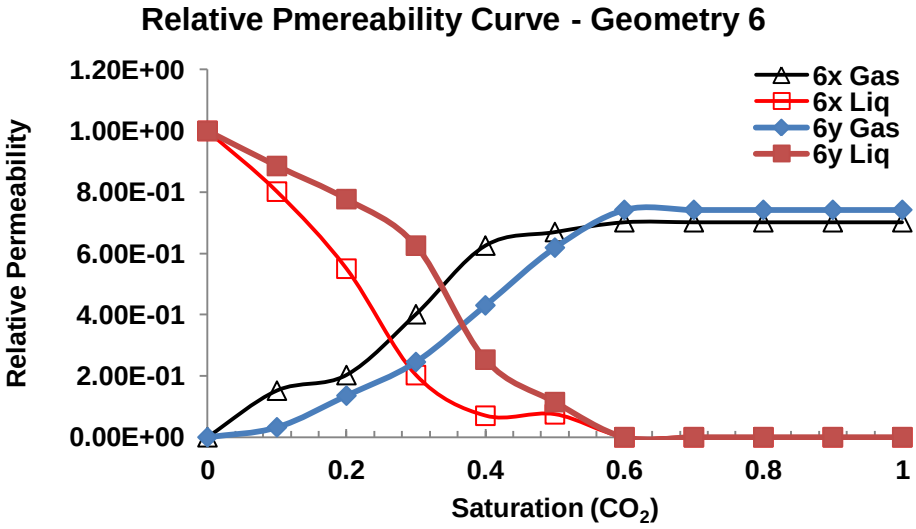

Figure 18 - Relative permeability curves for geometry 6

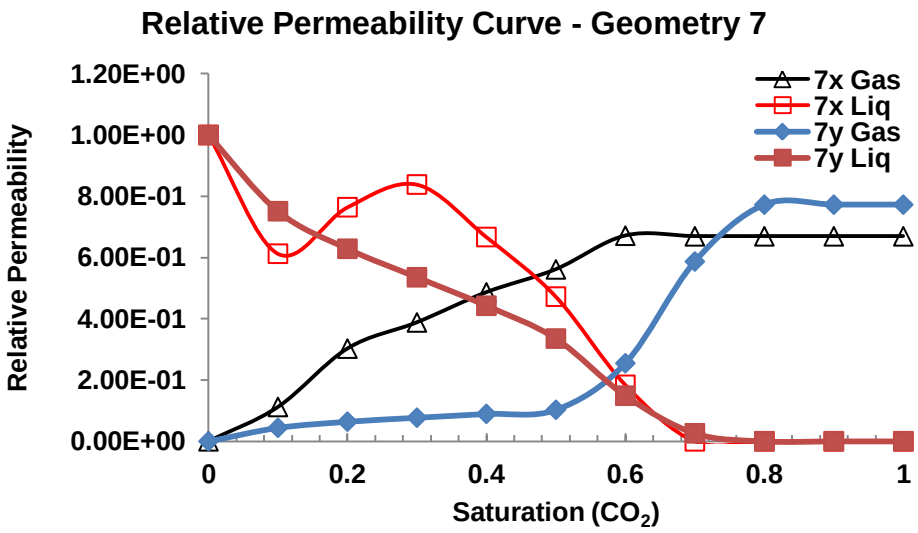

Figure 19 - Relative permeability curves for geometry 7

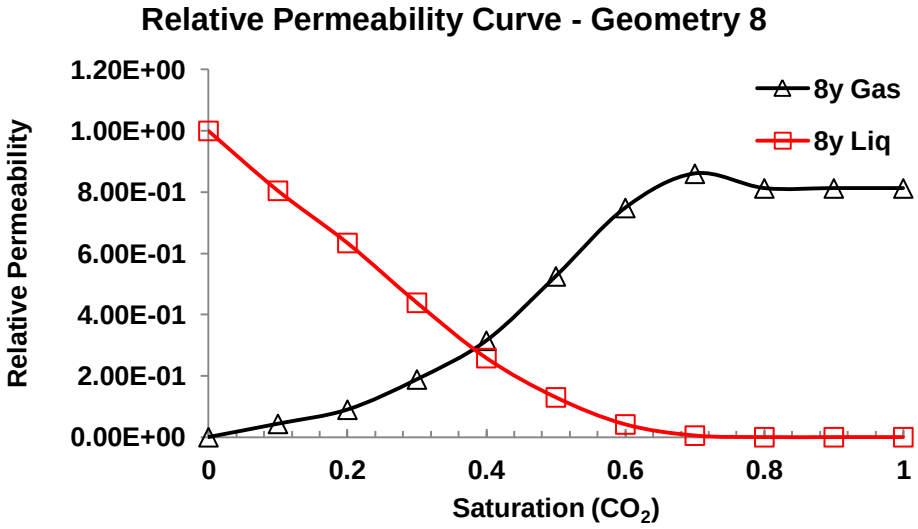

Figure 20 - Relative permeability curves for geometry 8

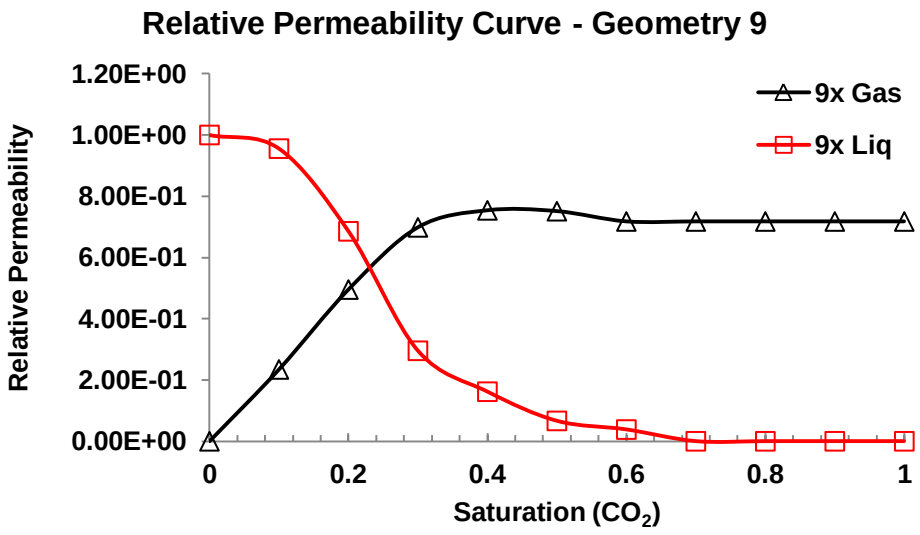

Figure 21 - Relative permeability curves for geometry 9

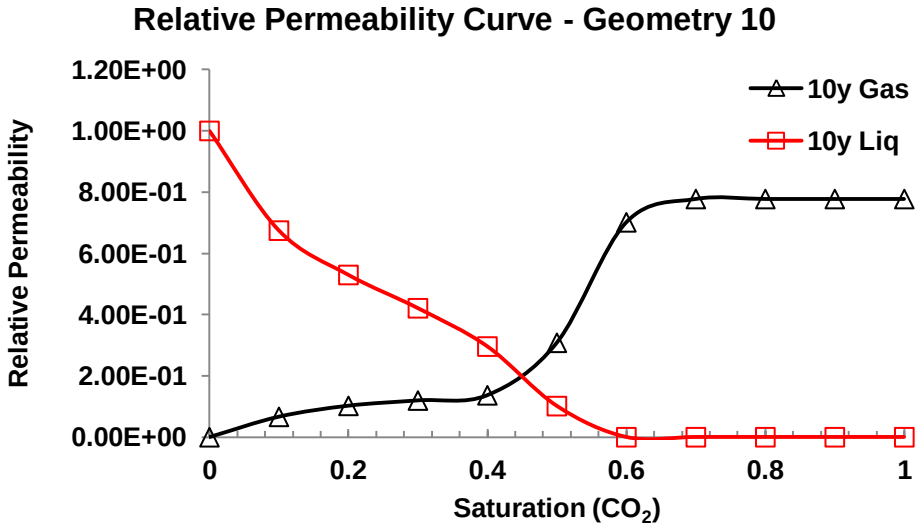

Figure 22 - Relative permeability curves for geometry 10

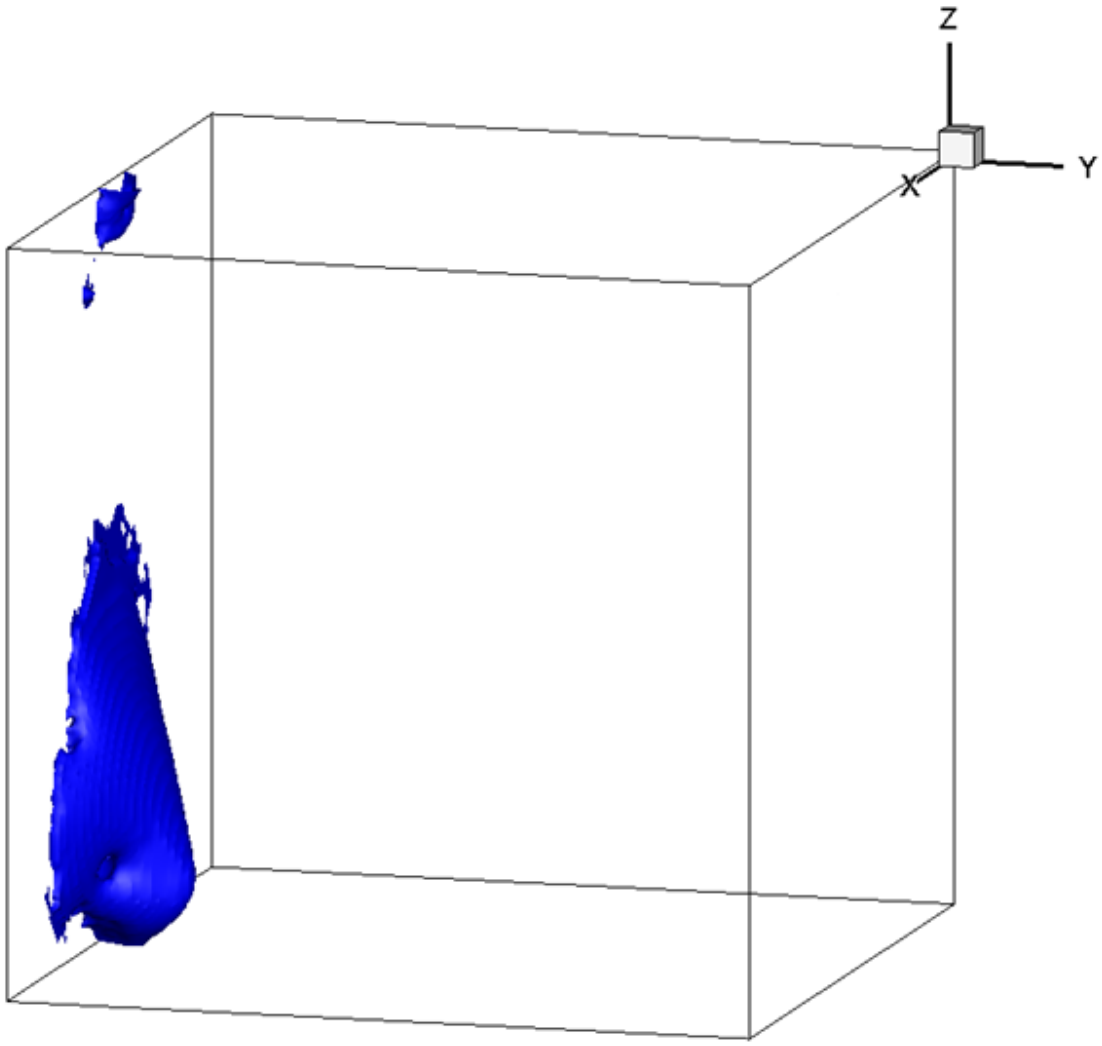

Figure 23 - Distribution of the CO_2 phase pushing into the porous media at time step of 4,000 for geometry 6

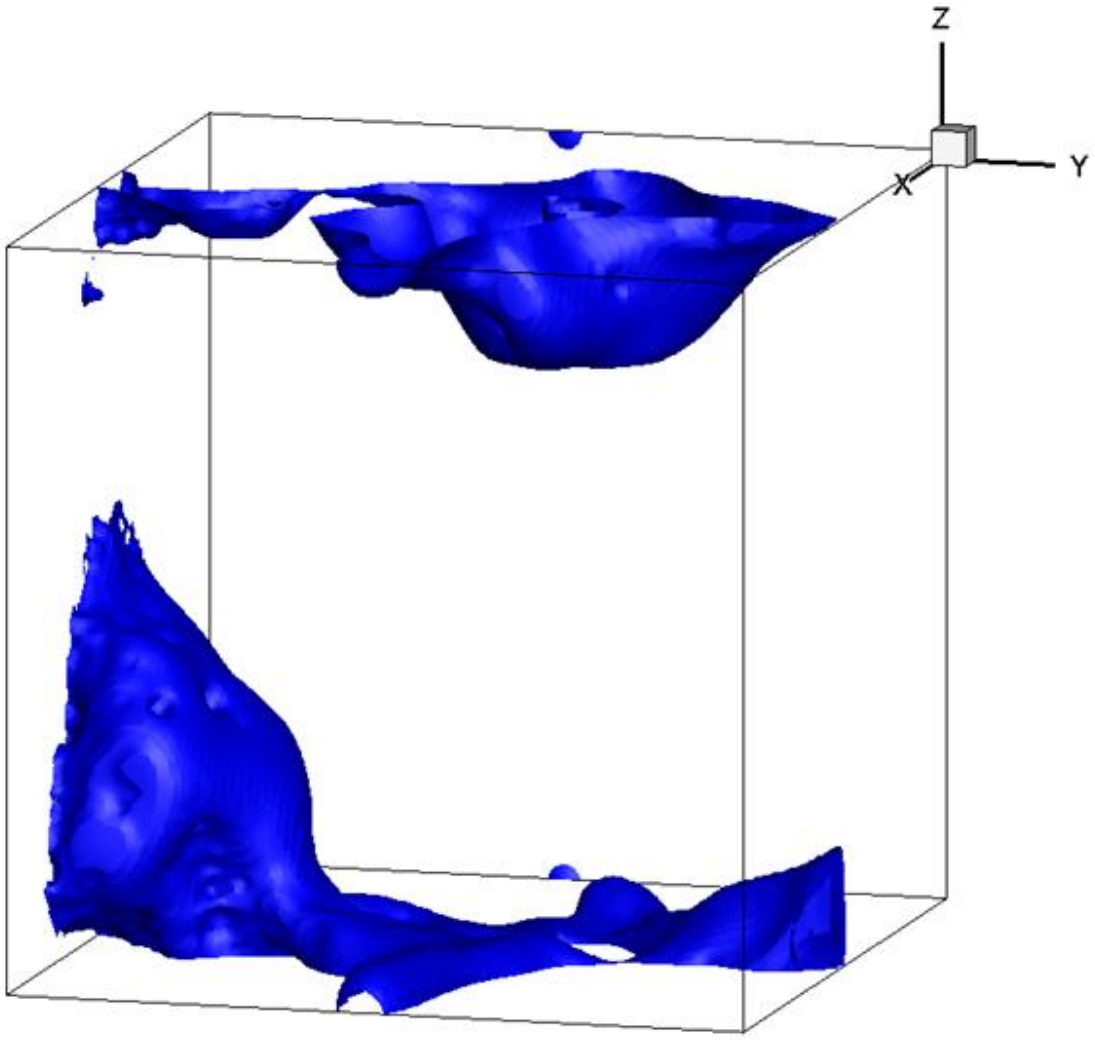

Figure 24 - Distribution of the CO_2 phase pushing into the porous media at time step of 20,000 for geometry 6

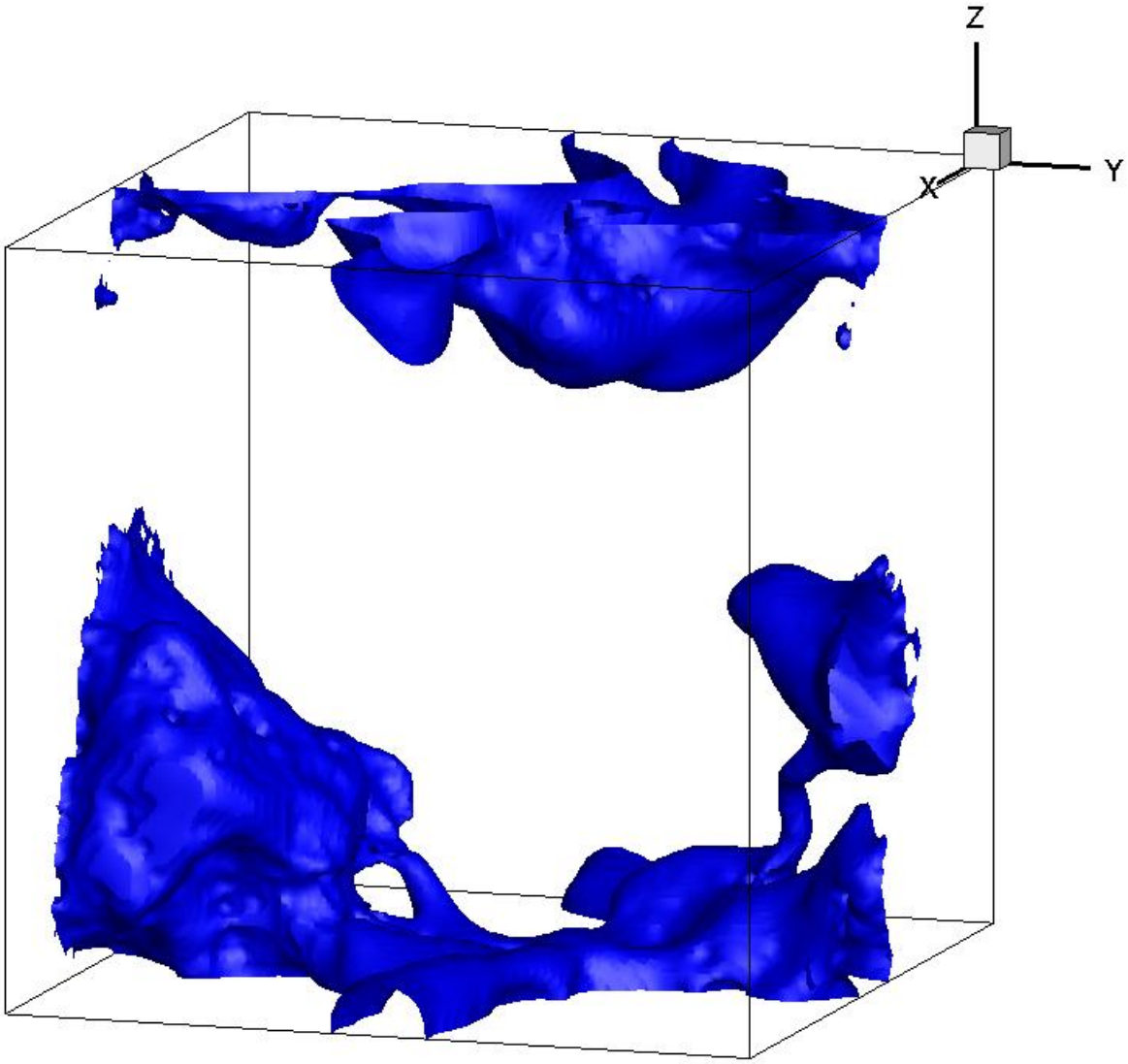

Figure 25 - Distribution of the CO_2 phase pushing into the porous media at time step of 100,000 for geometry 6

5.3 Field Kriging

5.3.1 Problem Description

The idea of this section is to move beyond the relative permeability and permeability calculations at the pore scales already done in the literature and to incorporate the pore scale results into practical

applications. The pore scale results can be used to generate a field of data. This is done by placing the pore samples in a structured form in a structured grid in two-dimensional space. The domain size is limited by computational resources and is set to 1024x3072, which is scaled to 1.024m by 3.072m as each unit has dimension of 1mm. The dimensions were selected to utilize the maximum computing resources. Two fields were generated in this section. The features of the kriged permeability fields in x- and y- directions are important as "cores" and "pore" samples would be taken from these fields for reconstruction of these fields. This is summarized in Figure 26.

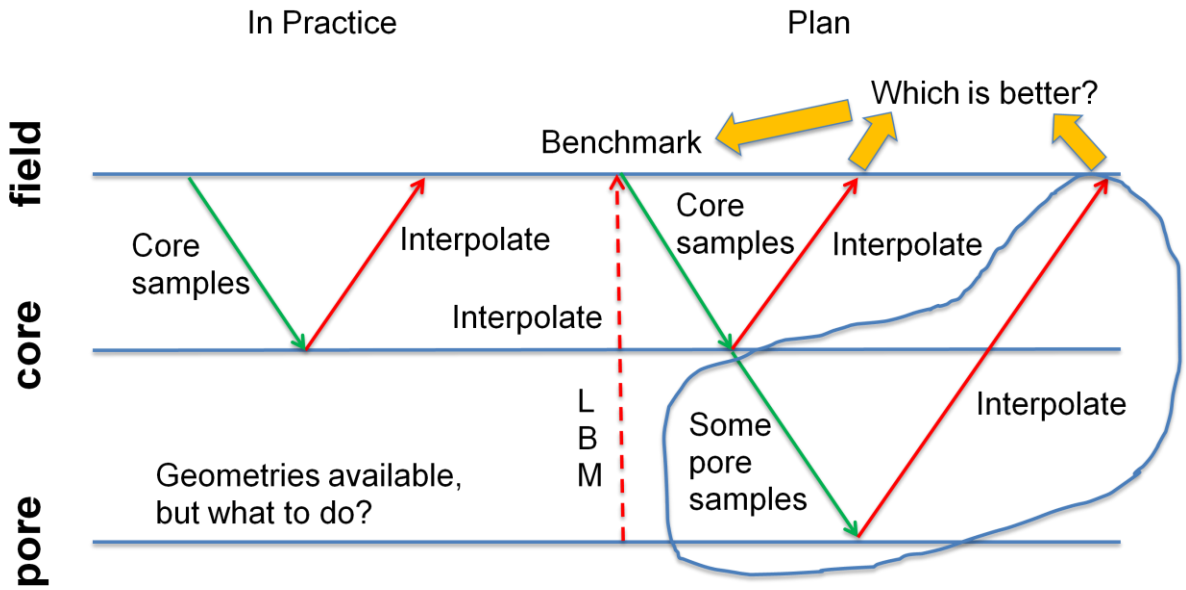

Figure 26 - Graphical representation of current methodology and proposed methodology

5.3.2 Computational Aspects

The permeability and the relative permeability data was kriged using Tecplot. The fractional diagonal distance beyond which sources become statistically insignificant is 0.3. The semi-variance at each source data on a normalized scale was set to be 0. There was no drift in the overall trend. All the source points were considered in the interpolation (Tecplot 2006). Two fields of permeability and relative permeability curves were created for comparison. The structured coordinates in which the pores are placed for field 1 are shown in Table 4 and Figure 27. The structured coordinates in which the pores are placed for field 2 are shown in Table 5 and Figure 28.

Table 4 – Locations in which the LBM results are placed to generate benchmark field 1

Pore Geometry Number	X-coordinate	Y-coordinate
1	384	512
2	768	256
3	768	768
4	1152	512
5	1536	256
6	1536	768
7	1920	512
8	2304	256
9	2304	768
10	2688	512

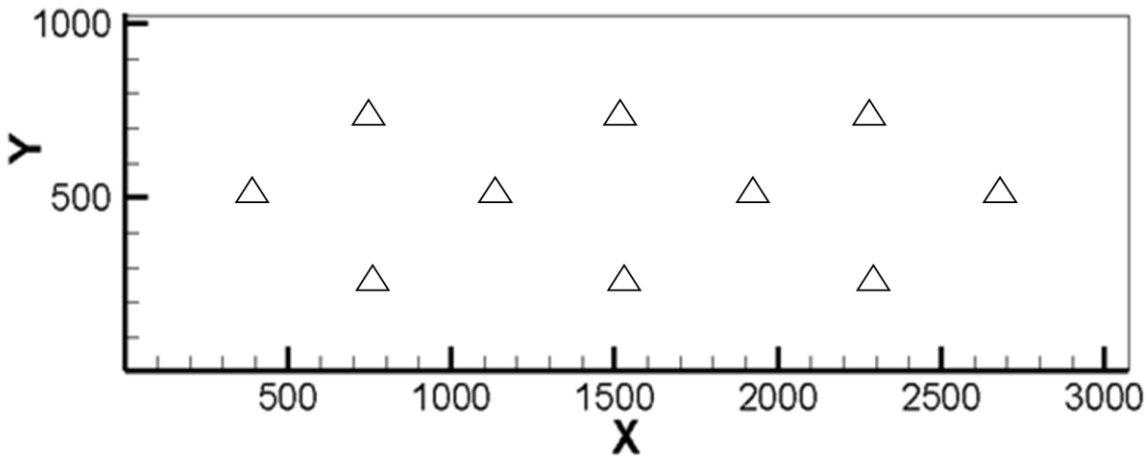

Figure 27 - LBM results placements for field 1 kriging

Table 5 – Locations in which the LBM results are placed to generate benchmark field 2

Pore Geometry Number	X-coordinate	Y-coordinate
1	1	1
2	1536	1
3	3072	1
4	1	512
5	1024	512
6	2048	512
7	3072	512
8	1	1024
9	1536	1024
10	3072	1024

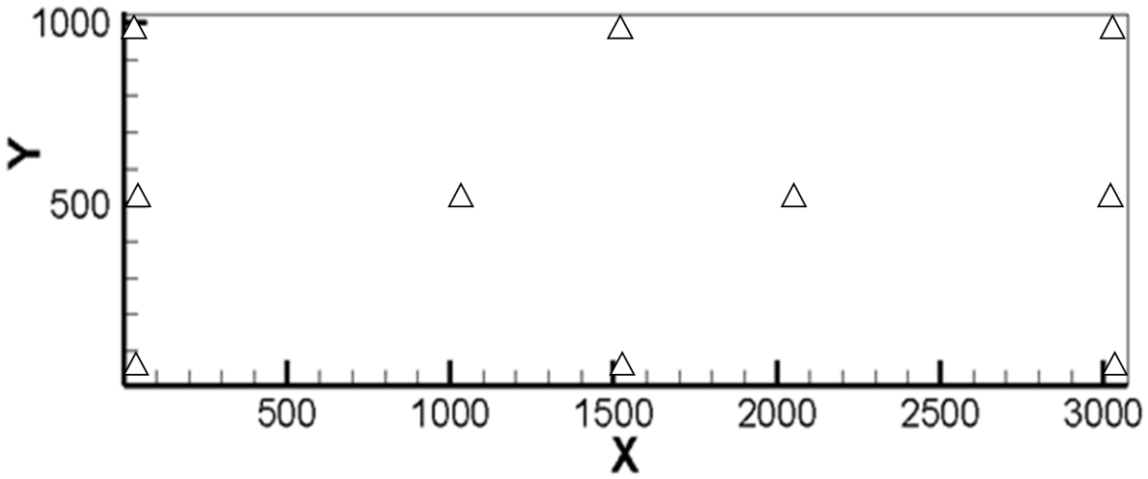

Figure 28 - LBM results placements for field 2 kriging

5.3.3 Field Results

Figure 29 and Figure 30 show the kriged permeability field created by these pore scale results in x- and y-directions. Embedded in these results are their relative permeability curves, thus, it is possible to retrieve permeability and relative permeability results in each of the 3072x1024 pores in the generated field. The small and sudden changes in x- and y-directional permeability fields are ideal for testing the accuracy of the reconstructions.

Figure 31 and Figure 32 show the kriged permeability fields created by these pore scale results in x- and y-directions. The generated field produced different features and hence a different scenario than that of field 1. This also meant that the key features of field 1 and field 2 should lie close to the locations of the 10 source points as they are responsible for the maximum and minimum features. These important features will pose challenges to how the reconstructions based on "pore" and "core" samples are extracted, and the results will naturally be location dependent.

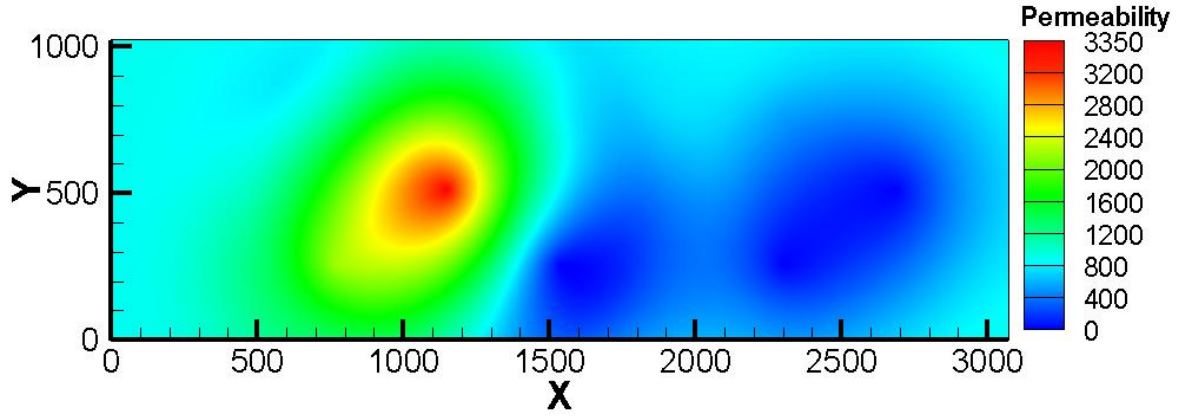

Figure 29 – Permeability field for benchmark field 1 in x-direction

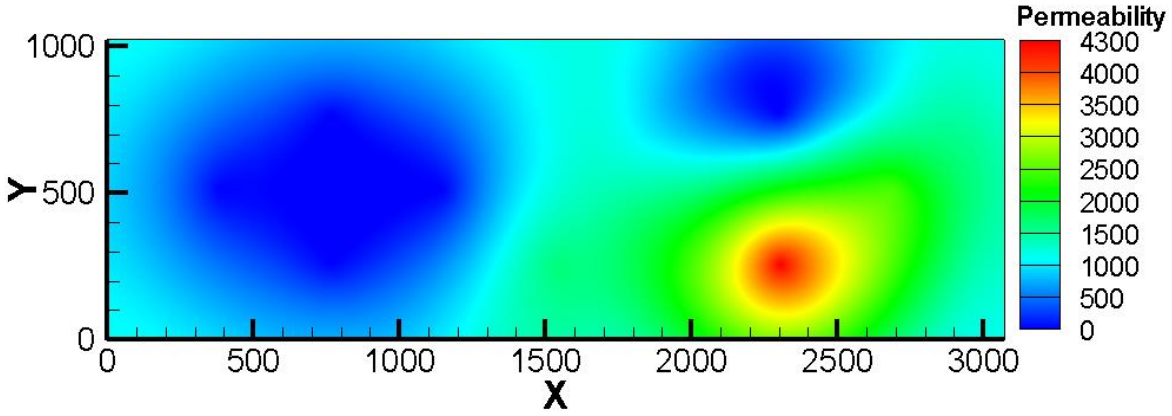

Figure 30 – Permeability field for benchmark field 1 in y-direction

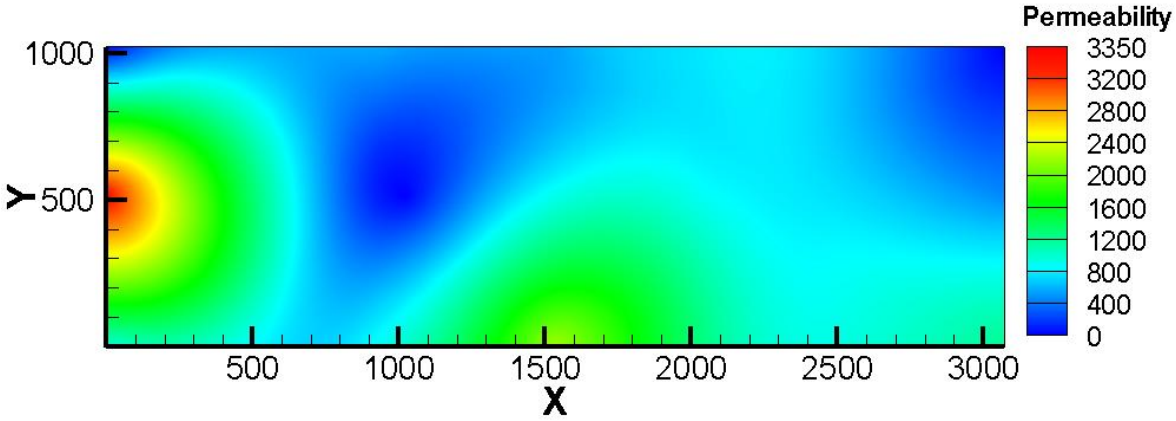

Figure 31 – Permeability field for benchmark field 2 in x-direction

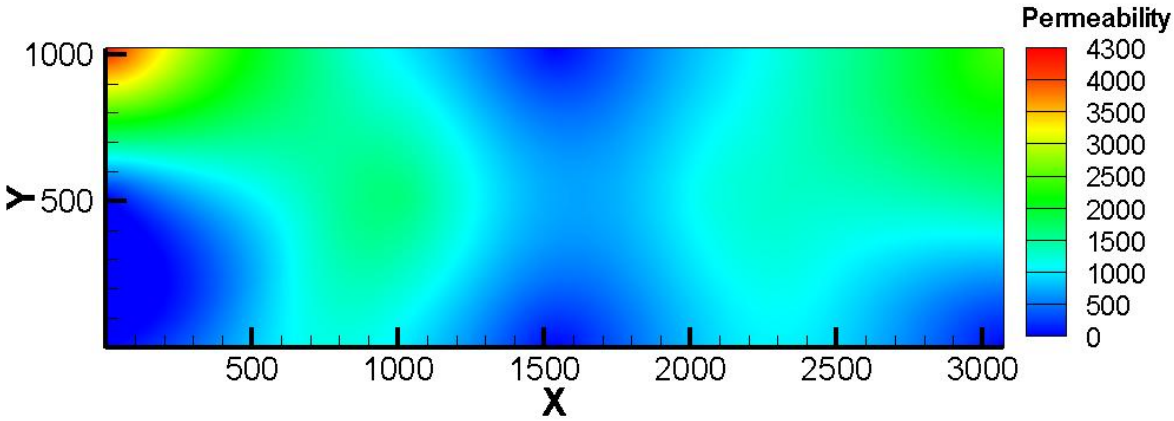

Figure 32 – Permeability field for benchmark field 2 in y-direction

5.4 Core Samples

5.4.1 Problem Description

The benchmark fields have been created for analysis. Core samples are important in field practices because they provide insight to the formation and structures of the subsurface. In practice, these cores are extracted, upscaled (measured macroscopically), and then kriged to create an approximation of the overall subsurface geological formation. It is impossible to extract enough samples in the ground to provide complete description of the geological characteristics.

5.4.2 Computational Aspects

The core samples are extracted from the benchmark fields for analysis. In this section, the focus is on obtaining 18 core samples sized 64x64, corresponding to 6.4 cm per side for each core. Figure 33 shows the locations of the cores on the map and Table 6 shows the coordinates for each core.

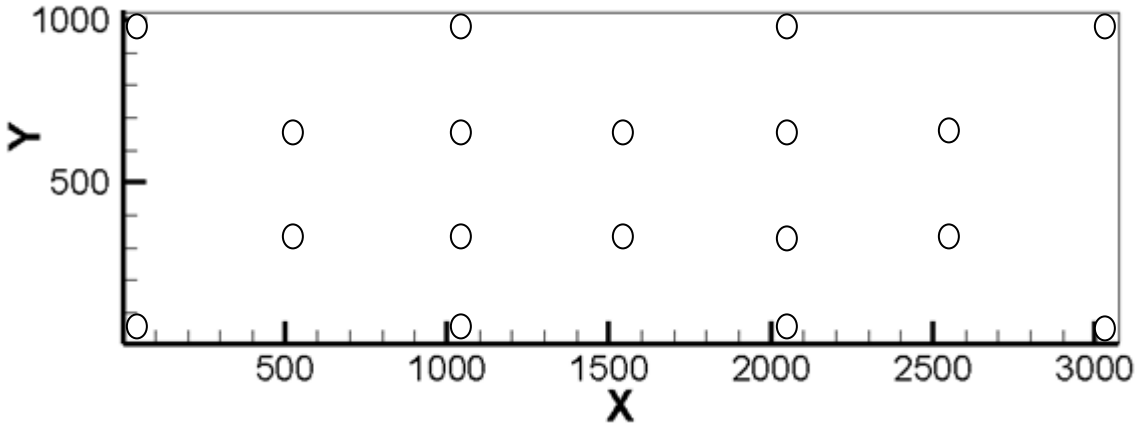

Figure 33 – Placement of the extracted cores for both fields

Table 6 – X- and y-coordinates of the extracted cores for both fields

Core Geometry Number	X-coordinate	Y-coordinate
1	$480 \leq x < 544$	$309 \leq y < 373$
2	$992 \leq x < 1056$	$309 \leq y < 373$
3	$1504 \leq x < 1568$	$309 \leq y < 373$
4	$2016 \leq x < 2080$	$309 \leq y < 373$
5	$2528 \leq x < 2592$	$309 \leq y < 373$
6	$480 \leq x < 544$	$651 \leq y < 715$
7	$992 \leq x < 1056$	$651 \leq y < 715$
8	$1504 \leq x < 1568$	$651 \leq y < 715$
9	$2016 \leq x < 2080$	$651 \leq y < 715$
10	$2528 \leq x < 2592$	$651 \leq y < 715$
11	$1 \leq x < 65$	$1 \leq y < 65$
12	$992 \leq x < 1056$	$1 \leq y < 65$
13	$2016 \leq x < 2080$	$1 \leq y < 65$
14	$3008 \leq x < 3072$	$1 \leq y < 65$
15	$1 \leq x < 65$	$960 < y \leq 1024$
16	$992 \leq x < 1056$	$960 < y \leq 1024$
17	$2016 \leq x < 2080$	$960 < y \leq 1024$
18	$3008 \leq x < 3072$	$960 < y \leq 1024$

5.5 Core Kriging

5.5.1 Problem Description

In the previous section, core samples were extracted from the benchmark fields. One of the difficulties in utilizing these core samples is how to express the properties, specifically permeability and relative permeability data embedded in the samples. In experimental practices, core analysis would be conducted on the samples to obtain overall properties of these samples. In this numerical experiment, these pore scale properties would be upscaled using the renormalization method to obtain overall permeability and equivalent relative permeability curve for that particular core. Afterwards, the upscaled core data would be used to interpolate new fields.

5.5.2 Computational Aspects

Each of the core samples (sized 64x64 pores) would be subjected to upscaling. This is done by first upscaling the sample to 32x32, 16x16, 8x8, 4x4, 2x2, and finally 1x1 using the renormalization formula. The collection of 1x1 data on permeability and relative permeability for the 18 core samples can then be used to reconstruct the fields for comparisons by placing them into the locations where the cores were extracted. The core kriging was done in Tecplot (Tecplot 2006) under the kriging interpolation function. The input value for the fractional diagonal distance beyond which sources become statistically insignificant is 0.3. The semi-variance at each source data on a normalized scale was set to be 0. There was no drift in the overall trend. All source points were considered in the interpolation; however the weights of their significance are automatically determined by Tecplot (Tecplot 2006). The field 1 permeability results are shown in Figure 34 and Figure 35 in x- and y-directions. Figure 36 and Figure 37 show the permeability results for field 2 in x- and y-directions. These results will be discussed in later sections. Note that the kriging method used is the simplest and consistent with the kriging method in which LBM results were used to create these benchmarks. This is done to allow fair comparisons between the results.

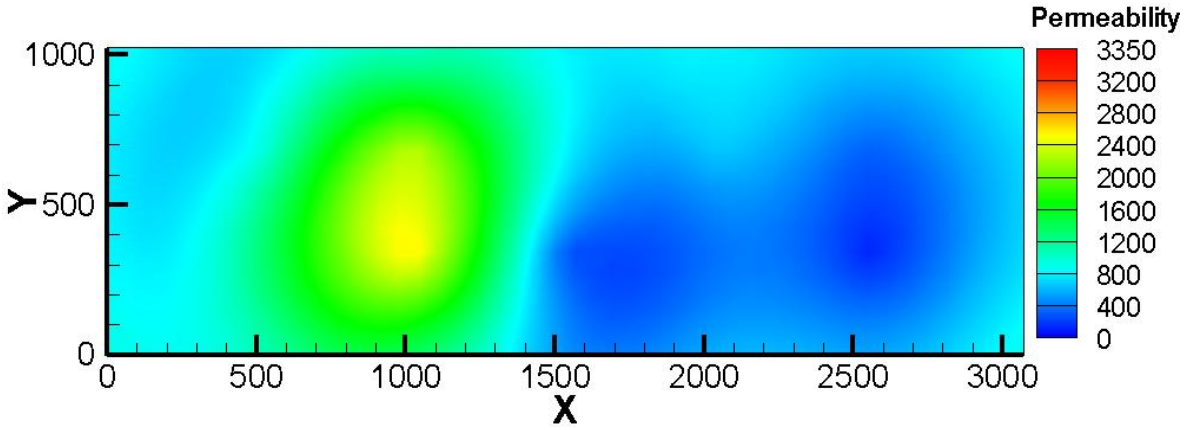

Figure 34 – Permeability field in the x-direction of field 1 using core kriging

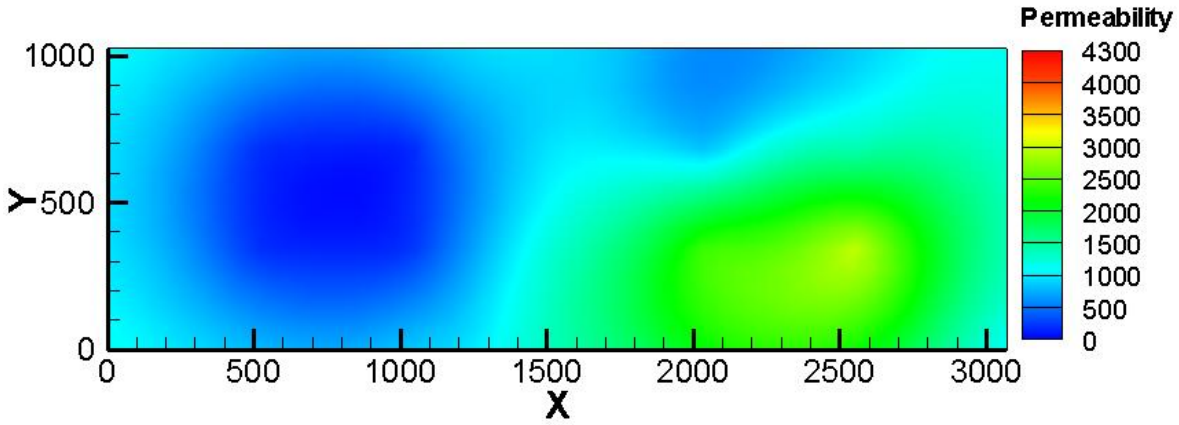

Figure 35 – Permeability field in the y-direction of field 1 using core kriging

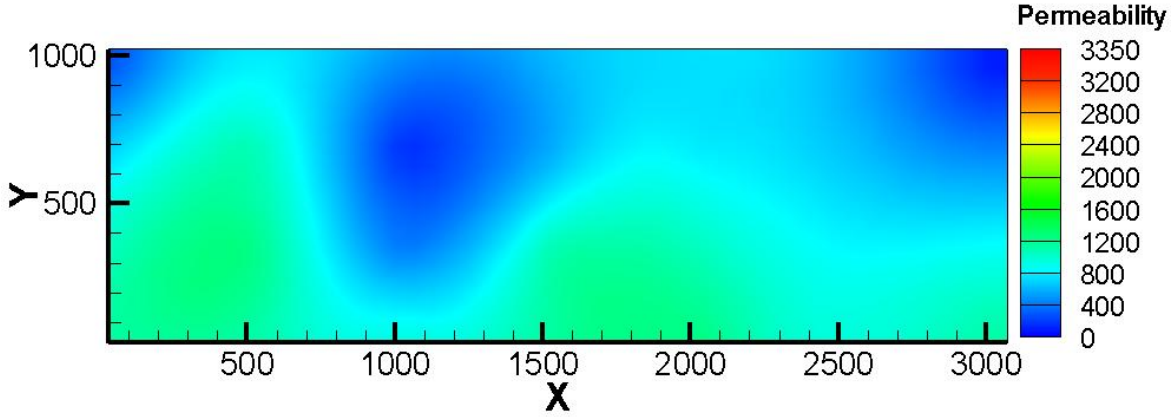

Figure 36 – Permeability field in the x-direction of field 2 using core kriging

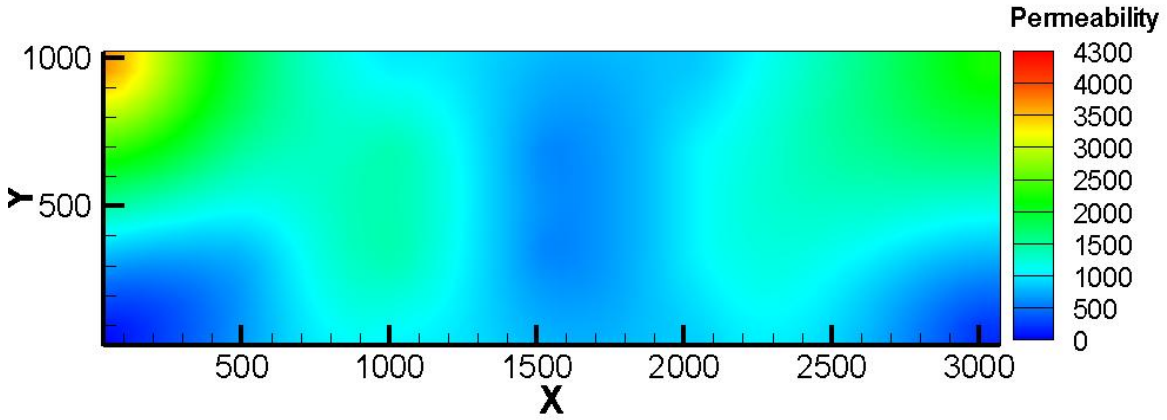

Figure 37 – Permeability field in the y-direction of field 2 using core kriging

5.6 Pore Kriging

5.6.1 Problem Description

The core samples are extracted from the benchmark fields for analysis. In this section, the focus is on obtaining pore samples from each of the core samples sized 6.4 cm x 6.4 cm. The idea is that the dimensions of these pore samples are at the lower threshold of REV, making them ideal for carrying out analysis that would describe the local distributions in these cores. The upscaled core data makes the assumption that the upscaled parameters are representative of the core while ignoring information at the local level. For each core sample, nine samples are extracted from them, meaning a total of 162 pore samples are extracted from 18 cores. The locations of the nine pore samples extracted are structured so that the distances between samples are spaced evenly, shown in Figure 38, and their local coordinates listed in Table 7. The global coordinates for every pore in each core are listed in Appendix B.

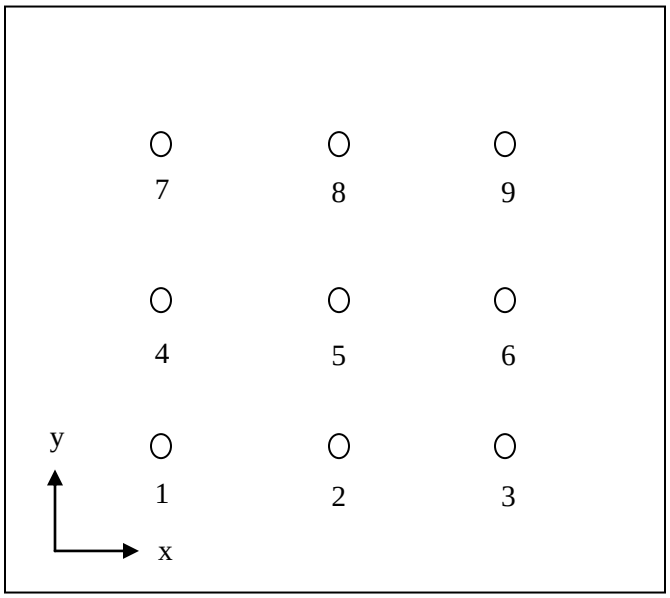

Figure 38 – Locations of pore samples extracted in a core sample

Table 7 – Local pore samples and their local coordinates

Name	Local x	Local y
Pore 1	16	16
Pore 2	32	16
Pore 3	48	16
Pore 4	16	32
Pore 5	32	32
Pore 6	48	32
Pore 7	16	48
Pore 8	32	48
Pore 9	48	48

5.6.2 Computational Aspects

The collection of 1x1 data on permeability and relative permeability for the 162 core samples can be then used to reconstruct the fields for comparisons by placing them into the space where the pores were extracted while by passing the core analysis. The kriging is done in Tecplot. The fractional diagonal distance beyond which sources become statistically insignificant is 0.3. The semi-variance at each source data on a normalized scale was set to be 0. There was no drift in the overall trend. All

source points were considered in the interpolation; however the weights of their significance are automatically determined by Tecplot (Tecplot 2006). The field 1 permeability results in x- and y-directions are shown in Figure 39 and Figure 40. Permeability results in x- and y-directions for field 2 are shown in Figure 41 and Figure 42. These results will be discussed in later section.

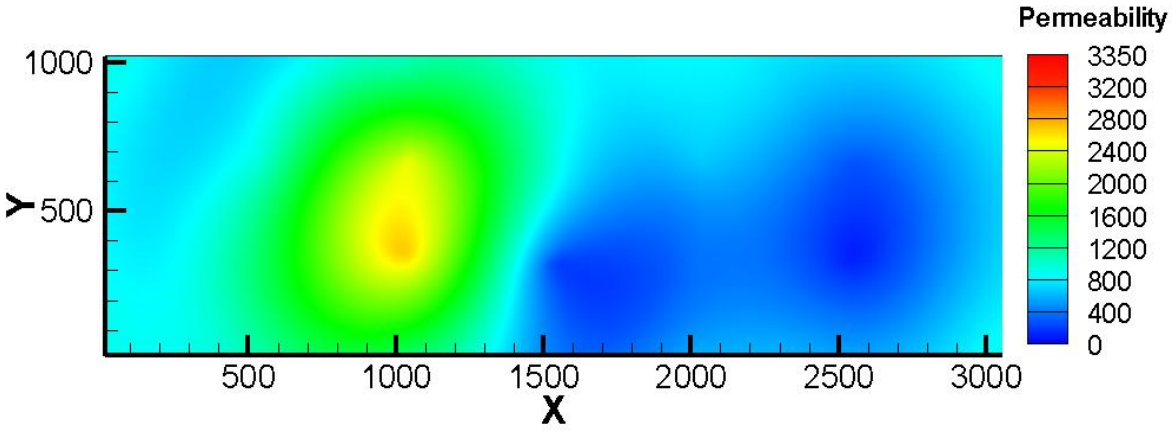

Figure 39 – Permeability field in the x-direction of field 1 using pore kriging

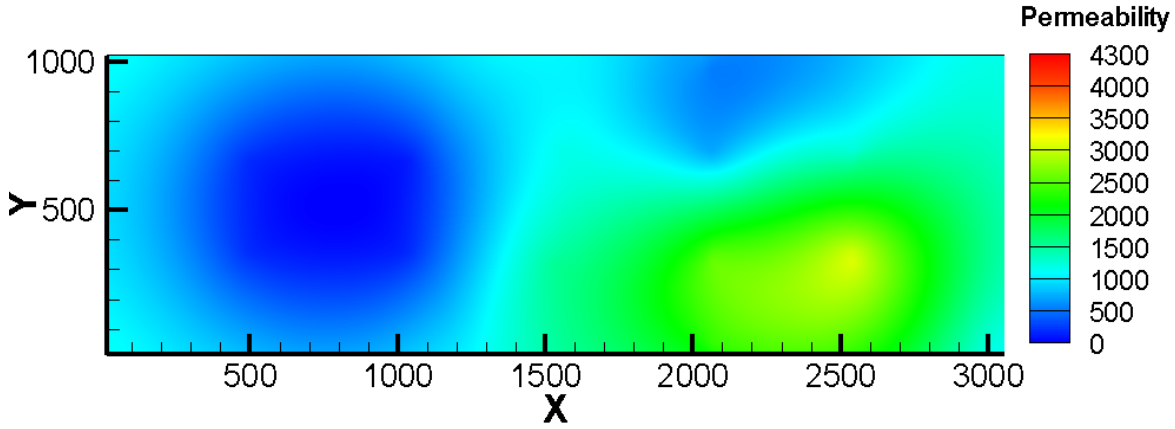

Figure 40 – Permeability field in the y-direction of field 1 using pore kriging

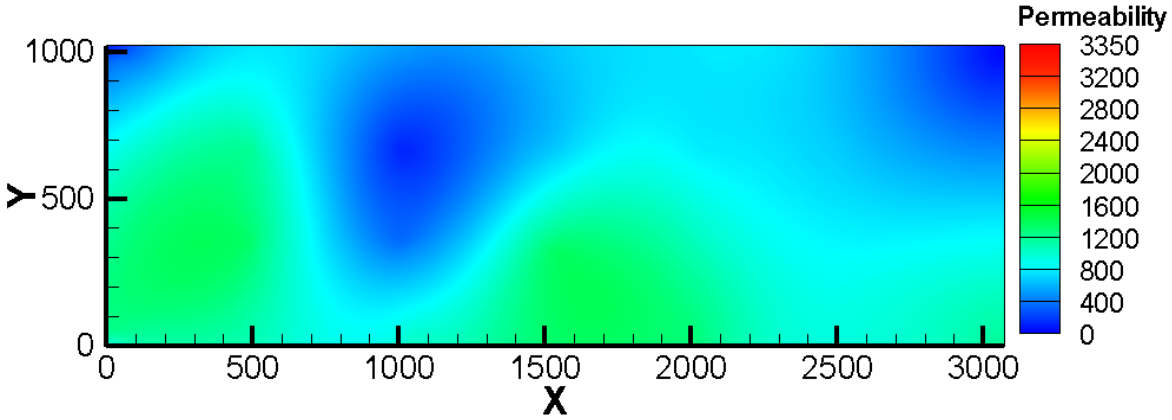

Figure 41 – Permeability field in the x-direction of field 2 using pore kriging

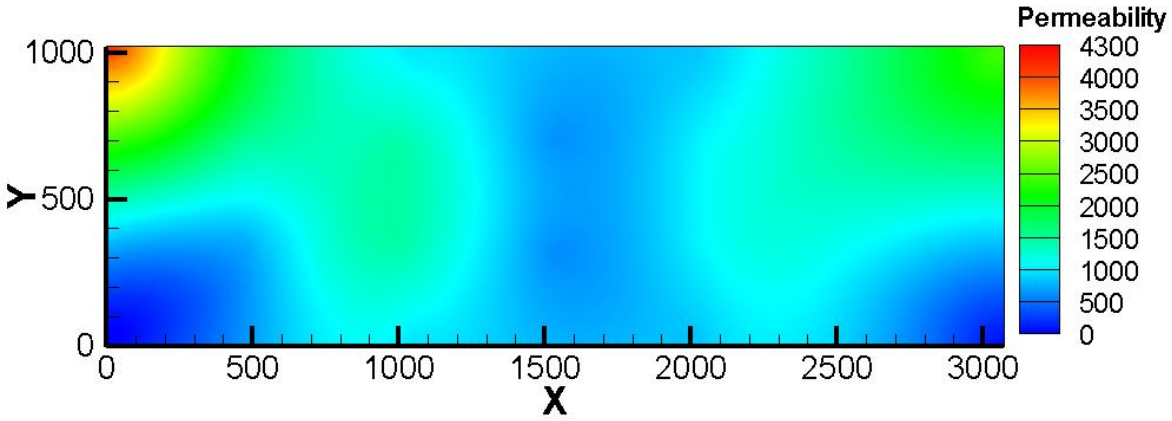

Figure 42 – Permeability field in the y-direction of field 2 using pore kriging

Chapter 6
Discussion

6.1 Visual Comparisons

6.1.1 Field 1

The locations of the points in which were used for creating the benchmark fields are marked by triangles, and the locations in which the samples were extracted are marked by circle markers, shown in Figure 43. The most important features in the x-direction of field are the red oval and the contrast between green and blue.

The benchmark, core, and pore kriged results for permeability in the x-direction are shown in Figure 44a to Figure 44c, under the same colour gradient scale as the benchmark field for fair comparisons. It is seen that the kriged field that used the pore results generate better results at the red oval gradient than the core results; however, both methods do not accurately capture the shape of the oval. This is due to the locations of the core samples extracted and the distance in which the oval shape lie away from. In this case, both kriging methods did adequately in predicting the rapid blue gradient change.

Figure 45a shows the permeability in the y-direction for field 1, with most imporant features being the two oval shaped gradients and sudden changes to blue. Figure 45b and Figure 45c show the core and pore kriging results, respectively. Both methods do an adequate job in predicting the sudden changes to blue; however, it has always been a challenge to predict small anomolies sufficiently far away relative to the spacing of the samples. The pore and core kriging results do not capture the oval shapes very well; however, the pore scale kriging results showed slightly better results than the core scale results.

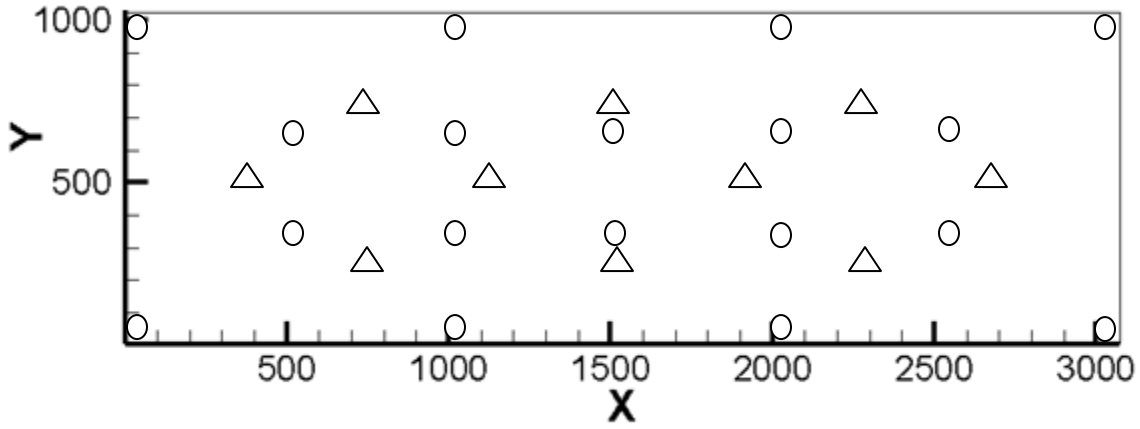

Figure 43 – Overlapping of LBM pore locations used to create the benchmark and locations of extracted cores in field 1. Triangles mark the location of the LBM pores, and the circles represent the core sample locations

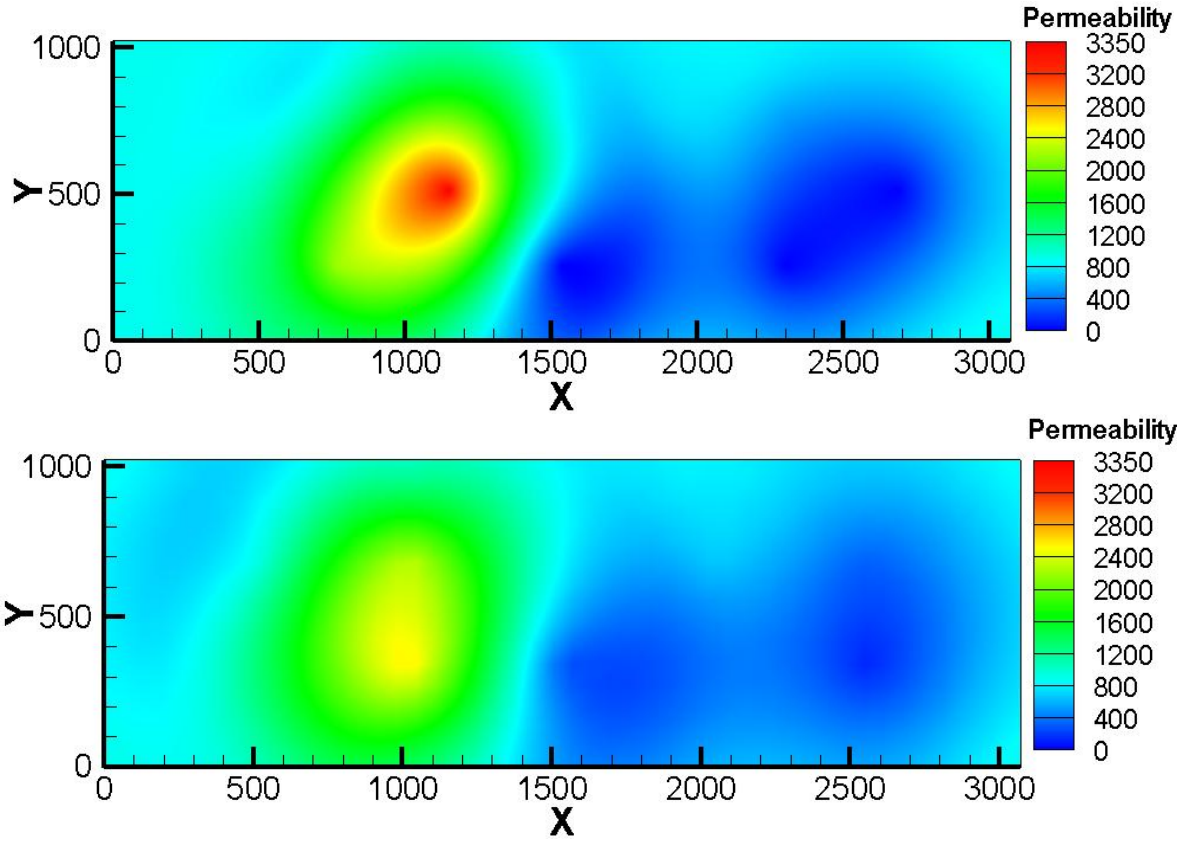

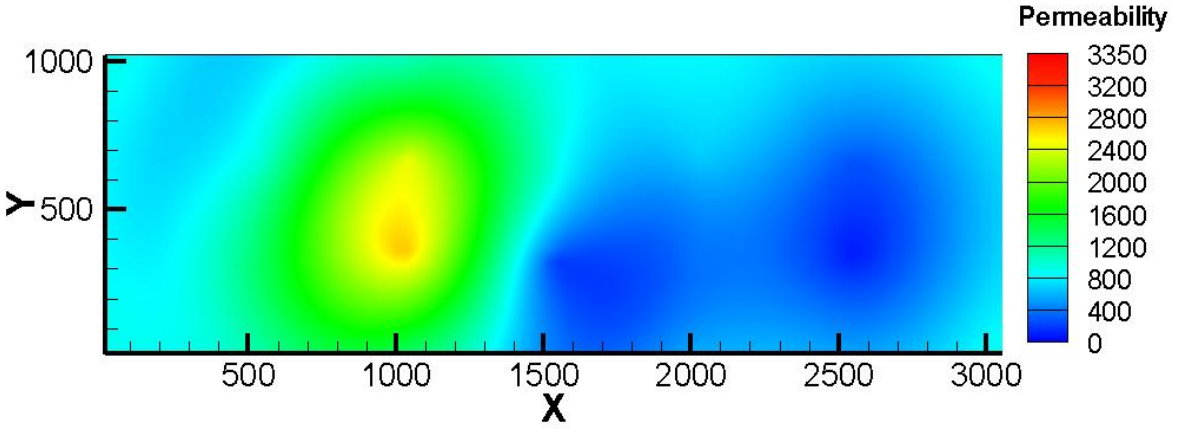

Figure 44 – Comparison of permeability field in x-direction for field 1; a) benchmark b) core kriging c) pore kriging

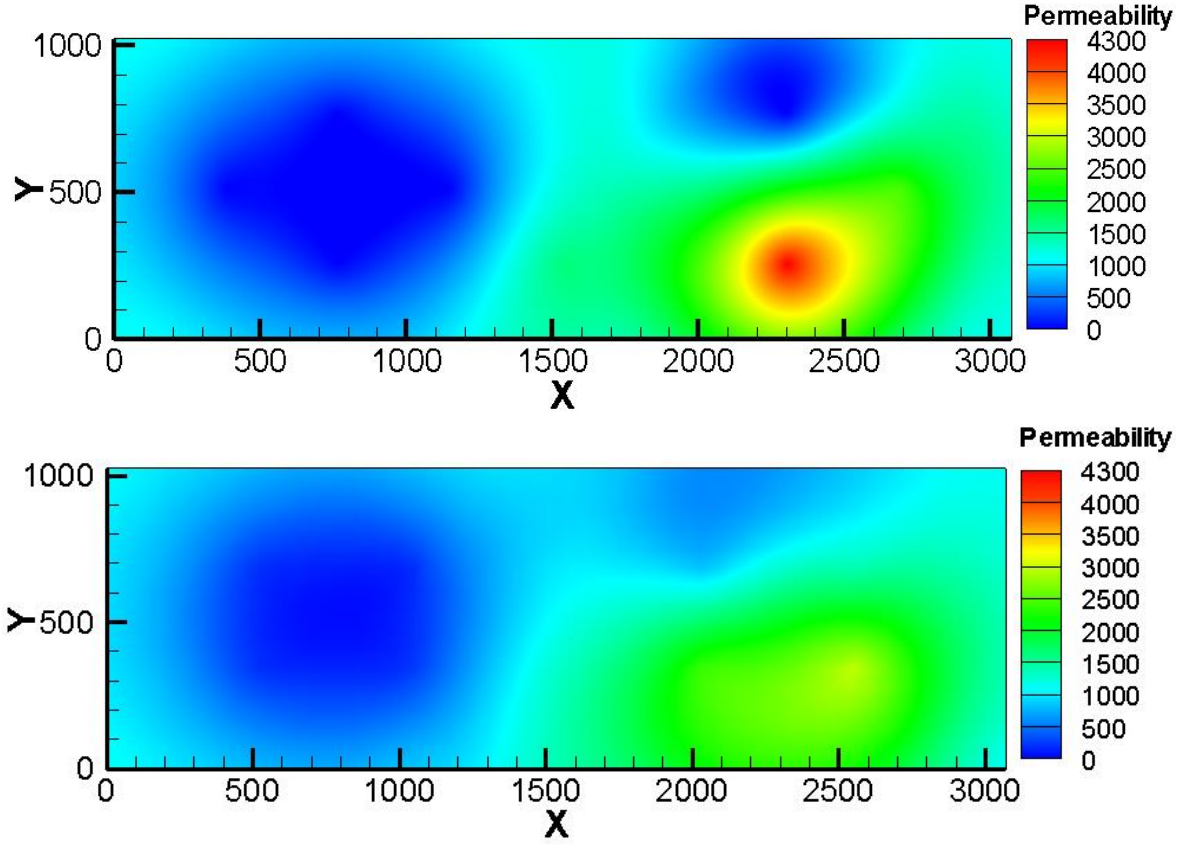

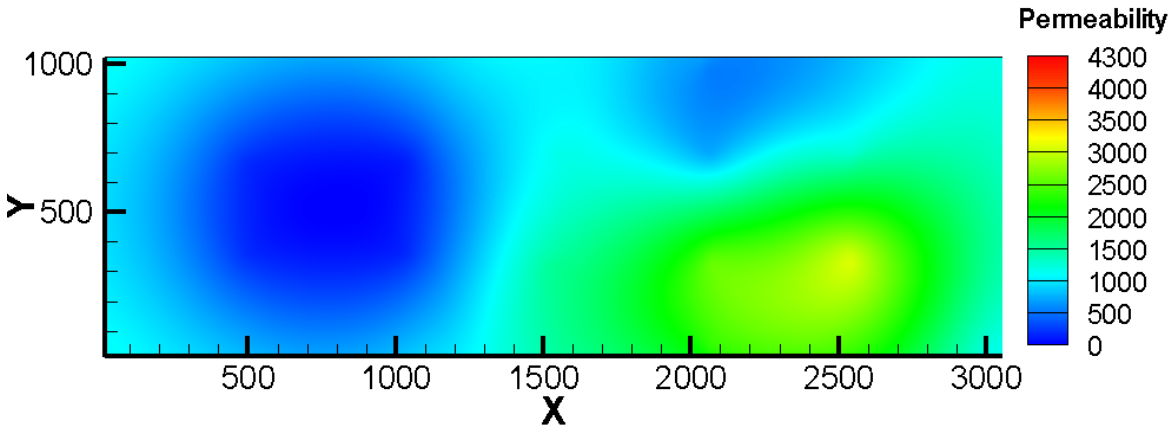

Figure 45 – Comparison of permeability field in y-direction for field 1; a) benchmark b) core kriging c) pore kriging

6.1.2 Field 2

Figure 47a presents the benchmark permeability field that was created in x-direction. The locations of the points in which the pore locations were used for creating the benchmark fields are marked by triangles, and the locations in which the core samples were extracted are marked by circle markers, shown in Figure 46. The most important features in the x-direction of field are the red oval on the centre left and the blue gradients. The core and pore kriged results are shown in Figure 47b and Figure 47c, respectively, under the same colour gradient scale as the benchmark field for fair comparisons. For the oval shaped gradient, it is relatively far away from the core and pore samples, roughly midway between two samples. It is seen that the kriged field that used the pore results generate comparable results with the core results. This result is hardly surprising as it showed that when the core samples are extracted significantly away from the key characteristics, there is little difference between the core and the proposed pore results.

Figure 48a illustrates the permeability in the y-direction, with most imporant features being the quarter oval shaped gradient at the top left and the curvy shapes of the green and blue gradients. Figure 48b and Figure 48c show the core and pore kriging results, respectively. Both methods do a fair job in predicting the general contours, and underestimating the blue gradients. The pore results show slightly better results in predicting the quarter oval than the core results. This is because the

pore method covered a wider range of the oval locations rather than one unified value in the case of core method.

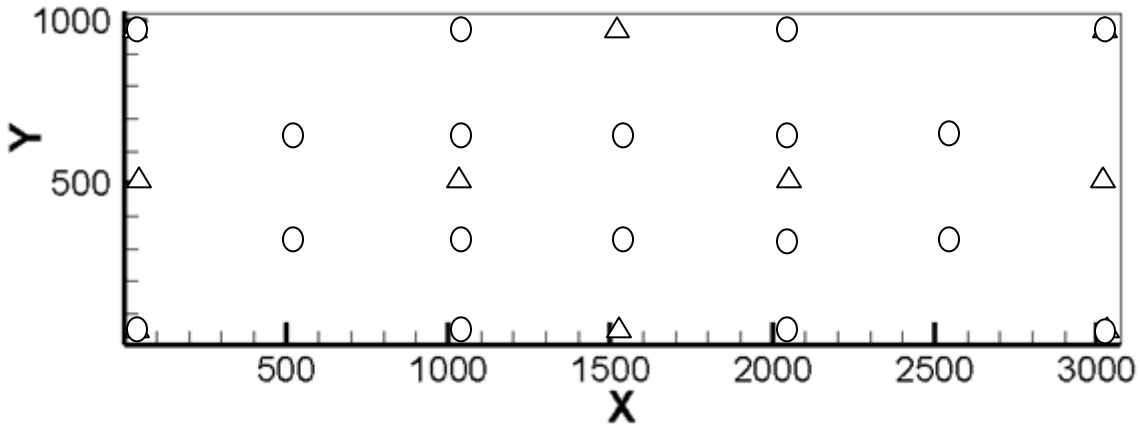

Figure 46 – Overlapping of LBM pore locations used to create the benchmark and locations of extracted cores in field 2. Triangles mark the location of the LBM pores, and the circles represent the core sample locations

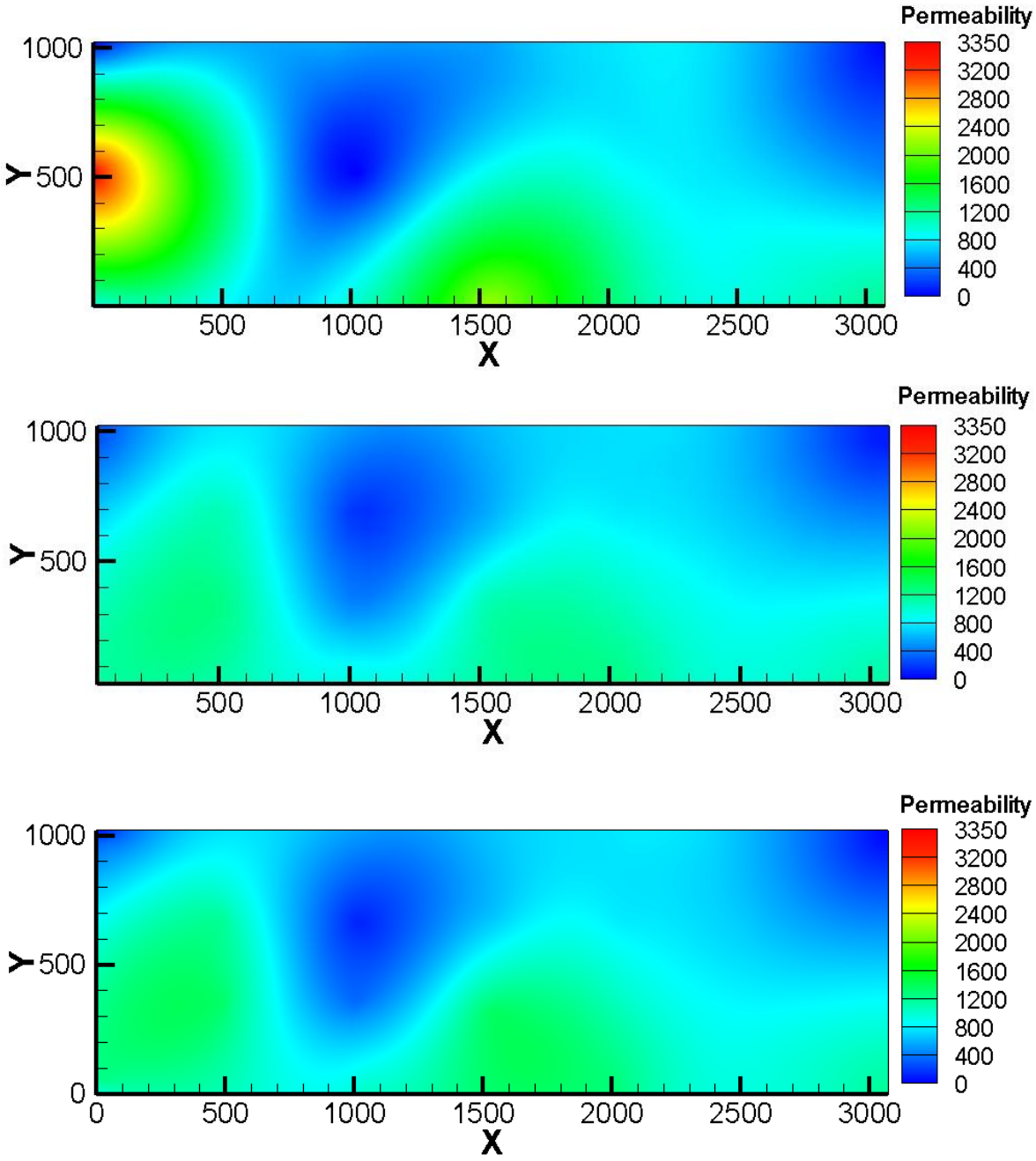

Figure 47 – Comparison of permeability field in x-direction for field 2; a) benchmark b) core kriging c) pore kriging

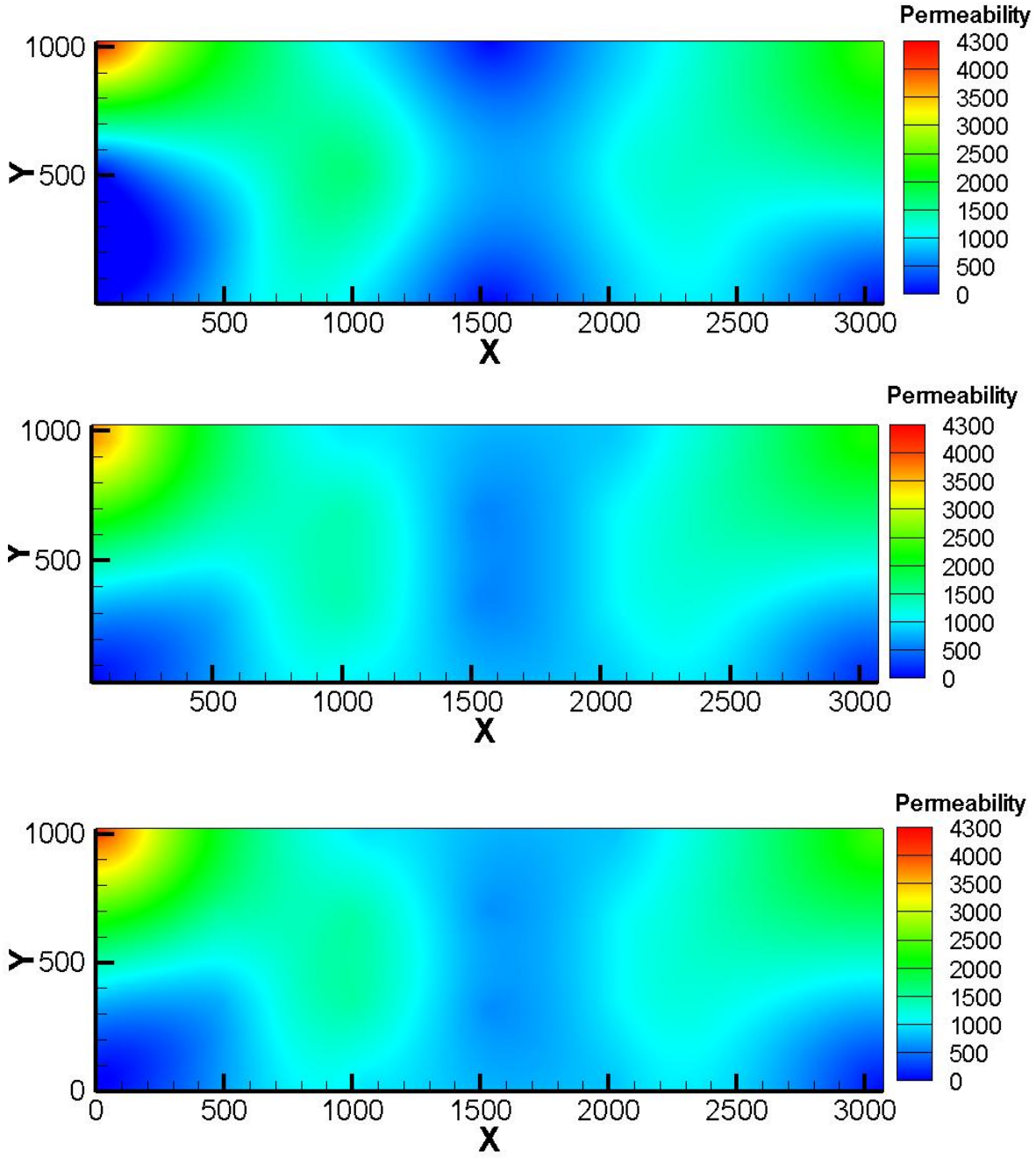

Figure 48 – Comparison of permeability field in y-direction for field 2; a) benchmark b) core kriging c) pore kriging

Table 8 shows the differences between the core results and the pore results. Percent permeability deviation of pore results showed 4-8% improvement in accuracy compared to the core results.

Relative permeability curves also showed 55-82% improvement in accuracy. By increasing the reach (higher ratio of distance between pores and maximum distance between features and sample core) with the utilizing of pores along the perimeters of the cores shows slight improvements in permeability and relative permeability as expected since it increased the coverage of the data. Further additional number of points within the pore coverage generally showed slight increases in both permeability and relative permeability data for both fields. In general, the more points to capture the characteristic of the cores, the more representative set of data is available and hence improve accuracy. If computation resources are limited, it would be more prudent to obtain a wider reach to increase the covereage of the data rather than obtain more points within the same reach. While there may be an abundance of pore scale information, an increase in information comes at a cost of computational time. The resolution for these field krigings is relatively large (core scale) with small domains, hence computational time for these operations are relatively quick. It is important for the user to understand and determine the right number of pore data to be used to balance between accuracy and computational costs.

Table 8 – Summary of the differences between core results and pore results in permeability and relative permeability

Field	Direction	Type	% Permeability deviation from benchmark	% Relative permeability Curve deviation from benchmark	Maximum distance between anomaly and nearest sample core (m)	Ratio of distance between pores/ maximum distance between feature and sample core
1	x	Core	29.90%	87.89%	0.171m	N/A
1	x	Pore	24.51%	28.65%	0.171m	0.09357
1	y	Core	42.78%	126.6%	0.268m	N/A
1	y	Pore	34.53%	44.00%	0.268m	0.05970
2	x	Core	20.44%	70.79%	0.512m	N/A
2	x	Pore	15.84%	15.25%	0.512m	0.03125
2	y	Core	42.56%	111.77%	0.512m	N/A
2	y	Pore	36.51%	33.60%	0.512m	0.03125

Chapter 7
Conclusions and Directions for future Work

7.1 Conclusions Achievements

In this work, pore samples were used to generate permeability and unsteady drainage relative permeability data of supercritical CO_2 displacing H_2O in multiple directions, relevant to CCS. To the best of the knowledge of the author, this approach had not been attempted in a binary fluid LBM model. The porosity values of the generated geometries are set as a constant of 0.2 to study the differences in permeability. Permeability values for these geometries vary and are loosely related to the minimum diameter. This wide spread in porosity and permeability is not surprising and is consistent with the studies in the literature.

Furthermore, a novel method to increase accuracy in predicting changes in localized fields by making use of pore scale data was introduced. Benchmark fields were generated using LBM results using kriging. Core extractions were done on these fields to mimic field core extractions. It is found that cores can be more representatively described by using multiple pore geometries at the lower threshold of REV dimension taken from each core. Utilizing pore geometries within the REV dimension range also meant that the properties found with the pores are representative of the medium and available for use without upscaling. Using these pore data for field kriging can generate more accurate and representative in terms of permeability and relative permeability than just using core data. This method is of course limited by the sample size and the distance between samples; however, it makes an incremental improvement to field prediction and attempts to make use of the small microstructure data which the geological features are founded upon.

7.2 Future Work

Future works include incorporation of lab experiments to test out the method in practice, such as the sandbox experiment conducted by Illman et al. (Illman et al. 2010), and reaching out to analyze real core samples and make use of real pore geometries. In addition, incorporation of indirect method with the propose methodology should be investigated for further possible improvements.

In addition, more advanced LBM models incorporating different density differences can be used, and gravity segregation effects can be incorporated. 3D studies should also be conducted when possible.

Appendix A– Pore Geometries

Geometry 1

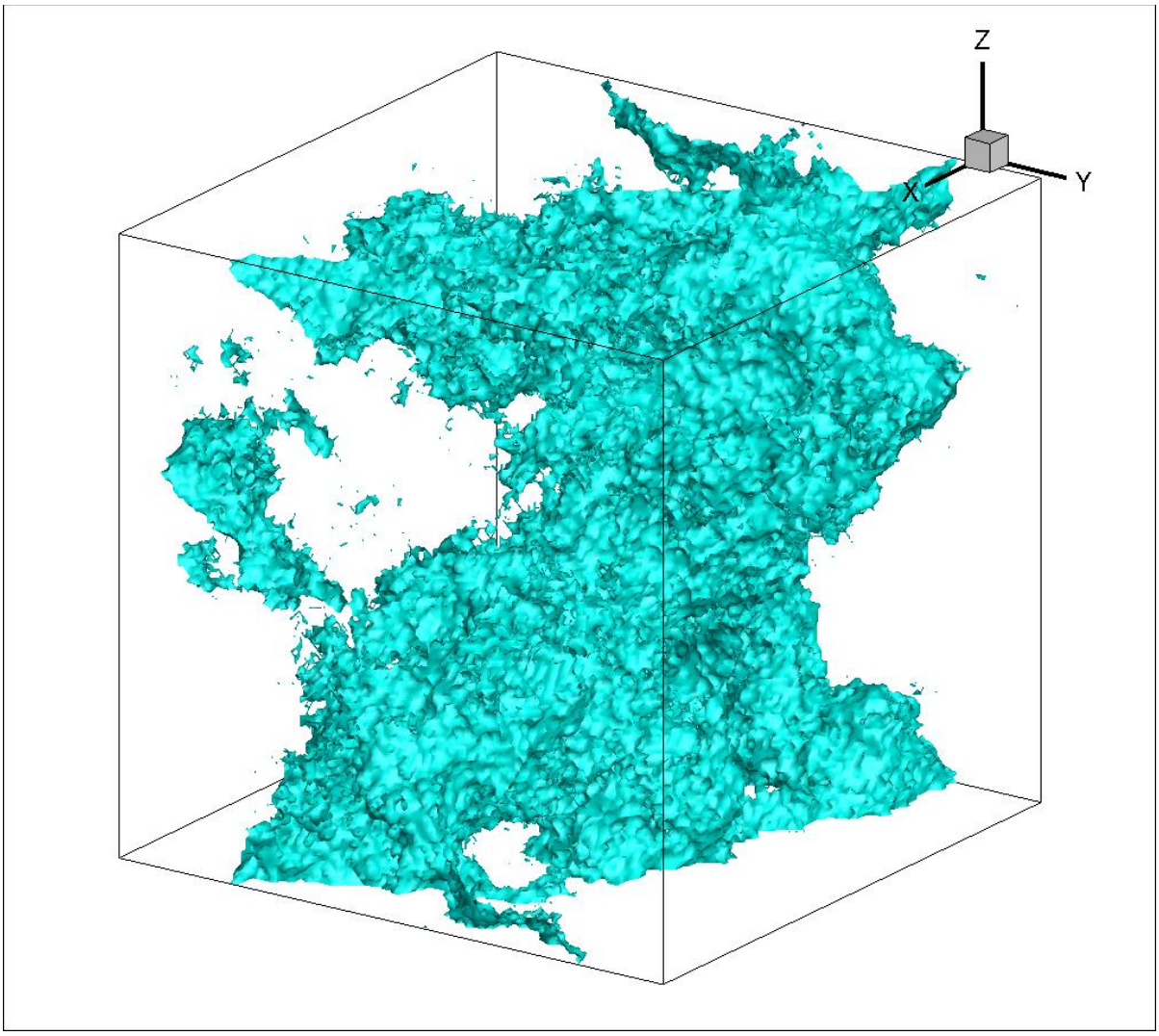

Geometry 2

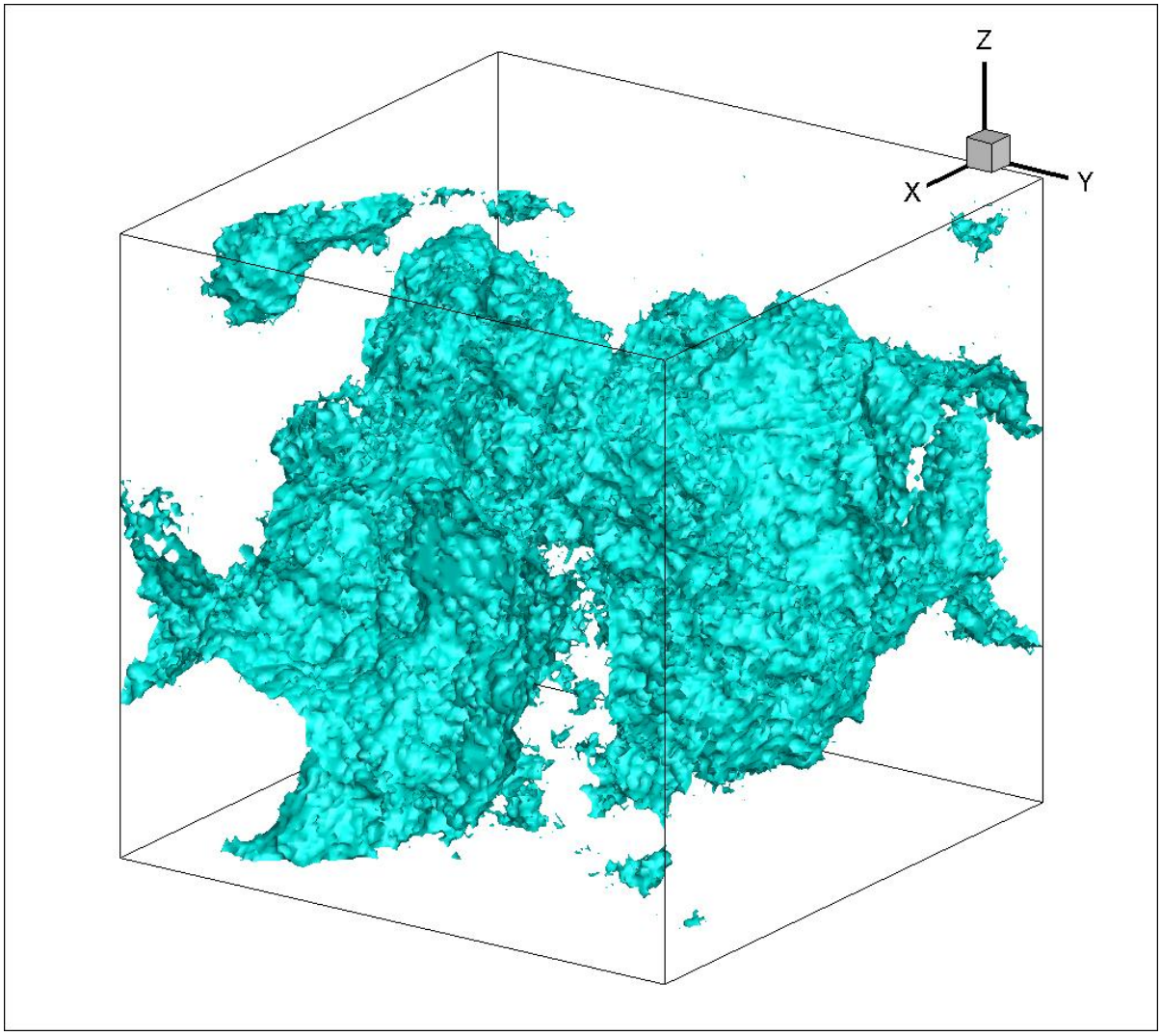

Geometry 3

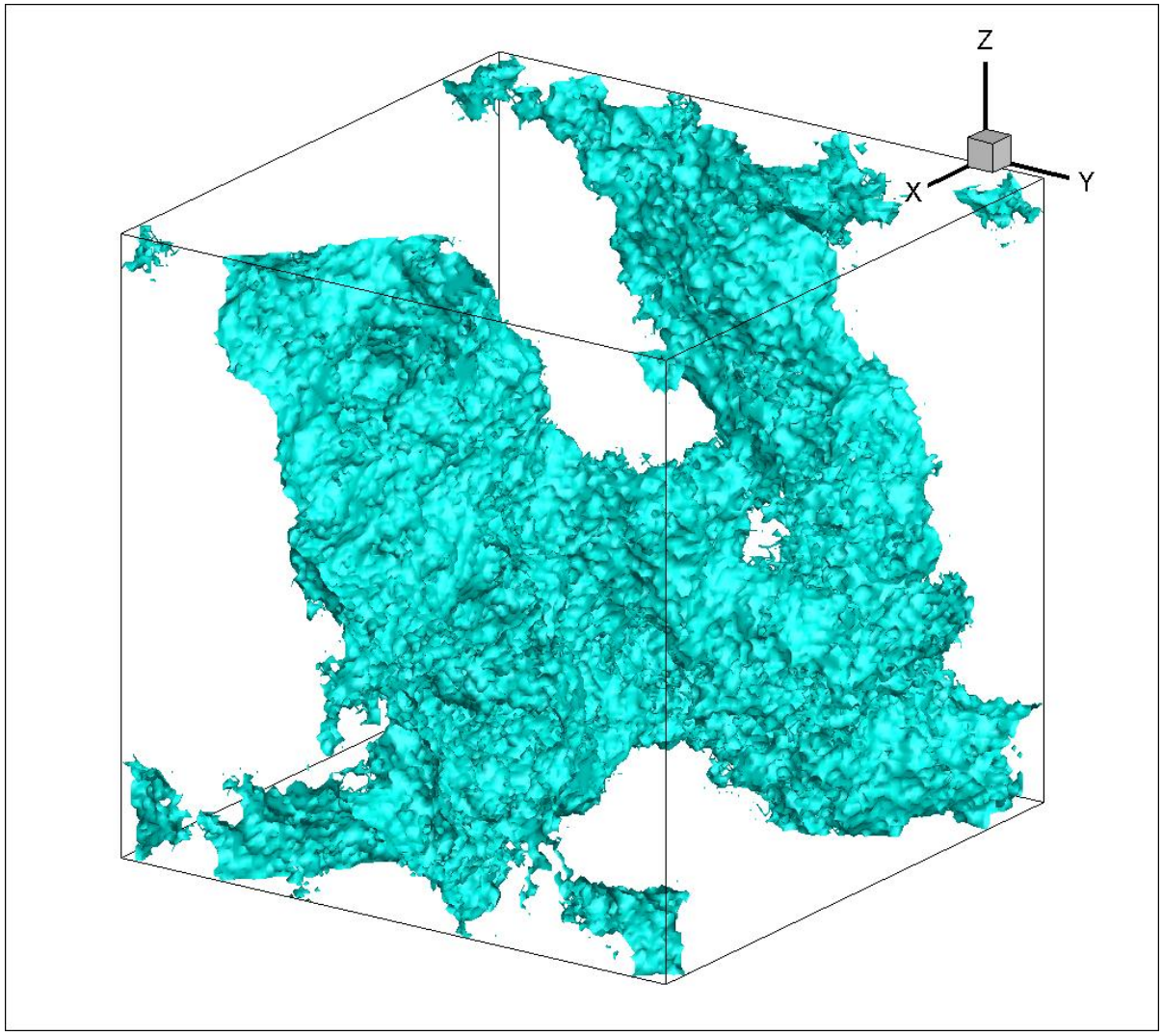

Geometry 4

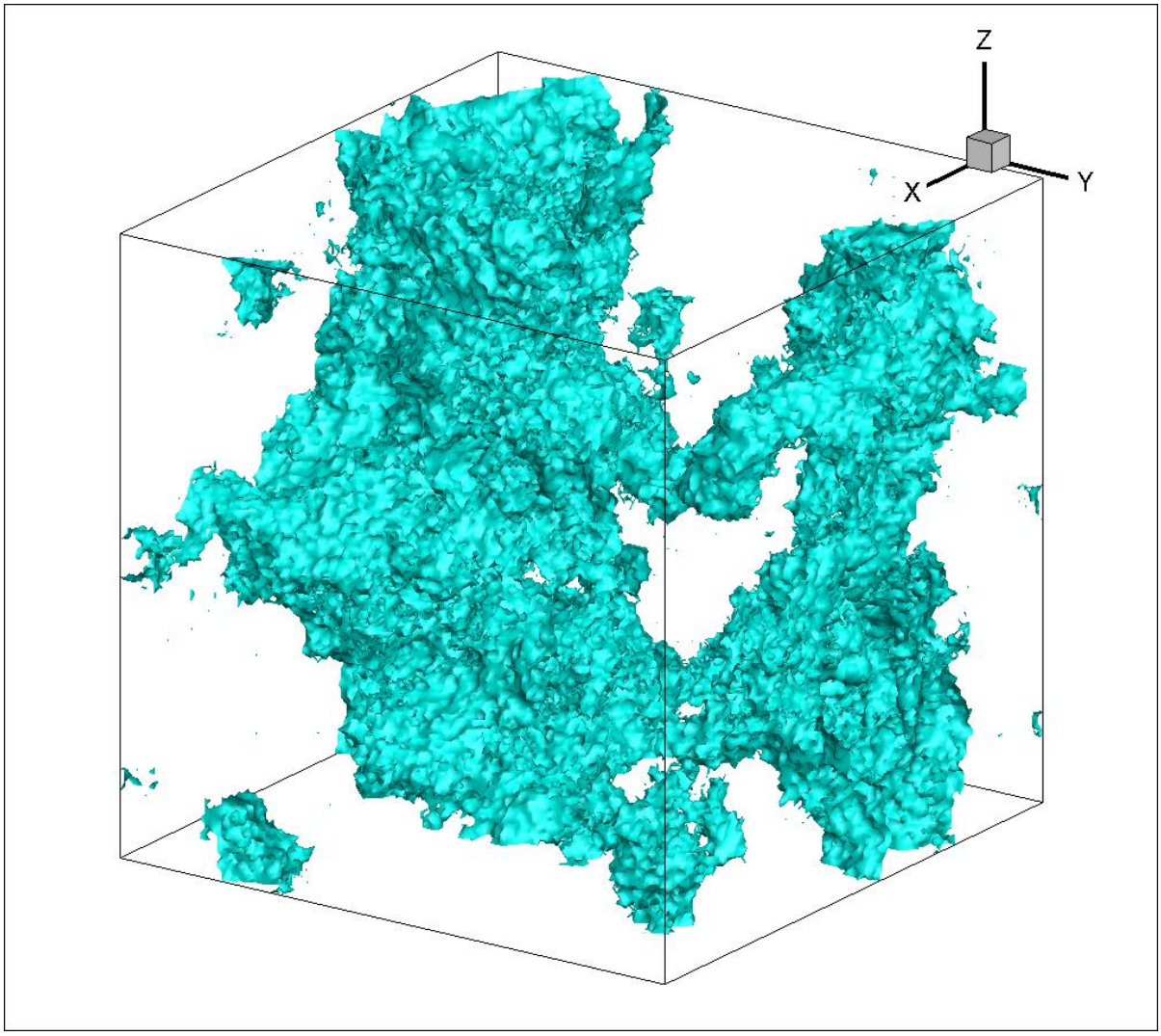

Geometry 5

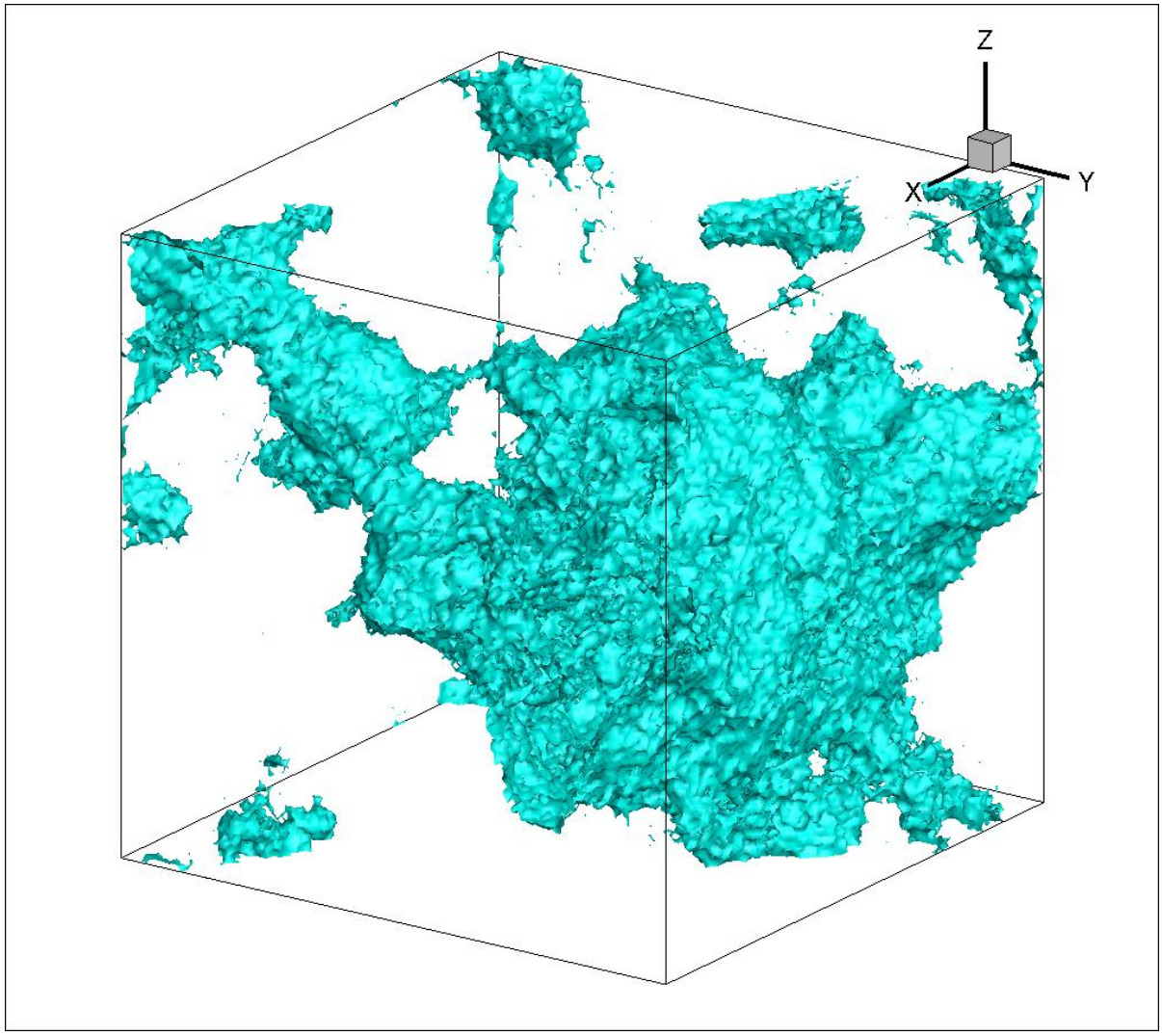

Geometry 6

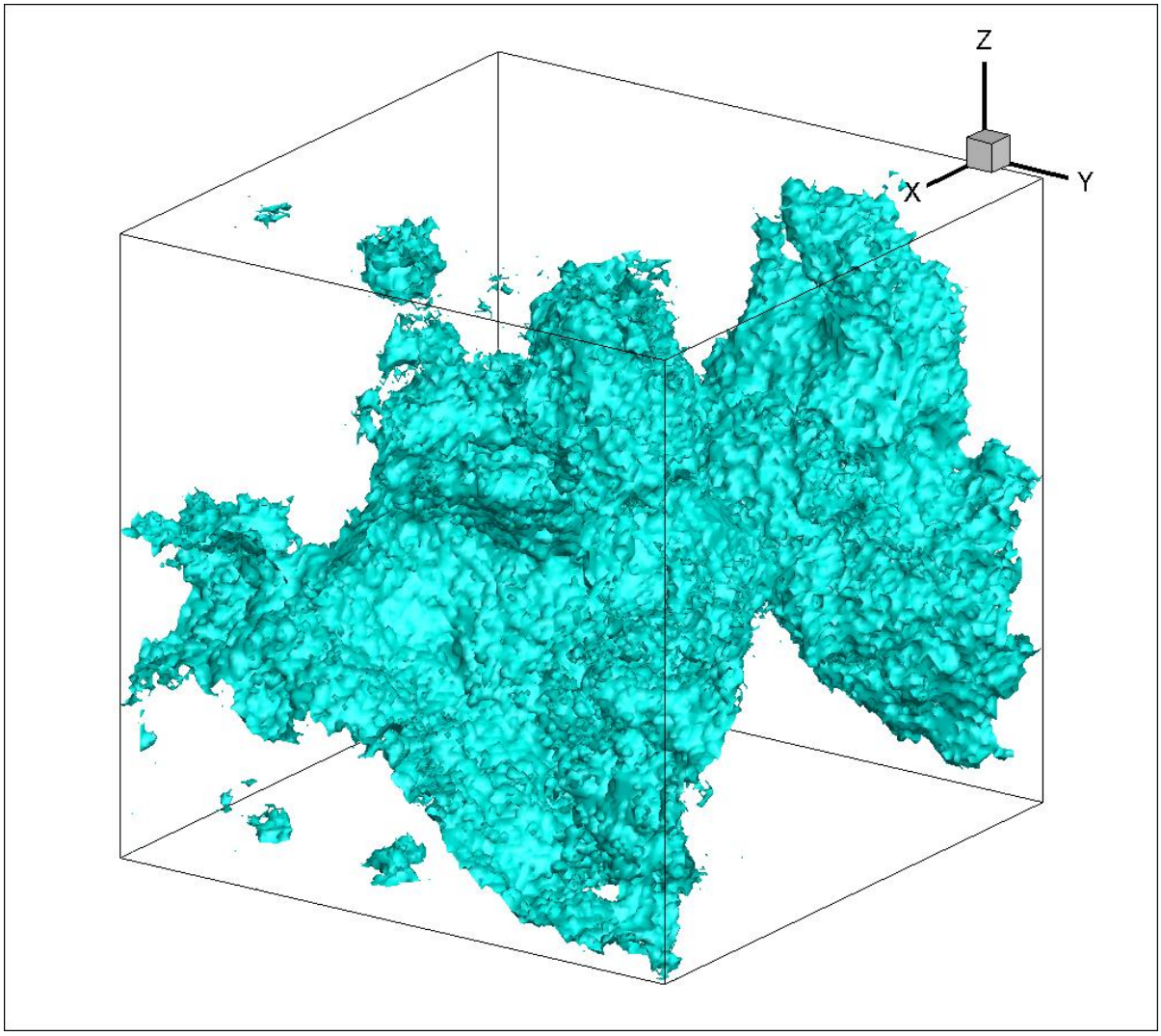

Geometry 7

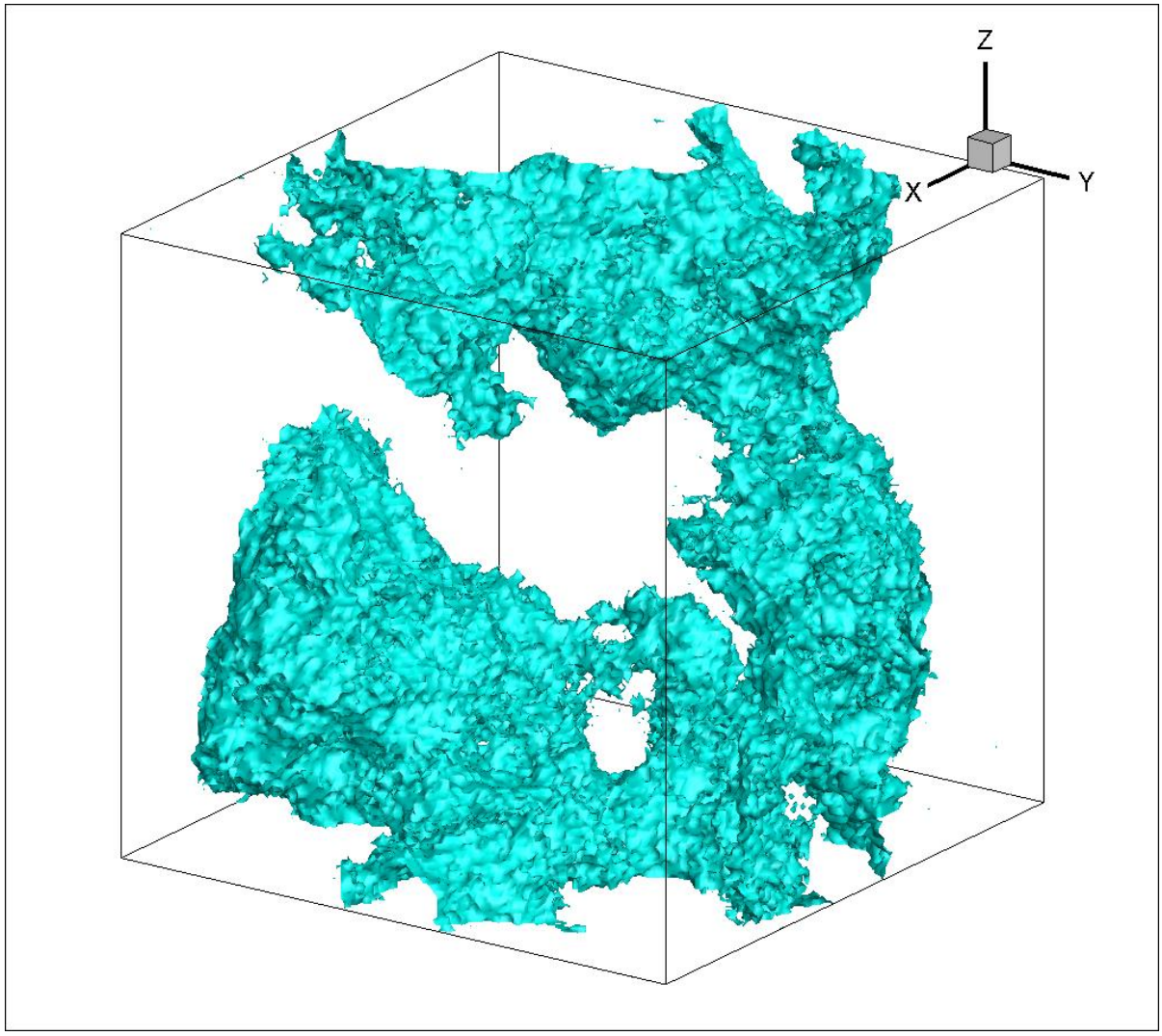

Geometry 8

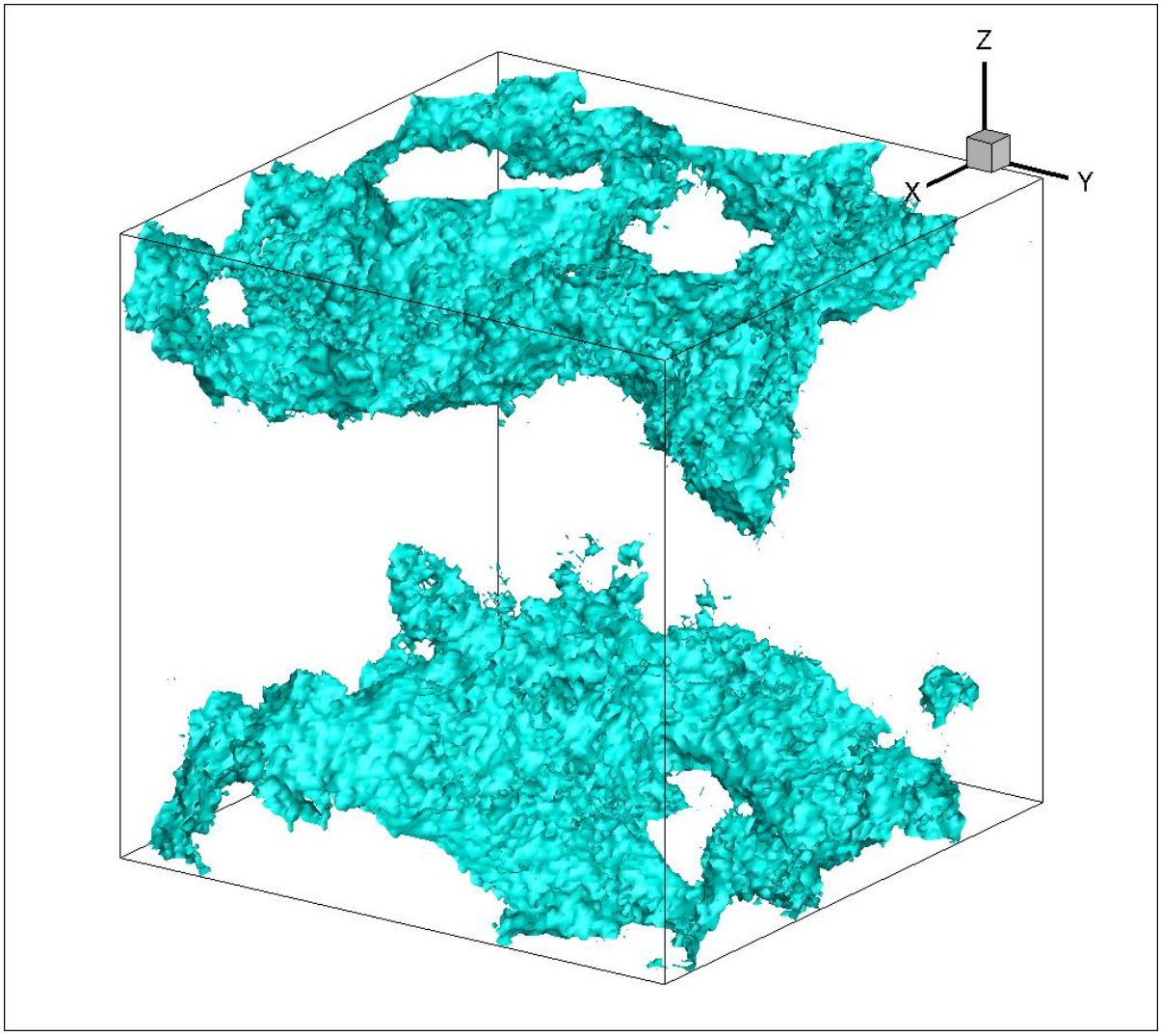

Geometry 9

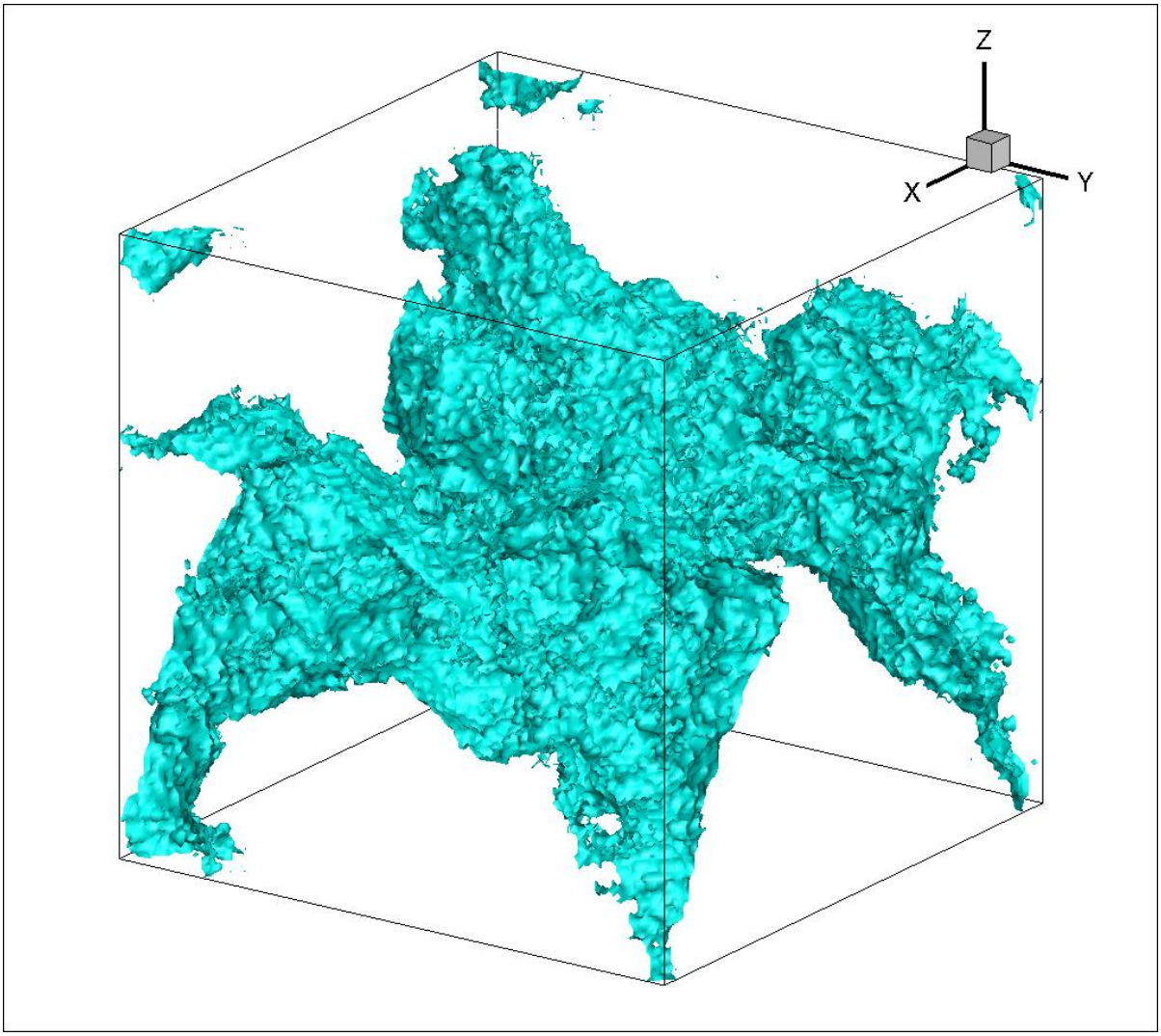

Geometry 10

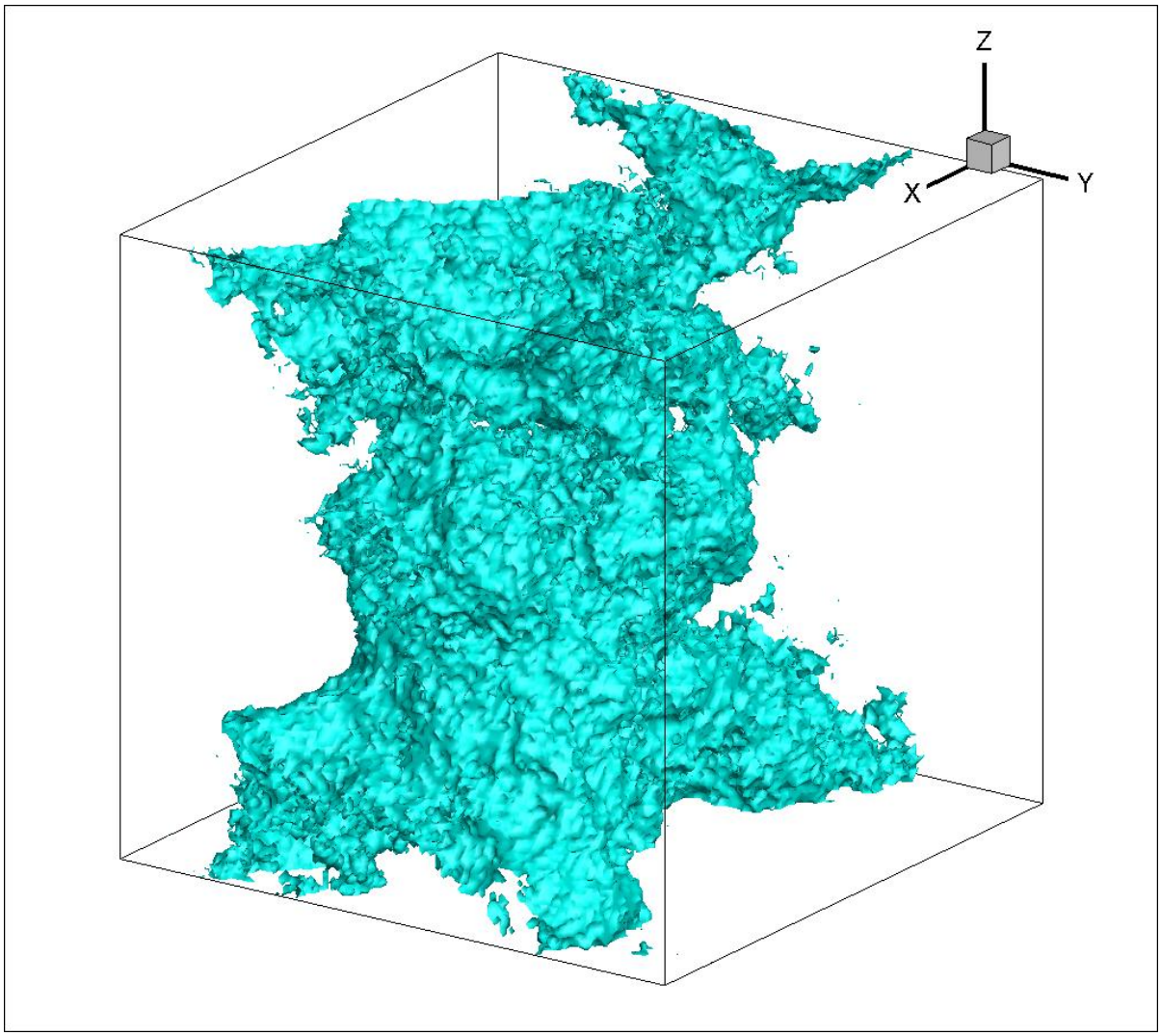

Appendix B– Locations of Pores

– Locations of Pores in Core Samples	local x	local y	"x"	"y"
Core 1 - 1	16	16	496	325
Core 1 - 2	32	16	512	325
Core 1 - 3	48	16	528	325
Core 1 - 4	16	32	496	341
Core 1 - 5	32	32	512	341
Core 1 - 6	48	32	528	341
Core 1 - 7	16	48	496	357
Core 1 - 8	32	48	512	357
Core 1 - 9	48	48	528	357
Core 2 - 1	16	16	496	667
Core 2 - 2	32	16	512	667
Core 2 - 3	48	16	528	667
Core 2 - 4	16	32	496	683
Core 2 - 5	32	32	512	683
Core 2 - 6	48	32	528	683
Core 2 - 7	16	48	496	699
Core 2 - 8	32	48	512	699
Core 2 - 9	48	48	528	699
Core 3 - 1	16	16	1008	325
Core 3 - 2	32	16	1024	325
Core 3 - 3	48	16	1040	325
Core 3 - 4	16	32	1008	341
Core 3 - 5	32	32	1024	341
Core 3 - 6	48	32	1040	341
Core 3 - 7	16	48	1008	357
Core 3 - 8	32	48	1024	357
Core 3 - 9	48	48	1040	357
Core 4 - 1	16	16	1008	667
Core 4 - 2	32	16	1024	667
Core 4 - 3	48	16	1040	667
Core 4 - 4	16	32	1008	683
Core 4 - 5	32	32	1024	683
Core 4 - 6	48	32	1040	683

Core 4 - 7	16	48	1008	699
Core 4 - 8	32	48	1024	699
Core 4 - 9	48	48	1040	699
Core 5 - 1	16	16	1520	325
Core 5 - 2	32	16	1536	325
Core 5 - 3	48	16	1552	325
Core 5 - 4	16	32	1520	341
Core 5 - 5	32	32	1536	341
Core 5 - 6	48	32	1552	341
Core 5 - 7	16	48	1520	357
Core 5 - 8	32	48	1536	357
Core 5 - 9	48	48	1552	357
Core 6 - 1	16	16	1520	667
Core 6 - 2	32	16	1536	667
Core 6 - 3	48	16	1552	667
Core 6 - 4	16	32	1520	683
Core 6 - 5	32	32	1536	683
Core 6 - 6	48	32	1552	683
Core 6 - 7	16	48	1520	699
Core 6 - 8	32	48	1536	699
Core 6 - 9	48	48	1552	699
Core 7 - 1	16	16	2032	325
Core 7 - 2	32	16	2048	325
Core 7 - 3	48	16	2064	325
Core 7 - 4	16	32	2032	341
Core 7 - 5	32	32	2048	341
Core 7 - 6	48	32	2064	341
Core 7 - 7	16	48	2032	357
Core 7 - 8	32	48	2048	357
Core 7 - 9	48	48	2064	357
Core 8 - 1	16	16	2032	667
Core 8 - 2	32	16	2048	667
Core 8 - 3	48	16	2064	667
Core 8 - 4	16	32	2032	683
Core 8 - 5	32	32	2048	683
Core 8 - 6	48	32	2064	683
Core 8 - 7	16	48	2032	699
Core 8 - 8	32	48	2048	699
Core 8 - 9	48	48	2064	699

Core 9 - 1	16	16	2544	325
Core 9 - 2	32	16	2560	325
Core 9 - 3	48	16	2576	325
Core 9 - 4	16	32	2544	341
Core 9 - 5	32	32	2560	341
Core 9 - 6	48	32	2576	341
Core 9 - 7	16	48	2544	357
Core 9 - 8	32	48	2560	357
Core 9 - 9	48	48	2576	357
Core 10 -1	16	16	2544	667
Core 10 -2	32	16	2560	667
Core 10 -3	48	16	2576	667
Core 10 -4	16	32	2544	683
Core 10 -5	32	32	2560	683
Core 10 -6	48	32	2576	683
Core 10 -7	16	48	2544	699
Core 10 -8	32	48	2560	699
Core 10 -9	48	48	2576	699
Core 11 -1	16	16	16	16
Core 11 -2	32	16	32	16
Core 11 -3	48	16	48	16
Core 11 -4	16	32	16	32
Core 11 -5	32	32	32	32
Core 11 -6	48	32	48	32
Core 11 -7	16	48	16	48
Core 11 -8	32	48	32	48
Core 11 -9	48	48	48	48
Core 12 -1	16	16	1008	16
Core 12 -2	32	16	1024	16
Core 12 -3	48	16	1040	16
Core 12 -4	16	32	1008	32
Core 12 -5	32	32	1024	32
Core 12 -6	48	32	1040	32
Core 12 -7	16	48	1008	48
Core 12 -8	32	48	1024	48
Core 12 -9	48	48	1040	48
Core 13 -1	16	16	2032	16
Core 13 -2	32	16	2048	16
Core 13 -3	48	16	2064	16

Core 13 -4	16	32	2032	32
Core 13 -5	32	32	2048	32
Core 13 -6	48	32	2064	32
Core 13 -7	16	48	2032	48
Core 13 -8	32	48	2048	48
Core 13 -9	48	48	2064	48
Core 14 -1	16	16	3024	16
Core 14 -2	32	16	3040	16
Core 14 -3	48	16	3056	16
Core 14 -4	16	32	3024	32
Core 14 -5	32	32	3040	32
Core 14 -6	48	32	3056	32
Core 14 -7	16	48	3024	48
Core 14 -8	32	48	3040	48
Core 14 -9	48	48	3056	48
Core 15 -1	16	16	16	976
Core 15 -2	32	16	32	976
Core 15 -3	48	16	48	976
Core 15 -4	16	32	16	992
Core 15 -5	32	32	32	992
Core 15 -6	48	32	48	992
Core 15 -7	16	48	16	1008
Core 15 -8	32	48	32	1008
Core 15 -9	48	48	48	1008
Core 16 -1	16	16	1008	976
Core 16 -2	32	16	1024	976
Core 16 -3	48	16	1040	976
Core 16 -4	16	32	1008	992
Core 16 -5	32	32	1024	992
Core 16 -6	48	32	1040	992
Core 16 -7	16	48	1008	1008
Core 16 -8	32	48	1024	1008
Core 16 -9	48	48	1040	1008
Core 17 -1	16	16	2032	976
Core 17 -2	32	16	2048	976
Core 17 -3	48	16	2064	976
Core 17 -4	16	32	2032	992
Core 17 -5	32	32	2048	992
Core 17 -6	48	32	2064	992

Core 17 -7	16	48	2032	1008
Core 17 -8	32	48	2048	1008
Core 17 -9	48	48	2064	1008
Core 18 -1	16	16	3024	976
Core 18 -2	32	16	3040	976
Core 18 -3	48	16	3056	976
Core 18 -4	16	32	3024	992
Core 18 -5	32	32	3040	992
Core 18 -6	48	32	3056	992
Core 18 -7	16	48	3024	1008
Core 18 -8	32	48	3040	1008
Core 18 -9	48	48	3056	1008

Bibliography

Abaci, S., J. S. Edwards and B. N. Whittaker (1992). "Relative permeability measurements for two phase flow in unconsolidated sands." Mine Water and the Environment **11**(2): 11-26.

Babadagli, T. and S. Al-Salmi (2004). "A Review of Permeability-Prediction Methods for Carbonate Reservoirs Using Well-Log Data." SPE Reservoir Evaluation & Engineering **7**(2): 75-88.

Balan, B., S. Mohaghegh and S. Ameri (1995). State-Of-The-Art in Permeability Determination From Well Log Data: Part 1- A Comparative Study, Model Development. SPE Eastern Regional Conference Morgantown, West Virginia, Society of Petroleum Engineers.

Bennion, B. (2005). Relative Permeability Characteristics for Supercritical CO2 Displacing Water in a Variety of Potential Sequestration Zones. SPE Annual Technical Conference and Exhibition, 9-12 October 2005. Dallas, Texas, Society of Petroleum Engineers.

Bennion, B. and S. Bachu (2006). The Impact of Interfacial Tension and Pore Size Distribution/Capillary Pressure Character on CO2 Relative Permeability at Reservoir Conditions in CO2-Brine Systems. SPE/DOE Symposium on Improved Oil Recovery, 22-26 April 2006. Tulsa, Oklahoma, USA, Society of Petroleum Engineers.

Carbone, A., B. M. Chiaia, B. Frigo and C. Türk (2010). "Snow metamorphism: A fractal approach." Physical Review E **82**(3): 5.

Chiquet, P., J.-L. Daridon, D. Broseta and S. Thibeau (2007). "CO2/water interfacial tensions under pressure and temperature conditions of CO2 geological storage." Energy Conversion and Management **48**(3): 736-744.

Christie, M. A. (2001). "Flow in porous media — scale up of multiphase flow." Current Opinion in Colloid & Interface Science **6**(3): 236-241.

Dainton, M. P., M. H. Goldwater and N. K. Nichols (1997). "Direct Computation of Stochastic Flow in Reservoirs with Uncertain Parameters." Journal of Computational Physics **130**(2): 203-216.

Dake, L. P. (2001). The Practice of Reservoir Engineering (Revised Edition). Amsterdam.

Das, D. B. and S. M. Hassanizadeh (2005). Upscaling Multiphase Flow in Porous Media From Pore to Core and Beyond. Dordrecht, Springer.

Davis, J. C. (1986). Statistics and Data Analysis in Geology, Second Edition. New York, John Wiley & Sons.

Dullien, F. A. L. (1979). Porous media: fluid transport and pore structure. New York, Academic Press.

Egermann, P., C. Chalbaud, J.-P. Duquerroix and Y. Le Gallo (2006). An Integrated Approach to Parameterize Reservoir Models for CO2 Injection in Aquifers. SPE Annual Technical Conference and Exhibition, 24-27 September 2006. San Antonio, Texas, USA, Society of Petroleum Engineers.

Farmer, C. L. (2002). "Upscaling: a review." International Journal for Numerical Methods in Fluids **40**(1-2): 63-78.

Fenghour, A., W. A. Wakeham and V. Vesovic (1998). "The Viscosity of Carbon Dioxide." Journal of Physical Chemical Reference Data **27**(1): 31-44.

Gothäll, R., M. Eriksson and H. tille (2005). A Modification of the Random Midpoint Displacement Method for Generating Rock Fracture Similar Surfaces. ICF XI - 11th International Conference on Fracture. Turin, Italy.

Green, C. and L. Paterson (2007). "Analytical three-dimensional renormalization for calculating effective permeabilities." Transport in Porous Media **68**(2): 237-248.

Gunstensen, A. K. (1992). Lattice-Boltzmann Studies of Multiphase Flow Through Porous Media. Department of Earth, Atmospheric, and Planetary Sciences. Cambridge, MASSACHUSETTS INSTITUTE OF TECHNOLOGY. **PhD:** 127.

Gunstensen, A. K. and D. H. Rothman (1993). "Lattice-Boltzmann Studies of Immiscible Two-Phase Flow Through Porous Media." J. Geophys. Res. **98**(B4): 6431-6441.

Guo, Z., C. Zheng and B. Shi (2002). "Discrete lattice effects on the forcing term in the lattice Boltzmann method." Physical Review E **65**(4): 046308.

Hastings, J. and A. Muggeridge (2001). "Upscaling Uncertain Permeability Using Small Cell Renormalization." Mathematical Geology **33**(4): 491-505.

Huang, H., Z. Li, S. Liu and X.-y. Lu (2009). "Shan-and-Chen-type multiphase lattice Boltzmann study of viscous coupling effects for two-phase flow in porous media." International Journal for Numerical Methods in Fluids **61**(3): 341-354.

Huang, H., L. Wang and X.-y. Lu (2011). "Evaluation of three lattice Boltzmann models for multiphase flows in porous media." Comput. Math. Appl. **61**(12): 3606-3617.

Illman, W. A., J. Zhu, A. J. Craig and D. Yin (2010). "Comparison of aquifer characterization approaches through steady state groundwater model validation: A controlled laboratory sandbox study." Water Resour. Res. **46**(4): W04502.

Jilesen, J., J. Kuo and F.-S. Lien (2011). "Three-dimensional midpoint displacement algorithm for the generation of fractal porous media." Computers & Geosciences(0).

Journel, A. G. and F. G. Alabert (1990). "New Method for Reservoir Mapping." Journal of Petroleum Technology **42**(2): 212-218.

King, P. R. (1989). "The use of renormalization for calculating effective permeability." Transport in Porous Media **4**(1): 37-58.

Kuzmin, A. and J. Derksen (2011). Introduction to Lattice Boltzmann Method. LBM Workshop. Edmonton, University of Alberta.

Kuzmin, A., M. Januszewski, D. Eskin, F. Mostowfi and J. J. Derksen (2011). "Simulations of gravity-driven flow of binary liquids in microchannels." Chemical Engineering Journal **171**(2): 646-654.

Kuzmin, A., M. Januszewski, D. Eskin, F. Mostowfi and J. J. Derksen (2011). "Three-dimensional binary-liquid lattice Boltzmann simulation of microchannels with rectangular cross sections." Chemical Engineering Journal **178**(0): 306-316.

Li, H., C. Pan and C. T. Miller (2005). "Pore-scale investigation of viscous coupling effects for two-phase flow in porous media." Physical Review E **72**(2): 026705.

Lu, S., F. J. Moltz and H. H. Liu (2003). "An efficient, three-dimensional, anisotropic, fractional Brownian motion and truncated fractionalLevy motion simulation algorithm based on successive random additions." Computers & Geosciences **29**(1): 15-25.

Martys, N. S. and H. Chen (1996). "Simulation of multicomponent fluids in complex three-dimensional geometries by the lattice Boltzmann method." Physical Review E **53**(1): 743-750.

Meakin, P. and A. M. Tartakovsky (2009). "Modeling and simulation of pore-scale multiphase fluid flow and reactive transport in fractured and porous media." Rev. Geophys. **47**(3): RG3002.

Müller, N. (2011). "Supercritical CO₂-Brine Relative Permeability Experiments in Reservoir Rocks—Literature Review and Recommendations." Transport in Porous Media **87**(2): 367-383.

Ovaysi, S. and M. Piri (2010). "Direct pore-level modeling of incompressible fluid flow in porous media." Journal of Computational Physics **229**(19): 7456-7476.

Pan, C., L.-S. Luo and C. T. Miller (2006). "An evaluation of lattice Boltzmann schemes for porous medium flow simulation." Computers & Fluids **35**(8–9): 898-909.

Parker, J. C. (1989). "Multiphase flow and transport in porous media." Reviews of Geophysics **27**(3): 311-328.

Permadi, P. and A. Susilo (2009). Permeability Prediction and Characteristics of Pore Structure and Geometry as Inferred from Core Data. SPE/EAGE Reservoir Characterization and Simulation Conference, 19-21 October 2009. Abu Dhabi, UAE, Society of Petroleum Engineers.

Pooley, C. M., H. Kusumaatmaja and J. M. Yeomans (2008). "Contact line dynamics in binary lattice Boltzmann simulations." Physical Review E **78**(5): 056709.

Ramstad, T., P.-E. Øren and S. Bakke (2010). "Simulation of Two Phase Flow in Reservoir Rocks Using a Lattice Boltzmann Method." SPE Journal **15**(4): 917-927.

Renard, P. and G. de Marsily (1997). "Calculating equivalent permeability: a review." Advances in Water Resources **20**(5-6): 253-278.

Suekane, T., T. Ishii, S. Tsushima and S. Hirai (2006). "Migration of CO2 in Porous Media Filled with water." Journal of Thermal Science and Technology **1**(1): 1-11.

Suekane, T., S. Soukawa, S. Iwatani, S. Tsushima and S. Hirai (2005). "Behavior of supercritical CO2 injected into porous media containing water." Energy **30**(11–12): 2370-2382.

Sukop, M. C. and J. D.T. Thorne (2006). Lattice Boltzmann Modeling: An introduction for geoscientists and engineers. Heidelberg, Berlin, New York, Springer.

Sukop, M. C. and D. Or (2004). "Lattice Boltzmann method for modeling liquid-vapor interface configurations in porous media." Water Resour. Res. **40**(W01509): 1-11.

Survey, E. R. C. B. A. G. (2006). "Test case for comparative modelling of CO2 injection, migration and possible leakage - Wabamun Lake area, Alberta, Canada, datasets." Retrieved June 6th, 2011, 2011, from http://www.ags.gov.ab.ca/co2_h2s/wabamun/wabamun_download.html.

Taylor, L. H. and R. J. Vinopal (1999). Conventional Core vs. Mini-Permeameter Permeability Measurements: Tensleep Formation. SPE Rocky Mountain Regional Meeting, 15-18 May 1999. Gillette, Wyoming, Society of Petroleum Engineers.

Tecplot (2006). "Interpolate Kriging." Retrieved March 2012, 2012, from http://download.tecplot.com/focus/2006/help/tecplot/index.htm#interpolate_kriging.htm.

Tidwell, V. C. and J. L. Wilson (2002). "Visual attributes of a rock and their relationship to permeability: A comparison of digital image and minipermeameter data." Water Resour. Res. **38**(11): 1261.

Tölke, J. (2002). "Lattice Boltzmann simulations of binary fluid flow through porous media." Philosophical Transactions of the Royal Society of London. Series A: Mathematical, Physical and Engineering Sciences **360**(1792): 535-545.

Unalmiser, S., J. J. Funk and S. Aramco (1998). "Engineering Core Analysis." Journal of Petroleum Technology **50**(4): 106-114.

Venteris, E. R. and K. M. Carter (2009). "Assessing spatial uncertainty in reservoir characterization for carbon sequestration planning using public well-log data: A case study." Environmental Geosciences **16**(4): 211-234.

White, F. M. (2006). Fluid Mechanics, Six Edition. New York, McGraw-Hill.

Xu, W., T. T. Tran, R. M. Srivastava and A. G. Journel (1992). Integrating Seismic Data in Reservoir Modeling: The Collocated Cokriging Alternative. SPE Annual Technical Conference and Exhibition, 4-7 October 1992. Washington, D.C., Society of Petroleum Engineers**:** 833-842.

Yiotis, A. G., J. Psihogios, M. E. Kainourgiakis, A. Papaioannou and A. K. Stubos (2007). "A lattice Boltzmann study of viscous coupling effects in immiscible two-phase flow in porous media." Colloids and Surfaces A: Physicochemical and Engineering Aspects **300**(1–2): 35-49.

Zhang, D. (1998). "Numerical solutions to statistical moment equations of groundwater flow in nonstationary, bounded, heterogeneous media." Water Resour. Res. **34**(3): 529-538.

Zhang, D., R. Zhang, S. Chen and W. E. Soll (2000). "Pore scale study of flow in porous media: Scale dependency, REV, and statistical REV." Geophysical Research Letters **27**(8): 1195-1198.